

2013-01-01

Development Of `Lick And Stick' Passive Wireless Temperature Sensor For Harsh Environment

Hasanul Karim

University of Texas at El Paso, hkarim@miners.utep.edu

Follow this and additional works at: https://digitalcommons.utep.edu/open_etd



Part of the [Mechanical Engineering Commons](#)

Recommended Citation

Karim, Hasanul, "Development Of `Lick And Stick' Passive Wireless Temperature Sensor For Harsh Environment" (2013). *Open Access Theses & Dissertations*. 1653.

https://digitalcommons.utep.edu/open_etd/1653

This is brought to you for free and open access by DigitalCommons@UTEP. It has been accepted for inclusion in Open Access Theses & Dissertations by an authorized administrator of DigitalCommons@UTEP. For more information, please contact lweber@utep.edu.

DEVELOPMENT OF 'LICK AND STICK' PASSIVE WIRELESS
TEMPERATURE SENSOR FOR HARSH ENVIRONMENT

HASANUL KARIM

Department of Mechanical Engineering

APPROVED:

Yirong Lin, Ph.D., Chair

Norman Love Jr., Ph.D.

Tzu-Liang (Bill) Tseng, Ph.D.

Benjamin C. Flores, Ph.D.
Dean of the Graduate School

Copyright ©

by

Hasanul Karim

2013

Dedication

My mother Mosammat Begum Nurjahan, my father Ali Karim, my brother Nazmul Karim, & my wife Naznin Jahan Afrose

DEVELOPMENT OF 'LICK AND STICK' PASSIVE WIRELESS
TEMPERATURE SENSOR FOR HARSH ENVIRONMENT

by

HASANUL KARIM, Bachelor of Science in Mechanical Engineering

THESIS

Presented to the Faculty of the Graduate School of

The University of Texas at El Paso

in Partial Fulfillment

of the Requirements

for the Degree of

MASTER OF SCIENCE

Department of Mechanical Engineering

THE UNIVERSITY OF TEXAS AT EL PASO

December 2013

Acknowledgements

First, I would like to thank the Department of Energy for supporting this project. I want to express my gratitude to my supervisor Dr. Yirong Lin for giving me this research project and for all his support, advice, and encouragement. I would like to thank my committee members, Dr. Normal Love and Dr. Bill Tseng for agreeing to be on the defense committee. I want to especially thank to Mr. Diego Delfin, Dr. Sarah Gaytan and Ms. Monica Cadena for their contributions, help and suggestions in this project. I would like to thank W. M. Keck Center in UTEP for providing the facility to fabricate the samples. I am thankful to Mr. Cesar Garcia and Mr. Jay H Barton and Mr. Jeff Peebles for their kind and sincere help in the testing part of the project. I would like to thank Dr. Evgeny Shafirovich and his students for their help in the fabrication process. I would like to thank all the members of Dr. Lin's research group for their co-operation, help and invaluable suggestions throughout this project. I would like to thank Mr. Mohammad Arif Ishtiaque Shuvo and Mr. Md. Rajib for being such good friends and making things easier for me.

Lastly, but not the least, I am grateful to my dear wife Naznin Jahan Afrose. I could not have completed my thesis without her unlimited support and patience.

Abstract

Wireless passive temperature sensors have been receiving increasing attention due to the ever-growing need of higher energy efficient and precise monitoring of temperatures in high temperature energy conversion systems such as gas turbines and coal-based power plants. Unfortunately, the harsh environment such as high temperature and corrosive atmosphere present in these systems has significantly limited the reliability and increased the cost of current solutions. Therefore, this research project presents the concept and design of a low cost, passive, and wireless temperature sensor that can withstand high temperature and harsh environment. The temperature sensor was designed following the principle of metamaterials by utilizing Closed Ring Resonators (CRR) in a dielectric matrix. The proposed wireless, passive temperature sensor behaves like an LC circuit, which has a temperature dependent resonance frequency. A full wave electromagnetic solver Ansys Ansoft HFSS was used to validate the model and to evaluate the effect of different geometry and combination of SRR structures on the resonance frequency and sensitivity of the proposed sensor. Two different fabrication methods – compression method using a die-punch assembly and 3D printing using binder-jetting techniques were used to fabricate the sensors. To simplify the sensor design, commercially available metal washers were used as CRR structures. Barium Titanate (BTO), and Alumina (Al_2O_3) were used as dielectric materials. Material characterization was done using Scanning Electron Microscopy (SEM) and X-ray Diffraction (XRD), and preliminary free space testing at room temperature using horn antennas and Gaussian beam antennas very promising results for using this novel sensing system for harsh environment application.

Table of Contents

Acknowledgements	v
Abstract	vi
Table of Contents	vii
List of Tables	viii
List of Figures	ix
Chapter 1: Introduction	1
1.1 Introduction to metamaterials	1
1.2 Application of Metamaterials	7
1.3 Metamaterials in sensing technology	9
1.4 Conclusion	11
Chapter 2: Literature Review	12
2.1 Metamaterials	12
2.2 Wireless temperature sensing	17
2.3 Conclusion	19
Chapter 3: Model and Simulation	20
3.1 Concept and model of the sensor	20
3.2 Different SRR structure and their response with varying parameters	21
3.3 Effects of the substrate thickness (d) on Resonance Parameters	24
3.4 Effects of the split gap (g) on Resonance Parameters	27
3.5 Effect of relative permittivity (ϵ_r) on the resonance frequency	29
3.6 Comparison of the Electrical sizes of the sensor model with different SRR structure.....	30
3.7 Conclusion.....	31
Chapter 4: Fabrication	32
4.1 Fabrication using conventional die-punch assembly	32
4.2 Fabrication using 3D printing	40
4.3 Conclusion	53
Chapter 5: Testing and Results.....	55
5.1 Experimental setup using waveguide and network analyzer and corresponding test results	55
5.2 Experimental setup for free space measurement using horn antenna and corresponding test results	57
5.3 Experimental setup for free space measurement using Gaussian Beam antenna and corresponding test results	61
5.4 Conclusion.....	66
Chapter 6: Conclusion	67
References	69
Curriculum Vita.....	76

List of Tables

Table 4.1: Waveguide specifications	34
Table 4.2: Summary of fabricated samples	35

List of Figures

Figure 1.1: Directions of the Electric (E) and Magnetic (H) vector fields, wave vector (k) and the power flow density (S) vector in (a) Right Handed Medium and (b) Left Handed Medium.....	3
Figure 1.2: Light ray passing from medium 1 to medium 2. 1) incident ray, 2) Reflected ray, 3) refracted ray in a right handed medium and 4) refracted ray in a left handed medium	4
Figure 1.3: Different excitation techniques for SRR structure (a) only magnetic excitation (b) electric and magnetic excitation (c) only electric excitation and (d) no excitation. [9]	5
Figure 1.4: A square array of the first SRR structure proposed by Pendry et al. with lattice spacing a [10].	6
Figure 1.5: Some SRR structures studied in literature [12-15]	7
Figure 1.6: (A) 2D and (B) 3D paths that a light will follow theoretically through a cloaking device. [20]	8
Figure 1.7: (a) Schematic of the micrometer-sized metamaterial resonators sprayed on paper substrates with a predefined microstencil (b) Fabricated sample (c) Optical microscopy image of an as fabricated paper metamaterial sample	10
Figure 2.1: Photograph of an as built thermal cloak by Schittny et al. [83]	16
Figure 2.2: Schematic of wireless sensing of integrated resonator/antenna sensor developed by Cheng et al. [99]	18
Figure 3.1: (a) Proposed model of the temperature sensor (b) Equivalent circuit	21
Figure 3.2: Proposed sensor based on CRR structure modeled in Ansys Ansoft HFSS	22
Figure 3.3: Sensor model with different SRR structures: (a) EC-SRR (b) DSRR (c) BC-SRR (d) BC-CSRR (e) MSRR (f) DMSRR	22
Figure 3.4: An DMSRR model showing all the geometry parameters	23
Figure 3.5: Transmission spectrum, (a) CRR, (b) EC-SRR	24
Figure 3.6: Transmission spectrum, (a) DSRR (b) BC-SRR sensor structures.....	25
Figure 3.7: Transmission spectrum, (a) DMSRR (b) BC-CSRR sensor structures.	25
Figure 3.8: (a) Transmission spectra, MSRR structure (b) Effect of substrate thickness on resonance frequency for different SRR structured units.	26
Figure 3.9: Transmission spectra, (a) EC-SRR structure (b) DSRR structure	27
Figure 3.10: Transmission spectra, (a) BC-SRR structure (b) DMSRR structure	28
Figure 3.11: Transmission spectra, (a) BC-CSRR structure (b) MSRR structure	28
Figure 3.12: Effect of split gap on resonance frequency for different SRR structured units.....	29
Figure 3.13: (a) Transmission spectra, CRR structure (b) Effect of dielectric constant on resonance frequency for different SRR structured units.	30
Figure 4.1: Temperature and grain size influence in BaTiO ₃ properties [107]	33
Figure 4.2: (a) Schematic of sensor architecture, (b) die placed inside of the pressing machine, prior to compression.....	35
Figure 4.3: Sample 1, (a) top view, (b) 3D view	36
Figure 4.4: Sample 2, (a) top view, (b) 3D view	37
Figure 4.5: Sample 3, (a) top view, (b) 3D view	37
Figure 4.6: Sample 4, (a) top view, (b) 3D view	37
Figure 4.7: Sample 5, (a) top view, (b) 3D view	38
Figure 4.8: Sample 6, (a) top view, (b) 3D view	38
Figure 4.9: Sample 7, (a) top view, (b) 3D view	38

Figure 4.10: Sample 8, (a) top view, (b) 3D view	39
Figure 4.11: Samples polished for X band testing. Both (a) and (b) were fabricated under the same characteristics	39
Figure 4.12: Schematic of powder bed system [108]	40
Figure 4.13: As received BTO powder [108]	41
Figure 4.14: Different temperature profiles used for sintering fabricated parts [108]	42
Figure 4.15: Density vs sintering temperature for different binder saturations [108]	43
Figure 4.16: Set of magnified images (a) to (c) of sample fabricated with 60% binder saturation, layer thickness of 30 μm and sintered at 1200 $^{\circ}\text{C}$ for 4 hours [108]	44
Figure 4.17: Set of magnified images (a) to (c) of sample fabricated with 60% binder saturation, layer thickness of 30 μm and sintered at 1260 $^{\circ}\text{C}$ for four hours [108]	45
Figure 4.18: Set of magnified images (a) and (b) of sample fabricated with 60% binder saturation, layer thickness of 30 μm and sintered at 1330 $^{\circ}\text{C}$ for four hours [108]	46
Figure 4.19: Set of magnified images a) to c) of sample fabricated with 60% binder saturation, layer thickness of 30 μm and sintered at 1400 $^{\circ}\text{C}$ for four hours [108]	47
Figure 4.20: XRD analysis of as-received powder and sample sintered at 1260 $^{\circ}\text{C}$ for four hours [108]	48
Figure 4.21: Graph depicting shrinkage percentage in each direction vs sintering temperature [108]	49
Figure 4.22: CAD design of (a) Male part with extrusions (b) Female part with holes (c) Section view of the assembly	50
Figure 4.23: Fabricated male and female parts with BTO, sintered at 1260 $^{\circ}\text{C}$ for four hours	50
Figure 4.24: SEM image of raw alumina powder at different magnifications	51
Figure 4.25: Fabricated male and female parts using alumina (a) before sintering and (b) after sintering at 1680 $^{\circ}\text{C}$ for 4 hours	52
Figure 4.26: CAD design of curved sample of (a) 4.38 mm arc length and 4mm thickness (b) 20 mm arc length and 2.5 mm thickness	52
Figure 4.27: Fabricated curved samples (a) as built samples (b) small sample fitted inside the tube (c) large sample inside the tube	53
Figure 5.1: Experimental setup of measuring dielectric constant with a waveguide, a 3D printed BTO sample is placed in front of the setup	55
Figure 5.2: Dielectric constant of BTO samples fabricated by 3D printing and sintered at different temperatures as a function of frequency	56
Figure 5.3: Dielectric constant of an as built sample fabricated by compression method as a function of frequency	57
Figure 5.4: Free space measurement setup using horn antenna connected to a network analyzer	58
Figure 5.5: Transmission response measured from the scattered parameters for sample 3, 4, and 5 placed horizontally	59
Figure 5.6: Transmission response measured from the scattered parameters for sample 3, 4, and 5 placed vertically	60
Figure 5. 7: Free space testing setup with two Gaussian Beam antennas connected with a network analyzer (www.mwilab.com)	61
Figure 5.8: Transmission response from sample 1 (a) from 2-18 GHz (b) from 12-18 GHz	62
Figure 5.9: Transmission response from sample 2	63
Figure 5. 10: Transmission response from sample 3 (a) from 2-18 GHz (b) from 11-18 GHz	63
Figure 5.11: Transmission response from sample 4	64

Figure 5.12: Transmission response from sample 5	64
Figure 5.13: Transmission response from sample 6	65
Figure 5.14: Transmission response from sample 7	65
Figure 5.15: Transmission response from sample 8	66

Chapter 1: Introduction

There is an increasing demand for the further development of sensing technologies in the energy conversion systems such as gas turbines, coal based power plants, and in automotive industries. Precise temperature sensing is one of the most critical parameters to safeguard better combustion, achieve higher efficiency and lower contaminant emissions to the environment. Since these combustion processes create a harsh environment of high temperature and corrosive conditions, it is imperative that the sensors are made to survive this environment and at the same time being reliable. Eventually, necessity of wireless sensors increased as the wired systems are found to be expensive, complicated, and they limit the operating temperatures. Previous efforts on the regime of wireless sensing include thermocouples, thermoelectric materials and fiber optics. However, most of the approach is limited due to either being complicated or expensive. Furthermore, low reliability has been identified as an issue while working on harsh environments due to the use of welded joints, energy storage devices, and semi-conductor materials in their arrangements [1-3]. Therefore, there is an ever-increasing interest in developing passive, wireless, low cost and reliable temperature sensors capable of working in the hostile environments present in energy conversion systems. This thesis is a proposal for a passive wireless temperature sensor for harsh environments inspired from the concept of metamaterials. This first chapter of the dissertation presents the background of the study, describes its significance, and provides an overview of the methodology used.

1.1 Introduction to metamaterials

Meta is a Greek word, which means “beyond”, hence the word “metamaterials” refers to materials that can display properties that are beyond the properties of natural materials. Usually the structure of these materials plays a significant role deciding its properties rather than the material properties of its components. When an electromagnetic wave passes through a material, the otherwise nonhomogeneous medium can be considered as a homogeneous medium if the

atoms of that material are very small compared to the wavelength of the incident electromagnetic wave. So, from the electromagnetic point of view, it is the wavelength λ that determines whether a collection of objects can be considered as a material or not. The block of objects might not be considered as a material by the conventional definition of materials but to the incident electromagnetic wave there is no difference and hence this can be considered as an artificial material or metamaterial [4]. Such homogeneous medium can be characterized by only two parameters: electric permittivity (ϵ) and magnetic permeability (μ). These two parameters are very important and determine the propagation characteristic of an electromagnetic wave through a medium, which can be shown by the dispersion equation. The dispersion relation for an isotropic medium is defined as:

$$k^2 - \frac{\omega^2}{c^2} n^2 = 0 \quad (1.1)$$

Where, k is the wavenumber, ω is the angular frequency, c is the velocity of light in vacuum and n is the refractive index of the substance, which is given by,

$$n = \sqrt{\mu_r \epsilon_r} \quad (1.2)$$

Where, μ_r is the relative permeability and ϵ_r is the relative permittivity of the medium. For most of the natural materials both relative permeability and permittivity are positive and hence n is also a positive number. As long as both μ_r and ϵ_r have the same sign, n is a real number and wave will propagate through the medium but, if one of them is negative then n becomes imaginary and there will be no transmission for a thick substance. Now, the significance of both negative ϵ_r and μ_r can be further investigated by examining Faraday's and Ampere's law. For a monochromatic plane wave that uses $e^{j\omega t}$ convention, Ampere's and Faraday's law are expressed in equation 1.3 and 1.4 respectively:

$$\vec{k} \times \vec{H} = -\omega \epsilon \vec{E} \quad (1.3)$$

$$\vec{k} \times \vec{E} = \omega \mu \vec{H} \quad (1.4)$$

Where, \vec{k} is the wave vector, \vec{H} and \vec{E} are magnetic and electric field intensity vectors respectively. When both ϵ and μ are positive, from equation (1.3) and (1.4) it can be seen that \vec{k} , \vec{H} and \vec{E} form a right-handed co-ordinate system whereas when they are both negative, the

vectors form a left-handed co-ordinate system. A comparison between left-handed and right-handed co-ordinates systems is shown in Figure 1.1. Veselago's proposal of an artificial medium that can have simultaneously negative values of permittivity (ϵ) and permeability (μ) in 1968 was actually the starting point of the research on

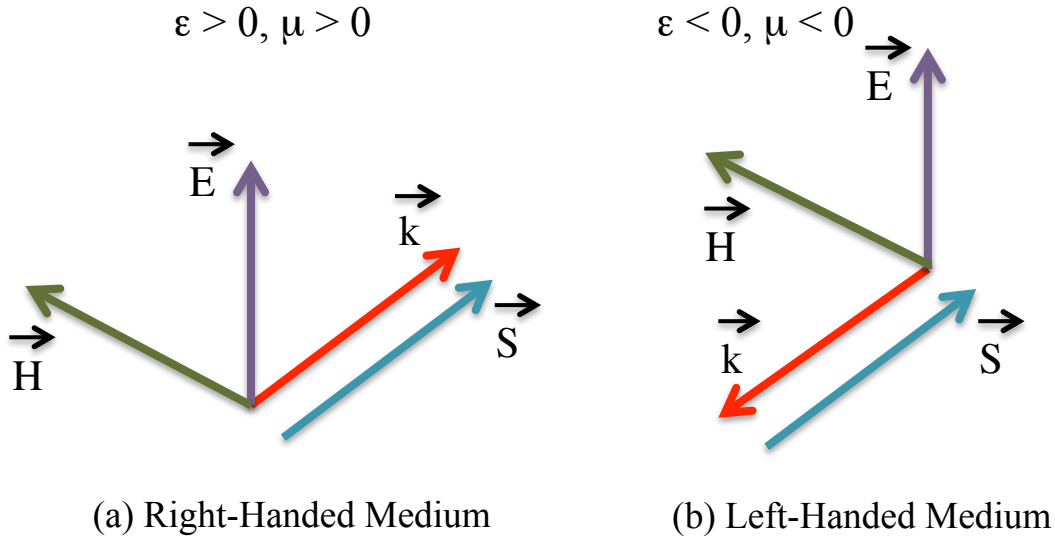


Figure 1.1: Directions of the Electric (E) and Magnetic (H) vector fields, wave vector (k) and the power flow density (S) vector in (a) Right Handed Medium and (b) Left Handed Medium

left-handed metamaterials [5]. It was expected that a left-handed medium would display some nonconventional behaviors such as backward propagation, reverse Doppler effect, reverse Vavilov-Cerenkov effect, and negative index of refraction [6]. The phenomenon of negative index of refraction can be explained with a modified Snell's law. When a ray of light passes from one medium to another medium the refraction of the light follows the general Snell's law (equation 1.5) if both media are right handed. As shown in Figure 1.2, the incident light ray is reflected along path 2 and refracted through path 3. However, if one of the media is left handed then a more accurate form of the Snell's law is used (equation 1.6). In that case, the refracted light goes along path 4.

$$\frac{\sin \theta}{\sin \phi} = \frac{n_2}{n_1} = \sqrt{\frac{\mu_2 \epsilon_2}{\mu_1 \epsilon_1}} \quad (1.5)$$

$$\frac{\sin \theta}{\sin \phi} = \frac{n_2}{n_1} = \frac{p_2}{p_1} \sqrt{\frac{\mu_2 \epsilon_2}{\mu_1 \epsilon_1}} \quad (1.6)$$

Where p_1 and p_2 are the rightness of the first and second medium respectively. p is +1 for a right handed medium and it is -1 for a left handed medium.

Negative values of permeability and permittivity can be obtained by combining special resonator structures with appropriate excitation techniques. There are three types of excitations that can be used for metamaterial resonator structures. They are: magnetic excitation, electric excitation and both magnetic and electrical excitation [6-8]. The choice of the excitation depends on the desired application. If ENG regions are required, the structure has to be excited electrically and it has to be excited

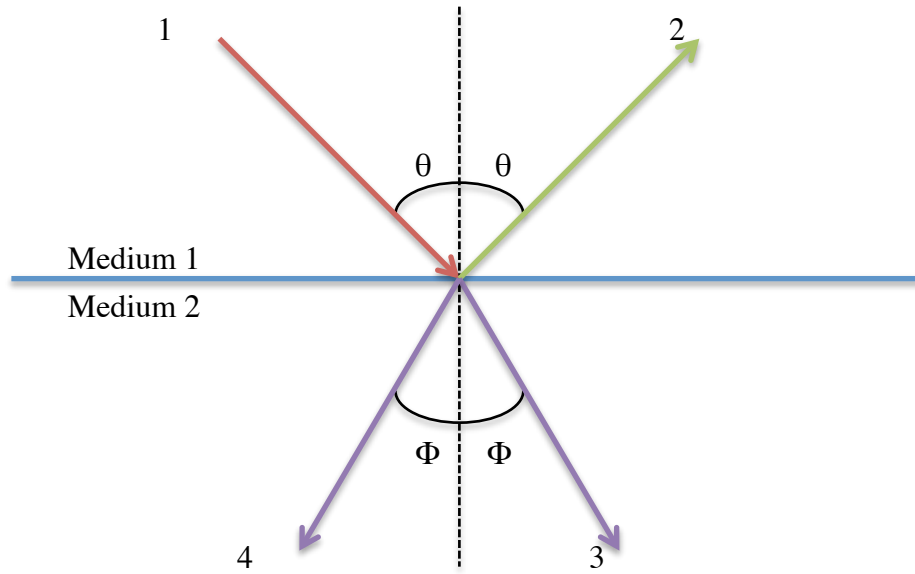


Figure 1.2: Light ray passing from medium 1 to medium 2. 1) incident ray, 2) Reflected ray, 3) refracted ray in a right handed medium and 4) refracted ray in a left handed medium

magnetically in order to obtain MNG regions [8]. Figure 1.3 summarizes the excitation techniques for a SRR structure. In figures 1.3(a) and 1.3(b), the magnetic field is perpendicular to the SRR plane. Hence, according to the Faraday's law of induction it can excite the magnetic resonances of the SRR. On the other hand when the magnetic field is parallel to the SRR plane it cannot excite a magnetic resonance. In figures 1.3(b) and 1.3(c), the electric field is

perpendicular to the gap of the rings. This configuration can excite the electrical resonances of the structure. Hence, the structure in figure 1.3(b) is excited both electrically and magnetically and the structure at 1.3(d) is not excited at all from the sense of an LC circuit.

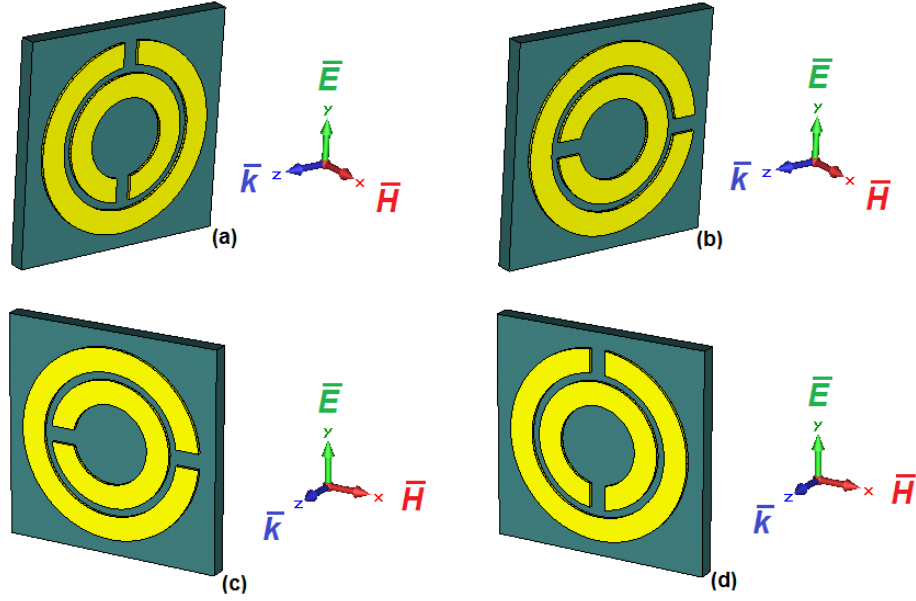


Figure 1.3: Different excitation techniques for SRR structure (a) only magnetic excitation (b) electric and magnetic excitation (c) only electric excitation and (d) no excitation. [9]

Prior to the development of metamaterials, materials with single negative index were found in nature, which were either Epsilon Negative media (ENG) or Mu Negative media (MNG). The concept of a Double Negative media (DNG) or Left Handed Media (LHM) was exciting, but it was not realized in reality until in 1999 when J.B. Pendry et al. [10] proposed the use of periodical arrays of SRRs (Split Ring Resonators) and thin-wires together where the negative values of effective permeability are obtained from the SRR structure and the negative values of permittivity are obtained from the thin wire array. It has been demonstrated that metamaterials need to appear as an effectively homogeneous media, which means that their lattice constants have to be smaller than the wavelength of the incident radiation [11].

Although SRR is not the only structure suggested in literature for obtaining the negative permeability value, it is the most studied structure so far. A single unit of SRR consists of two concentric thin sheets with splits on opposite sides. When excited, most of the electromagnetic energy is stored in the tiny gap between the rings, which results in an immense increase of the energy density. Figure 1.4 shows the SRR structure proposed by Pendry et al. Since then, metamaterials has become a mainstream research area and a numerous amount of publications has been observed over the past decade. Different structures based on the original SRR structure were proposed and evaluated for different applications. Some SRR structures studied in literature are shown in Figure1.5.

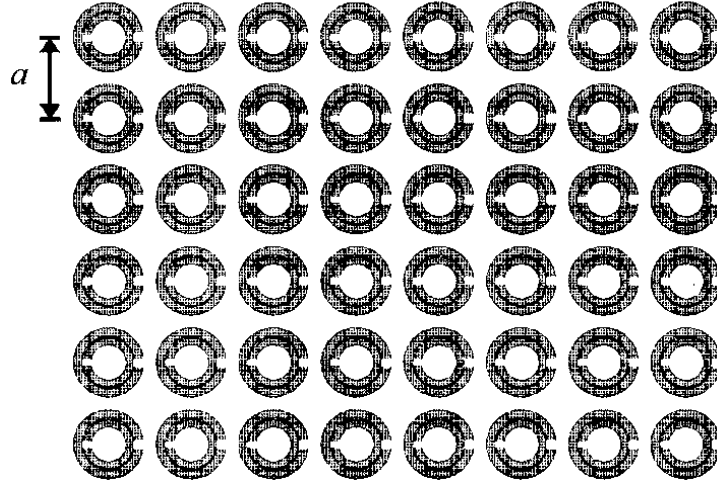


Figure 1.4: A square array of the first SRR structure proposed by Pendry et al. with lattice spacing a [10].

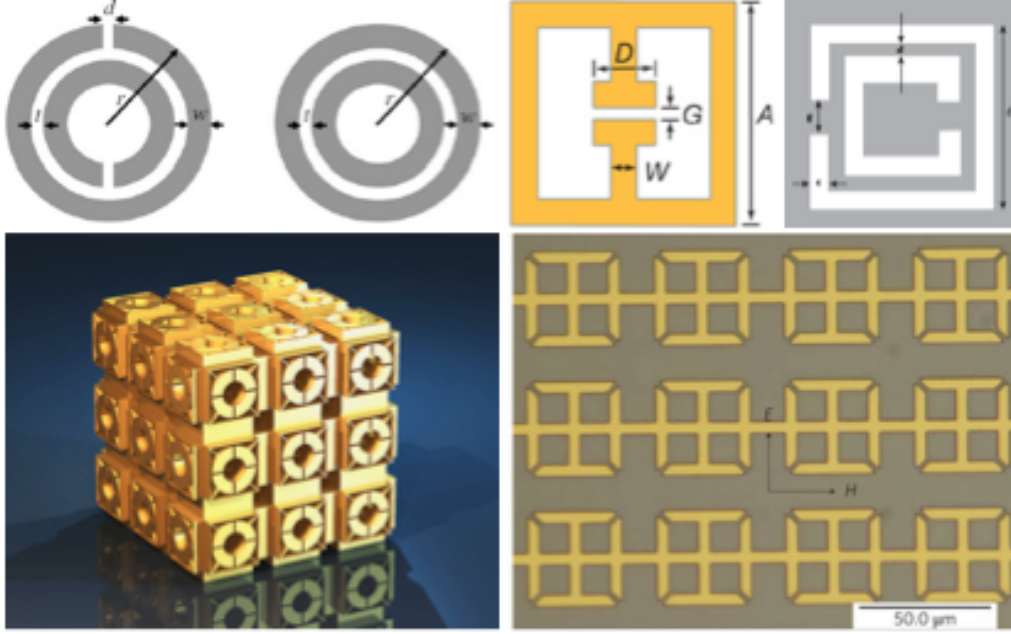


Figure 1.5: Some SRR structures studied in literature [12-15]

Another significant characteristic of the SRR structure is that it shows a resonant behavior. The structure can be represented as an LC circuit and the resonance frequency can be obtained by the following equation:

$$f_0 = 1 / 2\pi\sqrt{LC} \quad (1.7)$$

Where, f_0 is the resonance frequency, L is the inductance and C is the capacitance of the SRR structure. Several approaches were made to analyze different types of SRR structures and to develop mathematical models and equivalent circuits for them, which will be discussed in greater details in the literature review section.

1.2 Application of Metamaterials

Metamaterials have shown a promising future in different fields such as optics and photonics due to their extraordinary properties. Their unique interaction with electromagnetic waves has focused research efforts on developing metamaterial-based applications that couldn't be achieved with regular materials, such as perfect lenses, sensing technologies, cloaking devices and antennas [16]. In order to achieve the aforementioned applications, different types of

metamaterials have been developed including split ring resonators (SRRs), Swiss rolls, conical Swiss rolls and metal plasmons [16].

In Magnetic Resonance Imaging (MRI) obtaining magnetism without using any inherently magnetic materials is of great interest since natural magnetic materials will disturb the quasi-static magnetic field pattern of the system. Magnetic metamaterials that respond only to the time-varying magnetic fields can be used in this type of systems without interfering the field [4]. For example, Freire et al. studied a metamaterial lens for MRI, which improved its coil sensitivity and spatial localization [17].

In the optics area, Pendry proposed a perfect lens based on a negative refractive index material to overcome the limitations of current optical lens solutions [18]. This novel approach was focused on surpassing wavelength limitations imposed by classic alternatives and achieving subwavelength precision. Manipulation of light through metamaterials has also opened the possibility for the development of cloaking devices. Partial cloaking can be achieved by absorbing or scattering incident light away from the detectors [19]. In this field, Shurig et al. studied the possibility of electromagnetic

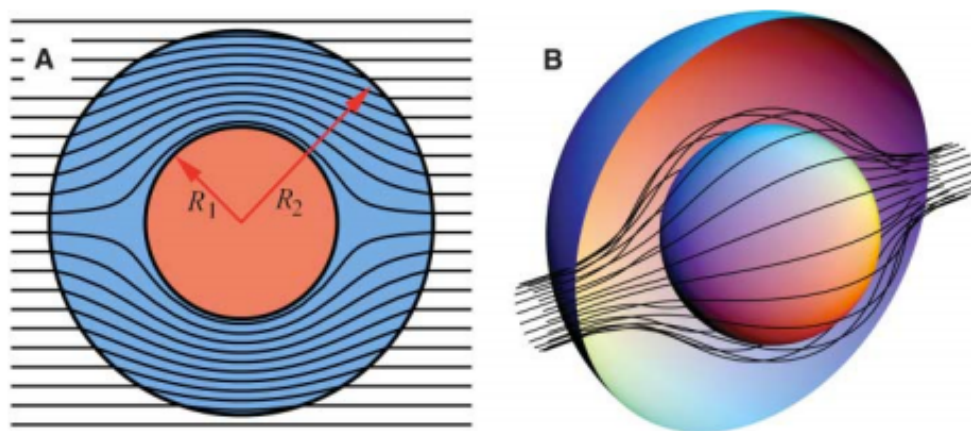


Figure 1.6: (A) 2D and (B) 3D paths that a light will follow theoretically through a cloaking device. [20]

cloaking in the microwave frequency through the fabrication of radial split ring resonators [21]. Their findings support the possibility of achieving cloaking mechanism through the

transformation optics method and metamaterial structures. Moreover, researchers have also studied acoustic cloaking. Chen et al. developed a method for 3D mapping of acoustic cloaking supposing the existence of acoustic metamaterials, which can be achieved through local resonances [22].

Aside of these metamaterial applications, there exist others that could make materials behave like liquids under certain frequency ranges or hide entire buildings from earthquakes. Such metamaterials are called elastic (or mechanical) and seismic metamaterials, respectively. Elastic metamaterials have the ability of transfer only pressure waves at high frequencies; while at low frequencies they transmit pressure waves and shear waves (incompressible solid behavior) in specific directions [23]. Lai et al. studied the use of silicon rubber and steel rods to build a two-dimensional elastic metamaterial to achieve better control of the elastic waves in solid materials [23]. On the seismic front, Torres-Silva et al. analyzed the use of acoustic metamaterials in the form of Swiss rolls to reduce the amplitude of seismic waves [24]. This structure can be placed around the building to act as an earthquake barrier, cloaking the building from the most destructive earthquake waves.

1.3 Metamaterials in sensing technology

Sensor development has also been benefited from the continuous advancement in metamaterials. Different designs have been proposed under the working mechanism of metamaterials for temperature, pressure, humidity and bio sensing. Biosensors are of extreme importance in disease diagnostics, food safety, environmental monitoring and in investigating other biological phenomena. Biosensors based on metamaterials have gained substantial attention because of their cost-effectiveness and label-free biomolecule detection from microwave to optical frequency [25]. Lee et al. [26] studied the use of split ring resonators to detect the binding of biotin and streptavidin, which is one of the most common non-covalent interactions found in nature, at microwave frequencies. A terahertz paper based biochemical sensor was proposed by Tao et al. [27] where the paper acts as a dielectric and a support while

the SRR patterns defines the shift of the resonance as a result of the shift in the capacitance induced by the added material. A schematic and a fabricated sensor are displayed in figure 1.7. A metamaterial-based plasmonic biosensor was developed by Kabashin et al. utilizing an array of vertically aligned gold nanorods on a glass substrate, which improved the sensitivity by more than two orders of magnitude compared to the previously developed plasmonic biosensors [28]. The terahertz region has also been

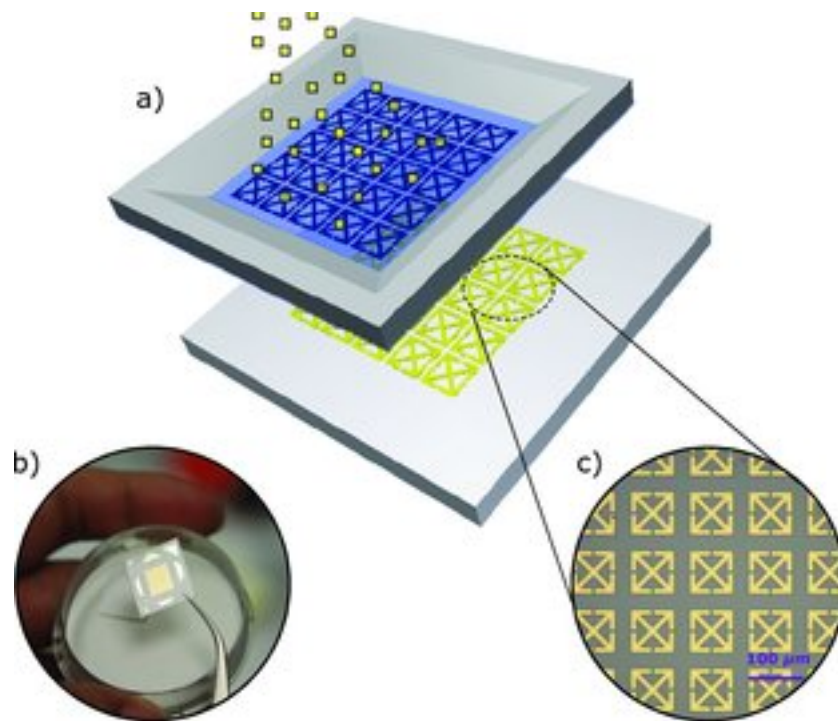


Figure 1.7: (a) Schematic of the micrometer-sized metamaterial resonators sprayed on paper substrates with a predefined microstencil (b) Fabricated sample (c) Optical microscopy image of an as fabricated paper metamaterial sample

explored to identify chemical and biochemical compound composition [25]. This can be achieved by sensing the resonant absorption of molecular or phonon resonances for small compounds. Yoshida et al. [29] proposed a novel, label-free sensing method in the terahertz frequency region by using a metallic mesh with thin profile to detect proteins.

Compared to Biosensors, not many studies have been reported on other types of sensors. Melik et al. [30] demonstrated a wireless strain sensor based on flexible metamaterial structure

combining SRR structure and kapton tape. Ekmekci et al. proposed a metamaterial-based sensor for pressure, concentration, temperature and humidity sensor based on broadside-coupled split ring resonator (BC-SRR) [31]. Additionally, this research group also studied the feasibility of a V-shaped split ring resonator for pressure sensing applications.

1.4 Conclusion

In this study, a metamaterial inspired cheap, passive wireless temperature sensor is proposed that can work in high temperature and harsh environments. This is achieved by using a dielectric matrix that embeds two CRR (Closed Ring Resonator) structures. The sensor unit can be represented as an LC circuit and the resonance frequency of this circuit/structure will change with the change of temperature enabling the measurement of temperature. The model is validated through finite element method and the effect of different geometry and combination of SRR structures on the sensitivity and electrical sizes of the proposed sensor are evaluated.

Chapter 2: Literature Review

The following section will discuss the significant literatures that have pioneered the research in metamaterials and in wireless temperature sensing. The first half of the literature review will cover the development of metamaterials. An effort will be made to provide a brief history of the birth and growth of this extraordinary research area, which has made things possible that once were considered as impossible. Over a really short span of time this field has seen many revolutionary findings and has spread in a lot of areas. While every effort was made to cover all the significant pioneering literatures and important current findings, the overwhelming amount of research that is being done on this field has made it beyond the scope of this thesis to produce a complete report. The second half focuses on the recent development of the wireless temperature sensing system, which include both conventional approach and metamaterial-based approach.

2.1 Metamaterials

Although the surge of research in the area of metamaterials has started in the last decade, the idea of having artificial materials comprised of customized functional building blocks packed into an effective medium can be traced back to 1898 [32, 33], when Jagadish Chunder Bose conducted the first microwave experiment on twisted dielectric composites [34] which by today's definition was an artificial chiral medium [33] and it lead to artificial linear and circular birefringence. In 1920, Karl Lindman [32, 35] experimented with hand made copper helices individually wrapped into cotton balls and densely packed into an isotropic three dimensional chiral metamaterial which displayed enormous resonant optical activity at microwave frequency. W. E. Kock [33, 36] arranged conducting spheres, disks, and strips periodically to make microwave lenses and demonstrated that it is possible to tailor the effective refractive index of an artificial media.

The starting point of the research in metamaterials however, is considered to be the work of Viktor Veselago who first postulated that a material that has both the electric permittivity and

magnetic permeability, it will have a negative refractive index. This paper was published in 1967 [37] first in Russian and one year later in English. In addition to the negative refractive index or backward wave propagation he also hypothesized a flat lens, which was a possibility that was not considered ever before. But, despite these outstanding hypotheses the paper did not accelerate the research work in this area. After a long time in 1996, J.B. Pendry [38] proposed a grid of conducting wires that generates an effective frequency dispersive permittivity, obeys a Drude model and achieves negative values in the GHz frequency range. A few years later in 1999, he suggested another periodic structure in a form of SRR to achieve a frequency dispersive permeability obeying Lorentz dispersion [10]. It was also shown that by adjusting the parameters properly, the resonant frequency of the SRR could be brought down in the GHz range, resulting a negative value of permittivity in a frequency region that overlaps with the frequency region of negative permittivity. The following year, Smith et al. [39] made a composite medium combining an array of thin wires and SRR structures and demonstrated that indeed in the GHz range, it was possible to achieve simultaneous negative values of permittivity and permeability. So, it was proven that it was possible to make a composite medium to realize negative refraction, and shortly after, Shelby et al. [40] presented the first experimental realization of an LHM and confirmed the negative refractive index of the medium. Although this design undoubtedly produced negative refractive index, there were some drawbacks as well; the most important ones were low transmission level and a narrow band of left-handed properties [41]. Soon structures of novel geometries of SRR were proposed, including the axially symmetric SRR [42, 43], the broadside coupled SRR [44], the omega SRR [45, 46], the brickwall [47], the S-ring SRR [48] and some three dimensional designs [49-51] to rectify these two problems. The anisotropic nature of the SRR structures was another problem because it limits the excitation criteria of the structure [52]. Consequently, many researchers focused on preparing an isotropic structure that will display a negative refractive index irrespective of the propagation vector and orientation of the symmetry axes of the structure. For example, Vendik et al. [53] suggested an artificial structure, which had the arrangement of particles similar to the NaCl structure with cubic

symmetry. They proposed the use of two high permittivity sub-lattices embedded in a low permittivity matrix and the permittivity and permeability tensors of the structure were isotropic.

2.1.1 Numerical simulations in designing and optimizing metamaterials

The design and optimization of different geometries of SRRs depended on largely two approaches [41]: either an equivalent circuit approach [48] or full-wave numerical simulations [54]. The numerical simulation of SRRs verified the experimental results and offered the possibility of analyzing an effective media consisting of discrete elements to validate different properties. Right after the first experimental verification of negative refraction, an Finite Difference Time-Domain (FDTD) method based simulations of similar rings and rod structure provided the first verification of negative refraction by numerical simulations and it also clearly demonstrated the phenomenon of backward phase inside the structure [55]. Later, simulation works focused on analyzing the key properties of LHM [43] and afterwards, the emphasis was on developing efficient numerical algorithms for simulating large or three-dimensional geometries [50]. The use of full wave electromagnetic solver like Ansys Ansoft HFSS (High Frequency Structural Solver) has become more common where reflection and transmission characteristics could be simulated as a function of frequency [8] and the effective parameters could be calculated from the frequency responses of the S-parameters.

2.1.2 Chiral Metamaterials

If the particles of a medium cannot be superimposed on their mirror images then it's called a chiral medium [56]. Due to the intrinsic chiral asymmetry, the medium responds to the left circularly polarized (LCP) wave and right circularly polarized (RCP) wave differently [57]. There is also a cross coupling between the electric field and magnetic field going through a chiral medium which is described by a dimensionless chirality parameter k . Although researches on chiral materials have started long before [58], Tretyakov et al. [59] were first to discuss the possibility of realizing negative refraction in chiral nihility in 2003. The authors proposed the idea of fabricating a metamaterial composed of helical wires as a chiral media. One year later,

Pendry [60] analyzed the conditions to make negative refraction in chiral metamaterials possible and showed that it is in fact simpler than for regular metamaterials, since, a chiral medium does not need either ϵ or μ to be negative to achieve a negative refractive index as long as the chiral parameter k is large enough. Pendry then proposed a practical model with twisted Swiss rolls as elemental structures to obtain a chiral metamaterial working in the microwave regime. After that, the research on chiral metamaterials mainly branched into two directions: bulk chiral metamaterials and planar chiral thin films [57]. So far, most of the researches on bulk chiral metamaterials are theoretical due to the complexity in fabricating homogeneous 3D chiral structures. Significant studies on this topic include a quasi-planar chiral structure based on SRR [61], bulk isotropic magnetic metamaterials [62], and development of 3D isotropic chiral metamaterials [63]. Fabrication of complicated 3D chiral metamaterials using advanced manufacturing such as colloidal nanohole lithography has been reported recently [64-66]. Since planar structures are easier to fabricate than the bulk media, research by many groups has been reported on this topic and many interesting properties and potential applications has been addressed. Zheludev et al. were the first to report the optical activity of a planar chiral structure in the optical regime [67]. Later, a bi-layer rosette-shaped structure in the microwave regime was also reported by the same group, which displayed a very strong rotation in terms of rotary power per wavelength [68]. A planar chiral metamaterial made of dual strips connected by a tilted bridge was reported to have a negative refractive index in the terahertz frequencies [69]. Recently, planar chiral metamaterials has been developed for biosensing applications [70] and asymmetric transmission has been explored [71].

2.1.3 Applications and prospects

The first application for a metamaterial with a negative refractive index was proposed by Pendry [18], which was the exciting declaration of a possible perfect lens or ‘superlens’. Another sensational application proposed by Pendry et al. [20] and later experimentally demonstrated by Schurig et al. [21] was cloaking of objects at microwave frequencies where the authors hid a

copper cylinder inside artificially structured metamaterial cloak. Other applications of LHM were in communication and miniaturization, which include obtaining new radiation patterns [72-74] and cavity resonant modes [41, 75]. Notable studies have been done in obtaining a reduced radar cross-section by analyzing the scattering of mainly canonical objects such as spheres or cylinders [76, 77], which was also extended to other random geometries [20]. The concept of cloaking soon crossed the boundary of only electromagnetic waves and was also applied in other applications. Yang et al. [78] demonstrated a dc electric cloak, which can make objects invisible to the applied static current fields. Theoretical discussion for both static [79, 80] and dynamic cloaking was found in literature. While the idea of static thermal coating was strictly equivalent to the static electric cloaking mentioned above [32, 81], dynamic thermal cloaking was more complicated [82]. Recently, Schittny et al. [83] designed, fabricated and characterized a micro structured transient thermal cloak that molds the flow of heat around an object in a metal plate, the fabricated cloak is shown in Figure 2.1. Other works of metamaterials beyond electromagnetism include acoustic

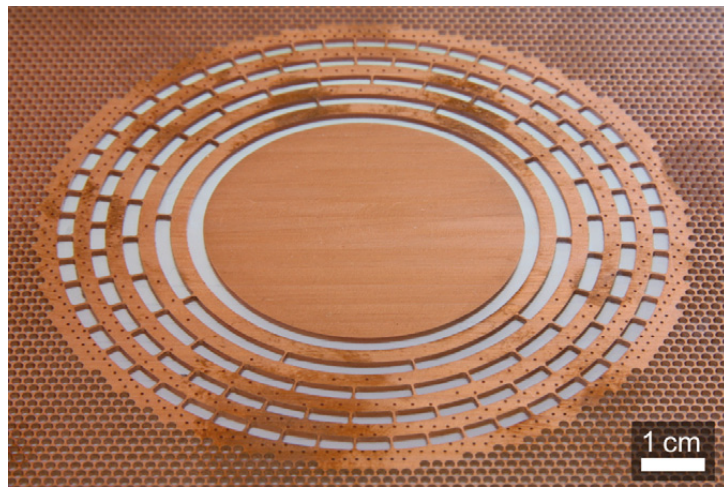


Figure 2.1: Photograph of an as built thermal cloak by Schittny et al. [83]

metamaterials [84, 85], elastodynamic metamaterials [86], ultra-light metamaterials [87], 3D auxetic metamaterials [88] etc.

2.2 Wireless temperature sensing

Temperatures sensing has always been a very important aspect of any energy conversion system since it can reduce heat loss in a system, predict failure and enhance system efficiency. Numerous researches have been done to develop better temperature sensors. The necessity of wireless temperature sensors grew, as conventional wired sensing systems tend to be costly and hard to install and maintain. Many studies have been reported on developing wireless sensing technologies to develop cheap and accurate temperature sensors. Schimetta et al. [89] proposed a hybrid sensor for measuring pressure and temperature using Surface Acoustic Wave (SAW) reflective delay line but the proposed system lacked in accuracy and also had a low temperature limitation (up to 130 °C). Afterwards, advanced SAW based temperature sensors were realized for even moderately conductive media such as ionic water ink [90] or for high temperatures up to 1000 °C [91-93] and for better temperature resolution [94]. Although temperature sensors based on SAW propagation were useful for high temperature and harsh environments as they have the advantage of not having low thermal mass, low conductivity or the strong radiation coupling of the components at high temperature like most of the conventional approach, the acoustic wave propagation through the surface of the material does not depend only on the temperature but also on the geometric, environmental and material properties along the path, which makes it difficult to obtain reliable data [95]. Wireless temperature sensors utilizing a resonating inductor-capacitor (LC) circuit were another approach to overcome these limitations of SAW sensors. A wireless, passive, remote sensor based on a resonating LC circuit was proposed by Ong et al. [96]. The characteristic resonance frequency of this circuit was dependent on the temperature and was the basis of measuring temperature. Later, this concept was applied to measure temperature of a rotating component with a sensitivity of 30kHz/°C. The authors used a capacitive sensing element made of Lead-Lanthanum-Zirconate-Titanate (PLZT) ceramic layer coated with NiCr, which can act as a parallel plate capacitor that is connected to an inductive antenna. The dielectric constant of the ceramic layer is temperature dependent and it can withstand up to 200 °C. Complementary Metal Oxide Semiconductors (CMOS) are another approach to the

temperature sensing which has gained attention over the years. Unfortunately, multiple components of this system make the fabrication complicated [97] and limit the operating temperature range [98]. Most of the developed sensing techniques required some power source, which makes it difficult to implement them at high temperatures. Therefore, an increasing demand of passive sensors is still present especially for harsh environment applications. Wang et al. [95] suggested a passive wireless temperature sensor for harsh environment in 2008 based on a completely passive LC resonant telemetry scheme but the sensor was calibrated and tested for only up to 235 °C. Recently, Cheng et al. demonstrated a resonator/antenna integrated passive wireless sensor using alumina as a dielectric substrate. The sensor was tested in the temperature range from 50 °C – 1000 °C while the resonance frequency of the structure decreased from 5.12 to 4.74 GHz with a sensitivity of 0.4 MHz/°C [99]. A schematic of the sensor is presented in Figure 2.2. The use of LC resonance circuits as a temperature sensing unit and the concept of representing a SRR structured metamaterials as a LC equivalent circuit inspired researchers to develop metamaterial based passive wireless temperature sensors since it offers more versatility, and scalability in design and also needs fewer components compared to the conventional LC circuit or CMOS circuits. So far, only a few studies suggesting

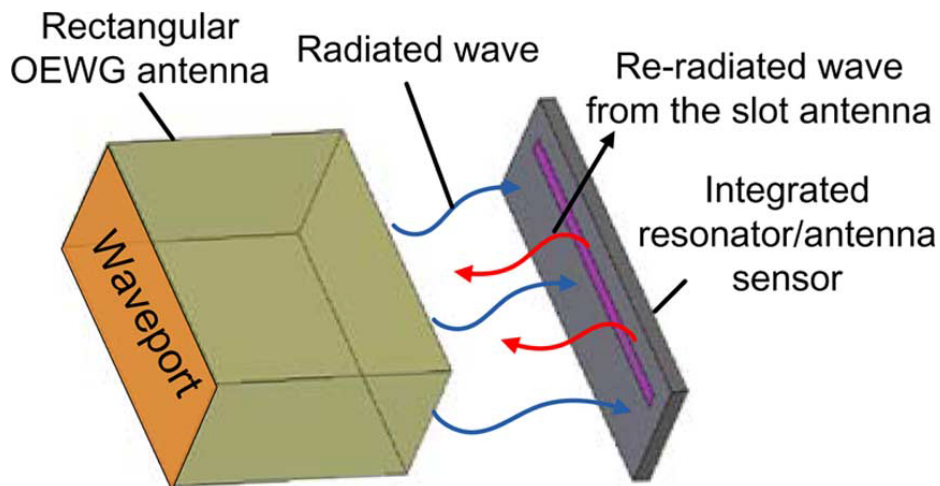


Figure 2.2: Schematic of wireless sensing of integrated resonator/antenna sensor developed by Cheng et al. [99]

metamaterials based wireless temperature sensors have been reported in literature. Thai et al. proposed an ultrasensitive wireless passive temperature transducer combining SRR structures with micro bimorph cantilevers [3]. The bilayer cantilevers deflect with the change of temperatures and thus shift the resonance frequency of the SRR structured resonators. The authors demonstrated a proof of concept utilizing Aluminum-PET (Polyethylene terephthalate) bilayer cantilevers that achieved a sensitivity of 2.14 MHz/°C. Ekmekci et al. [100] also demonstrated the feasibility of a metamaterial-based multi-functional sensor for temperature, humidity, density and pressure sensing. The authors proposed a double-sided split ring resonator (DSRR) topology with an additional sensing medium sandwiched between two identical broadside couple SRR unit cells. The resonance frequency of the DSRR unit changes when the thickness or the dielectric permittivity of this interlayer medium changes with the change of temperature, density, humidity or pressure of the environment surrounding the sensor. The authors used seawater as the interlayer medium for the demonstration of temperature sensing and achieved a sensitivity of 7.5 MHz/°C with the change of temperature from 10 °C to 30 °C.

2.3 Conclusion

Although many studies have been conducted over the years to develop a passive wireless temperature sensor sustainable in harsh environments, there are still several drawbacks of the current solutions, mostly due to the need of a power supply, complicated fabrication processes or temperature limitations. Metamaterials based temperature sensors have been proposed lately but have not been demonstrated for high temperature applications and hence further studies are needed to establish this as a suitable alternative of the current solutions.

Chapter 3: Modeling and Simulation

The first step for the development of the passive wireless temperature sensor shown in Figure 3.1 is to understand how design parameters such as choice of materials, substrate thickness, split gap, different SRR structure and dielectric constant can influence the resonance frequency of the sensor. Understanding these parameters will help to tune the sensor in the optimum resonance frequency and determine the working range of the sensor. To accomplish this, a 3D model of the sensor unit comprising of two CRR (Closed Ring Resonator) structure embedded in a dielectric matrix was developed and analyzed in a full wave electromagnetic solver, Ansys Ansoft HFSS 15.0 and the effect of substrate thickness, split gap and dielectric constant was evaluated. The same parameters were used to evaluate different SRR structures and were compared with the proposed CRR structure. In this chapter, the transmission spectra $S_{2,1}$ with respect to a sweep frequency will be analyzed for sensor unit with different SRR structures and change of resonance frequency with the change of the parameters mentioned will be identified and discussed.

3.1 Concept and model of the sensor

The proposed sensor has two metal CRR embedded in a dielectric material matrix, which separates them as depicted in Figure 3.1(a). The dielectric matrix surrounding the metal CRRs helps protecting the metals from harsh and corrosive environments. An equivalent circuit is also suggested in Figure 3.1(b). Calculations for the capacitance and inductance terms can be found elsewhere [101-103]. CRR structure was chosen to make the fabrication of the sensor easy and cheap as commercially available washers can be used as a CRR structure and complicated fabrication process like photolithography can be avoided.

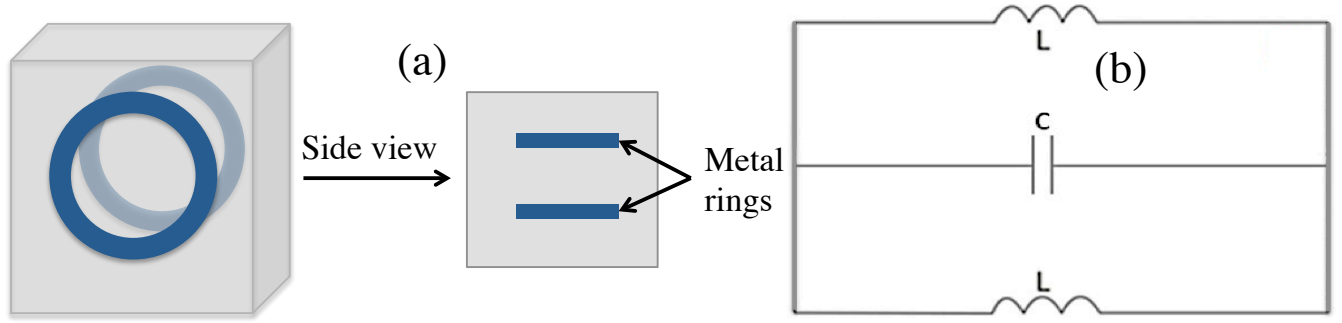


Figure 3.1: (a) Proposed model of the temperature sensor (b) Equivalent circuit

3.2 Different SRR structure and their response with varying parameters

To determine the geometry and configuration of proposed wireless temperature sensor, finite element based modeling was performed using Ansys Ansoft HFSS (High Frequency Structural Solver) 15.0, which is a full wave electromagnetic solver. Parameters for the sensor modeling process consisting of two CRR (Closed Ring Resonators, as shown in Figure 3.2) were evaluated to validate the feasibility of this structure for the sensing application. The most common SRR structures, i.e. EC-SRR (Edge Coupled-SRR) and BC-SRR (Broadside Coupled-SRR) reported to the date and other variations developed from these common structures were also assessed for the effect of substrate thickness, dielectric constant and split gap of the SRRs on the resonance frequency of the sensor unit.

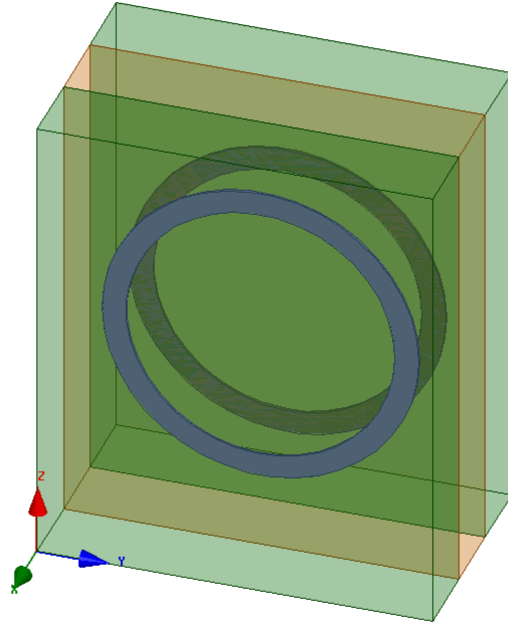


Figure 3.2: Proposed sensor based on CRR structure modeled in Ansys Ansoft HFSS

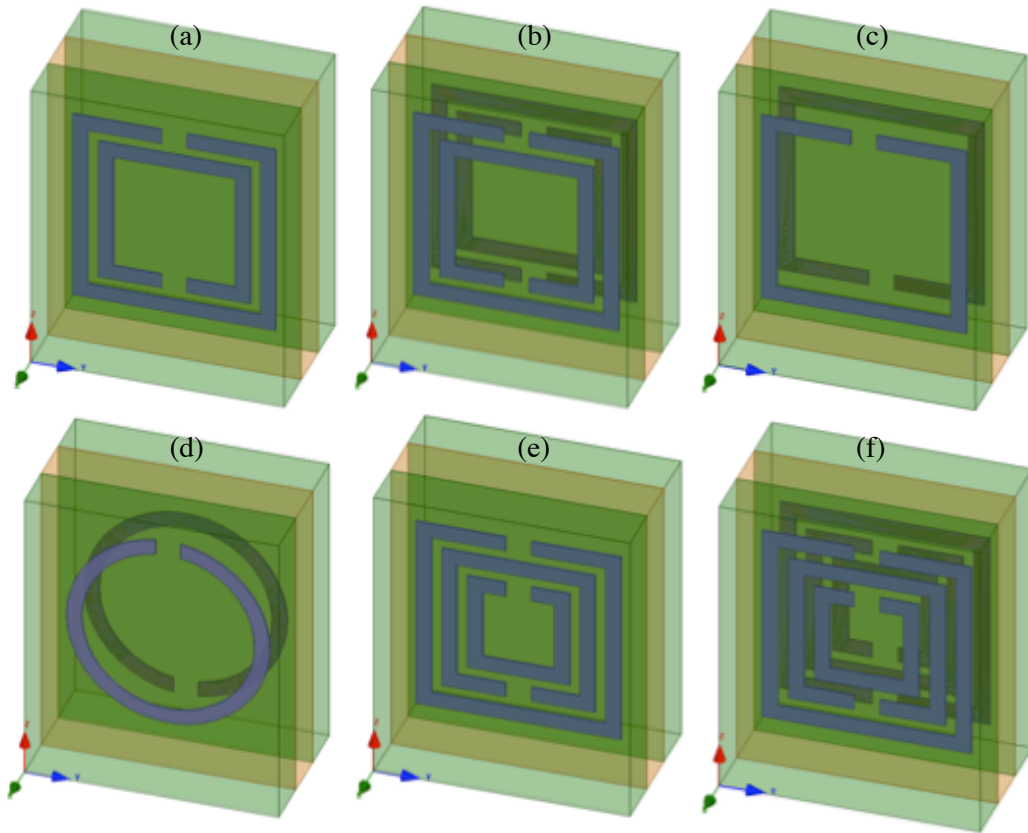


Figure 3.3: Sensor model with different SRR structures: (a) EC-SRR (b) DSRR (c) BC-SRR (d) BC-CSRR (e) MSRR (f) DMSRR

In all the models, a dielectric material separates two ring resonator structures. The distance between these two rings are d as identified in figure 3.4. The length = width = $L = 6\text{mm}$, and thickness = $D = 3\text{mm}$. The sides of each ring is $l_1 = 4\text{mm}$ (all structures except CRR), $l_2 = 3\text{mm}$ (not present in BC-SRR, BC-CSRR, CRR structure), $l_3 = 2\text{mm}$ (only in MSRR and DMSRR). The width of the metal rings $w = 0.3\text{mm}$ and thickness $t = 0.03\text{mm}$ are same for all the SRR structures in every model. Except for CRR, all other ring resonator structures have a split of s mm. The outer diameter for CRR and CSRR structure is 4 mm . In case of EC-SRR, DSRR, DMSRR, and MSRR, separation between the two rings are $g = 0.1\text{ mm}$.

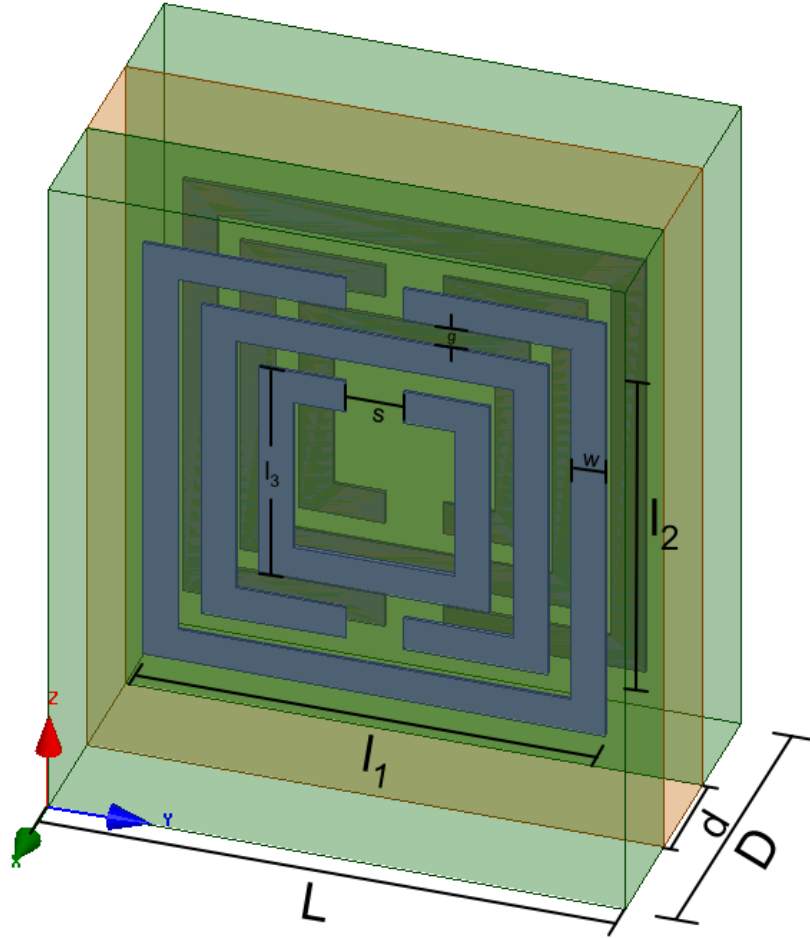


Figure 3.4: An DMSRR model showing all the geometry parameters

3.3 Effects of the substrate thickness (d) on Resonance Parameters

To determine the effect of substrate thickness on sensor characteristic, transmission spectra of different SRR structured sensor model are simulated by the HFSS software using the geometry parameters constant as mentioned above but varying for different substrate thickness, $d = 0.5 \text{ mm}$, 1 mm , 1.5 mm , 2 mm , 2.5 mm and 3 mm .

As the substrate thickness d of the CRR structure increases from 0.5 mm to 3 mm , the resonance frequency of this sensor structure decreases from 14.44 GHz to 12 GHz with a sensitivity of 976 MHz/mm over the range as shown in Figure 3.5 (a). While for EC-SRR structure, the variation is small with all the resonance frequencies within $2.5\text{-}2.6 \text{ GHz}$. The sensitivity for 1 mm substrate thickness increase for this structure is 28 MHz/mm .

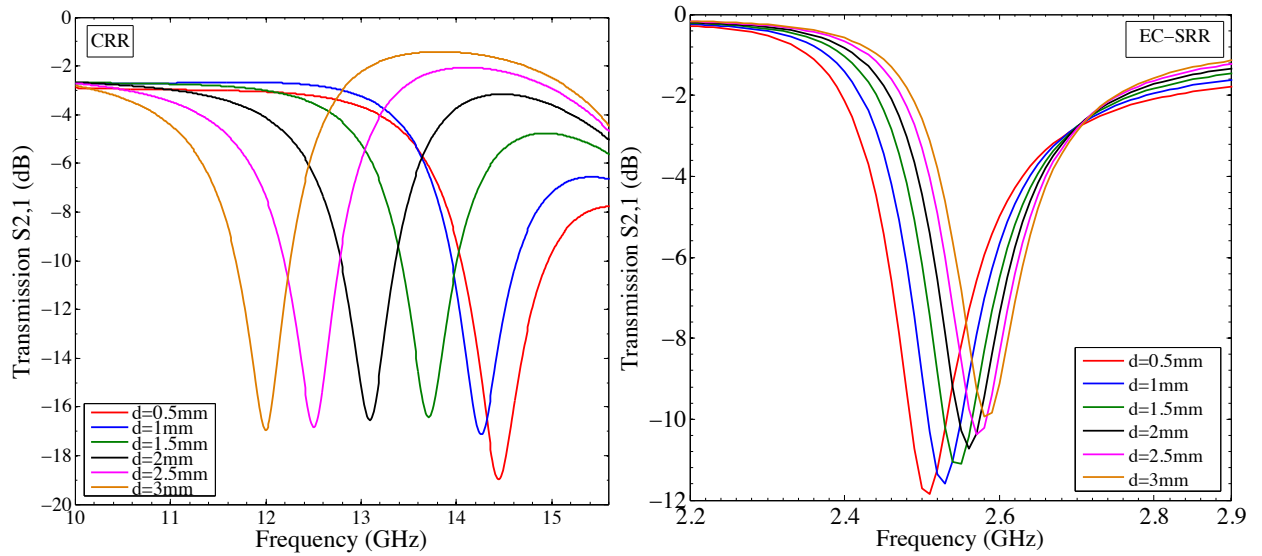


Figure 3.5: Transmission spectrum, (a) CRR, (b) EC-SRR

For DSRR, as this structure has SRR structures on both sides, changing the substrate thickness has greater influence on the resonance frequency than the EC-SRR structure. A drop in the resonance frequency value is also expected because of the higher capacitance between the SRRs on opposite sides. As shown in Figure 3.6 (a), for DSRR structures, the resonance frequency increases from 2.00 GHz to 2.44 GHz and the sensitivity of thickness change is 176 MHz/mm . For BC-SRR structure, the resonance frequency increases from 2.3 GHz to 2.98 GHz

with a sensitivity of 272 MHz per mm, as shown in Figure 3.6(b). It should be noted that the resonance frequency values for this structure is in between EC-SRR and DSRR since there is only one SRR structure on each side; there is no capacitance effect between neighboring SRRs as in case of DSRR structure. But, because of the higher capacitance between the SRRs on opposite sides, the resonance frequencies are lower than EC-SRR structure. As expected, DMSRR structure has a little lower resonance frequency then DSRR structure. The frequency range for this structure is from 2 GHz to 2.43 GHz with a sensitivity of 172 MHz / mm.

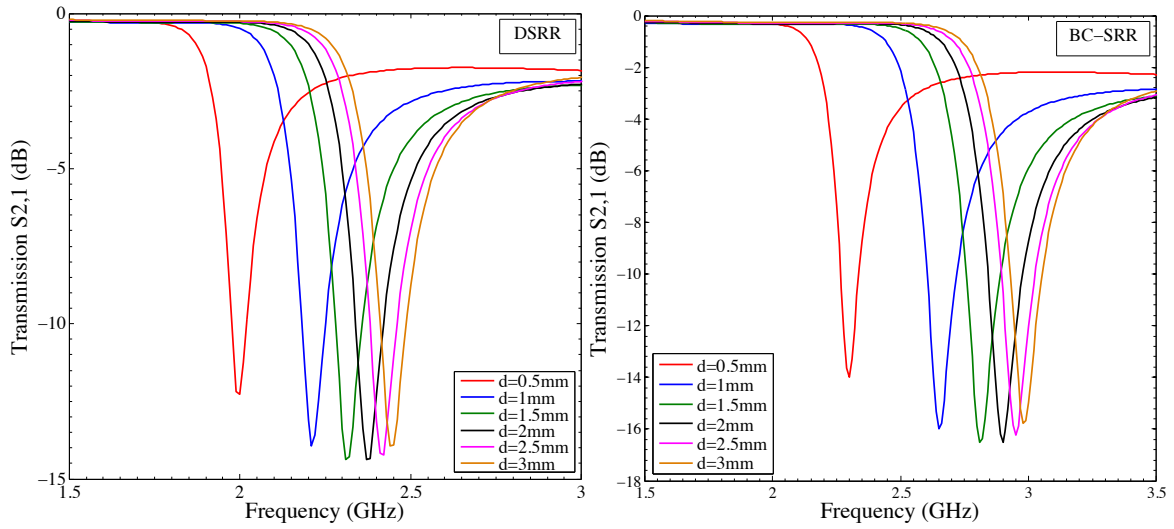


Figure 3.6: Transmission spectrum, (a) DSRR (b) BC-SRR sensor structures

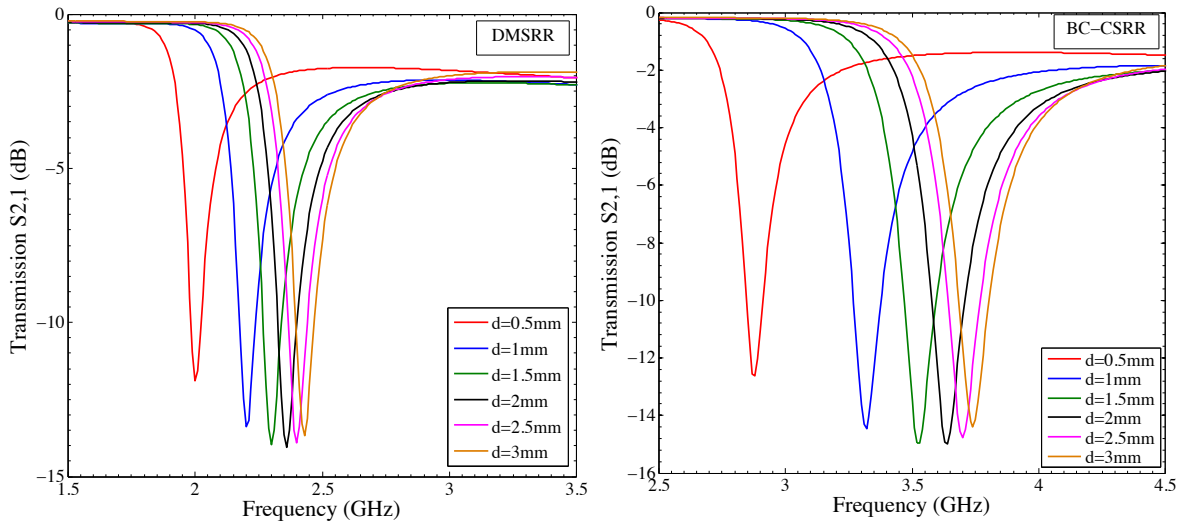


Figure 3.7: Transmission spectrum, (a) DMSRR (b) BC-CSRR sensor structures.

BC-CSRR structure, which basically consists of circular split rings instead of square rings and has the diameter equal to one side of the square SRR in BC-SRR structure displays a higher resonance frequency at any substrate thickness than the BC-SRR structure and the range of resonance frequency for BC- CSRR structure is from 2.88 GHz to 3.74 GHz with sensitivity of 344 MHz/mm. MSRR structure displays resonance frequency close to the EC-SRR structure since there is only one additional

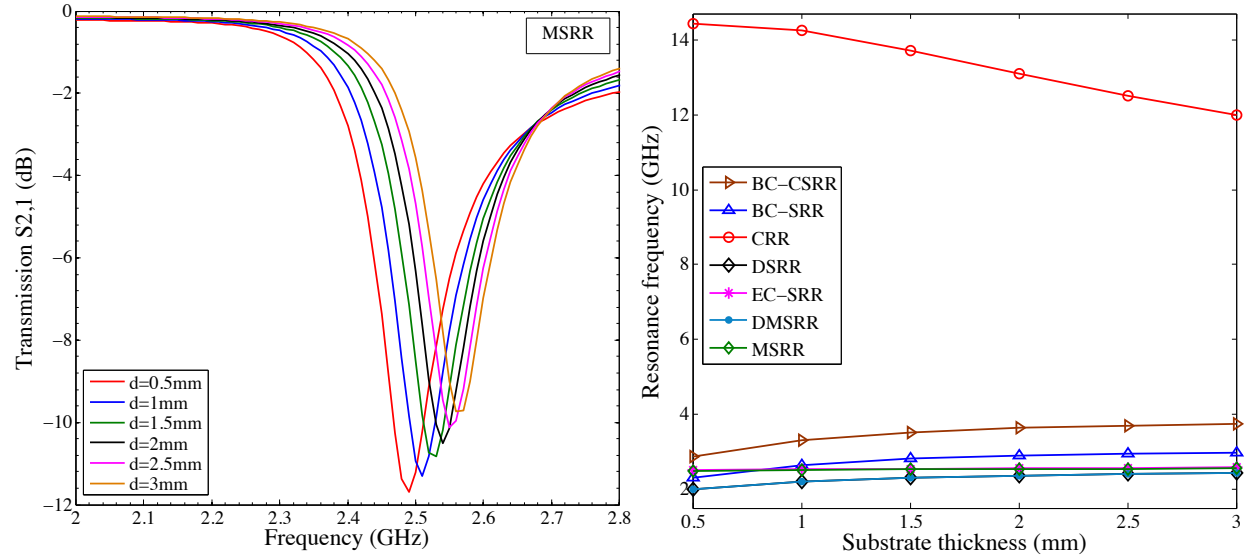


Figure 3.8: (a) Transmission spectra, MSRR structure (b) Effect of substrate thickness on resonance frequency for different SRR structured units.

ring added to the EC-SRR structure. It demonstrates that adding more SRR structure on one side will decrease the resonance frequency. The sensitivity of this structure in terms of substrate thickness is also 28 MHz/mm.

Figure 3.8 (b) depicts a comparison among all the different structures in terms of their change in resonance frequency with the change of substrate thickness. Only CRR structure shows a decrease in resonance frequency with the increase of the substrate thickness and all the other structures display increase but with different sensitivity. Also, it has the highest sensitivity to the change of substrate thickness than the other structures.

3.4 Effects of the split gap (g) on Resonance Parameters

Effect of split gap on the resonance frequency of the structure was evaluated from a gap of 0.2 mm to 3.4 mm. All the other parameters were kept constant. Thickness of each dielectric material layers were 1 mm, ring thickness = 0.03 mm, length of the sides of the SRR was 4mm by 4mm and same materials were used. Since the CRR structure has no split, this parameter is not applicable to this structure. All the other structures show an increase of resonance frequency with the increase of split gap as shown in Figure 3.12. The highest change in resonance frequency was observed for the BC-CSRR

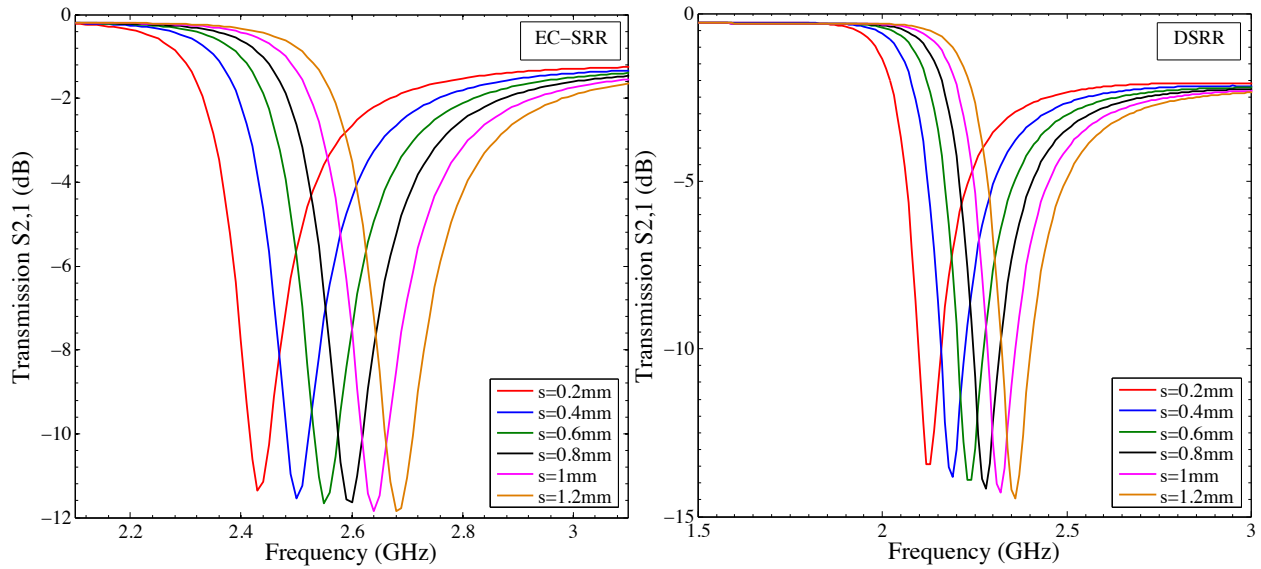


Figure 3.9: Transmission spectra, (a) EC-SRR structure (b) DSRR structure

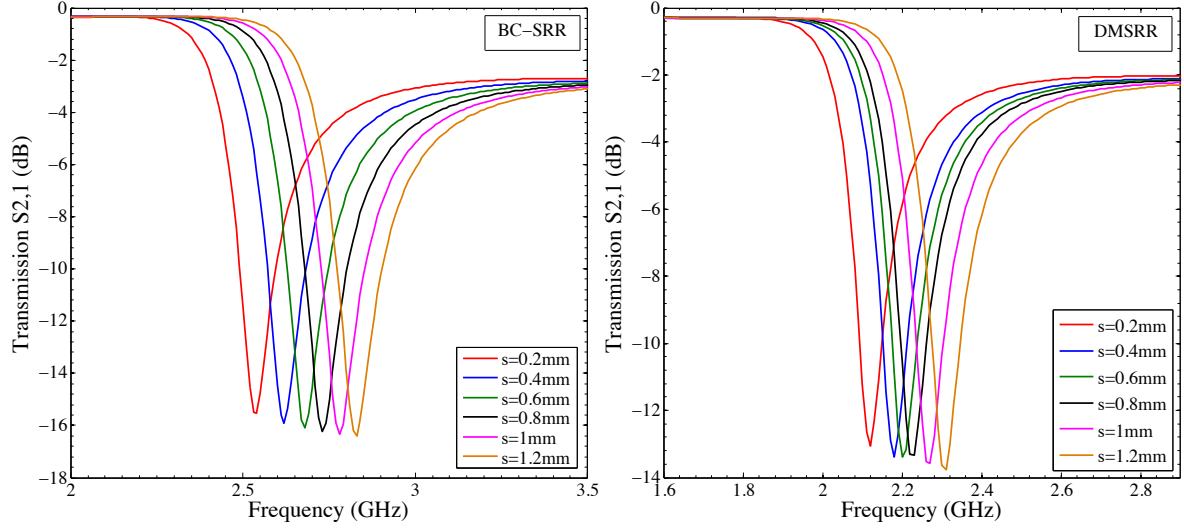


Figure 3.10: Transmission spectra, (a) BC-SRR structure (b) DMSRR structure

structure which shows a change of 470 MHz increase with 1 mm increase of the split gap. The BC-SRR structure displays a change of the resonance frequency from 2.54 to 2.83 GHz with a total change of 290 MHz. The least sensitive structure among these structures is the DMSRR, which shows a change of 190 MHz as the resonance frequency increases from 2.12 to 2.31 GHz. The EC-SRR and MSRR structure displays similar behavior and also has the resonance frequency values really close to each other. It is seen that the resonance frequency is reduced with the introduction of one additional SRR structure in the EC-SRR structure.

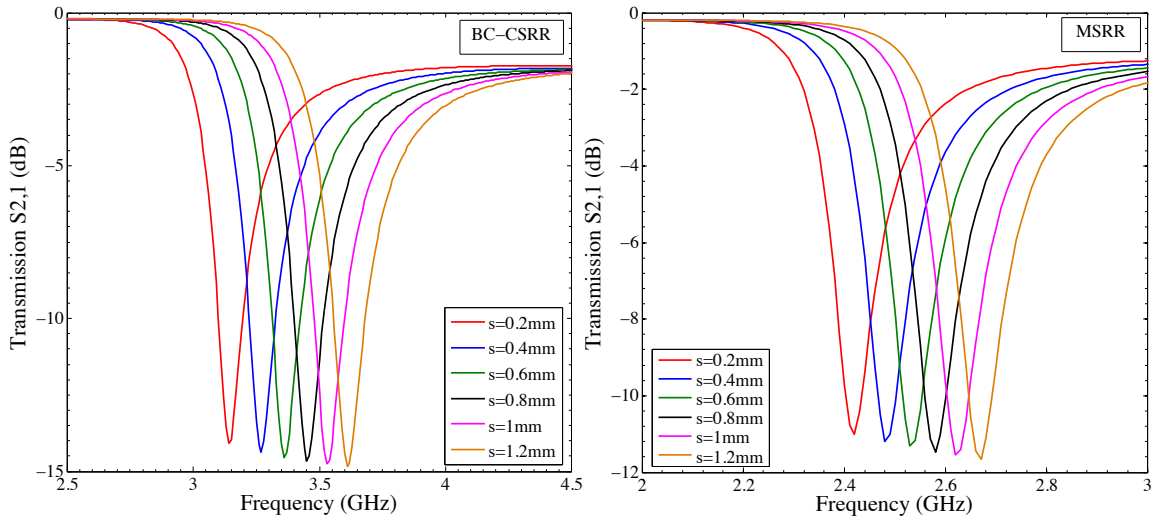


Figure 3.11: Transmission spectra, (a) BC-CSRR structure (b) MSRR structure

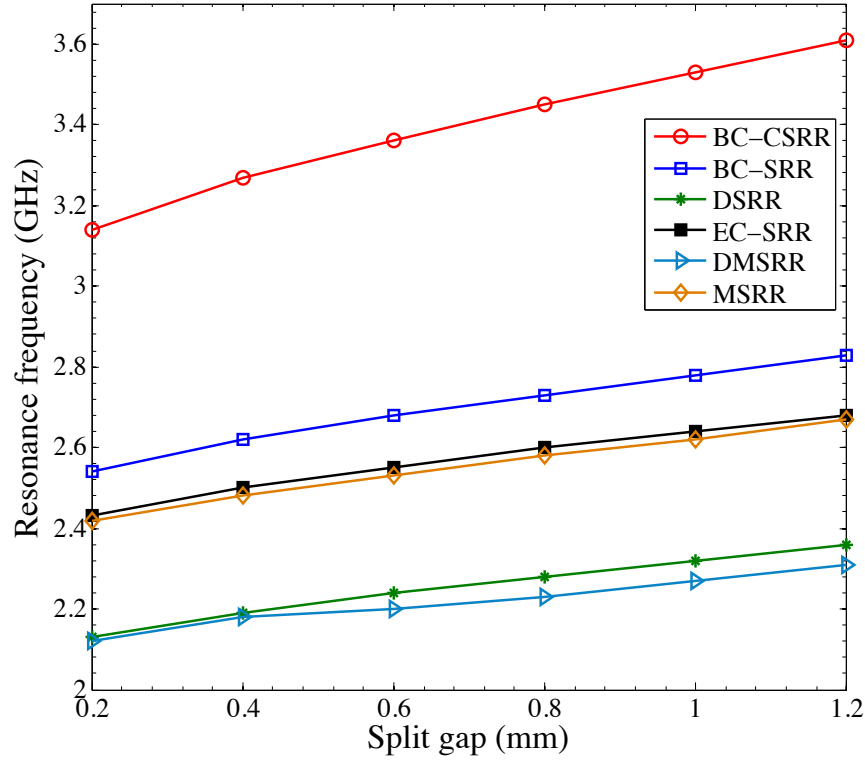


Figure 3.12: Effect of split gap on resonance frequency for different SRR structured units.

3.5 Effect of relative permittivity (ϵ_r) on the resonance frequency

To evaluate the temperature sensitivity of the sensor structures, standard dielectric constant of LiNbO_3 from 400 °C to 800 °C was taken into account [104], which varies from 52 to 145 within this temperature range. Using the dielectric constant of 52, 55, 65, 76, 87, 110 and 145 at temperatures 400 °C, 500 °C, 600 °C, 700 °C, 800 °C respectively, the temperature sensitivity of all the different structures was evaluated. All the structures show a decline in the resonance frequency with the increase of temperature. While CRR structure shows the highest resonance frequency values as expected, it also shows the highest sensitivity of 6.375 MHz/°C. The sensitivity for BC-CSRR, BC-SRR, DSRR, EC-SRR, DMSRR and MSRR structures are 1.475 MHz/°C, 1.15 MHz/°C, 0.975 MHz/°C, 1.125 MHz/°C, MHz/°C and 1.1 MHz/°C respectively. The transmission values for the CRR structures with different dielectric constant and comparison of the all structures are shown in Figure 3.13 (a) and (b) respectively.

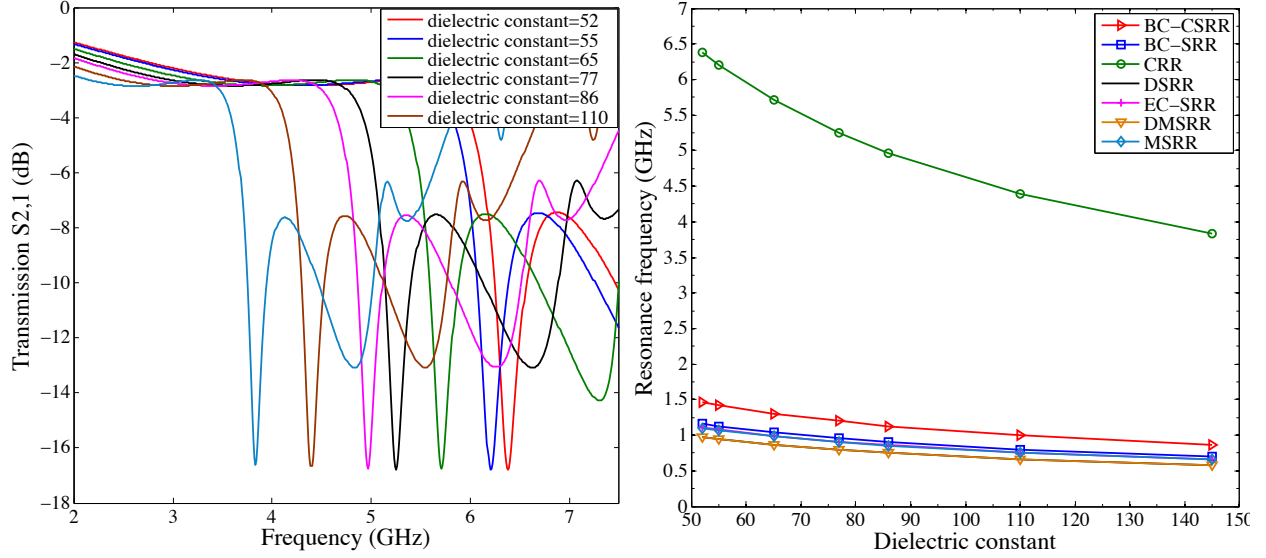


Figure 3.13: (a) Transmission spectra, CRR structure (b) Effect of dielectric constant on resonance frequency for different SRR structured units.

3.6 Comparison of the Electrical sizes of the sensor model with different SRR structure

Electrical size is a very important parameter for a metamaterial unit cell because smaller electrical size provides more effective medium approximation and more accuracy from the quasi-static analysis is also expected. The electrical size of the different structure can be calculated using equation (3.1) and to have a common base of comparison for all the structures, the resonance frequency values for dielectric constant of 145 from figure 3.13 (b) are used. It is observed that for all the substrate thickness and relative permittivity values DSRR and DMSRR structure has the smallest electrical size 0.016 while the CRR structure has the highest electrical size 0.108. The electrical size for the BC-CSRR, BC-SRR, EC-SRR, DMSRR and MSRR structure is 0.0246, 0.0198, 0.0186, and 0.0187 respectively. Electrical size of a resonator cell is defined as [105],

$$u = \frac{D}{\lambda_0} = \frac{D}{c/f_0} = f_0 \frac{D}{c} \quad (3.1)$$

Where, D = Maximum linear dimension of the resonator

= Diagonal of the square sample = 8.49 mm

λ_0 = Free space wavelength at the resonance frequency [105, 106]

c = Speed of light in vacuum = 3×10^8 m/s

f_0 = Resonance frequency of the resonator

3.7 Conclusion

Two CRR structure embedded in a dielectric ceramic matrix is proposed as a temperature sensor operable in high temperature and harsh environments. The use of CRR structure makes the fabrication cheap and simple as complex technique like lithography can be avoided. The feasibility of such sensor is validated through Finite Element Method using HFSS. In order to obtain the optimum dimensions, effect of substrate thickness and split gap was evaluated and also compared against other common metamaterial structures found in literature. A comparative analysis of the sensitivity of each structure was examined using the dielectric constant of LiNbO_3 at different temperatures. It was demonstrated that proposed CRR structure is highly sensitive to the change of temperature and hence really suitable as a temperature sensor.

Chapter 4: Fabrication

Two different fabrication methods were followed to fabricate a sensor unit with embedded CRR structures. The first method is a conventional powder compression method where a die and a punch were used to compress the dielectric ceramic powder. CRR structures were placed inside the ceramic matrix at an intermediate step and were compressed along with the powders. The first half of this chapter will discuss the detailed procedure and materials used for this fabrication method. The other method used is additive manufacturing since this method enables fabrication of components of complex geometry. Sensor units were fabricated by a binder jetting technology using ExOne M-lab system. At first, simple geometries were fabricated to characterize the properties of the materials and to obtain the optimum parameters for fabrication and then complicated parts were fabricated. The second part of this chapter will focus on the additive manufacturing method: the operation principle, material characterization and important parameters will be discussed. Scanning Electron Microscopy (SEM) was performed using TM-1000, Hitachi, Japan with an accelerating voltage of 15 kV. XRD analysis was obtained with Cu α radiation (D8, Bruker, Germany).

4.1 Fabrication using conventional die-punch assembly

Sensors with the CRR structure were fabricated through the conventional method of powder compression. For this method, two cylindrical dies comprising the diameter of 1 in. (Dayton Progress), 2.75 in. (Custom made) and a square die with a side of 2 in. (Across International) were used in order to achieve several geometries and sizes. Commercially available BaTiO₃ nanopowders with average particle sizes of 100 and 700 nm were used as the dielectric matrix due to its excellent properties such as a Curie temperature of 120°C [107] and a linear change of dielectric constant with temperature, as shown in Figure 4.1 that can be beneficial to the performance of the wireless sensor.

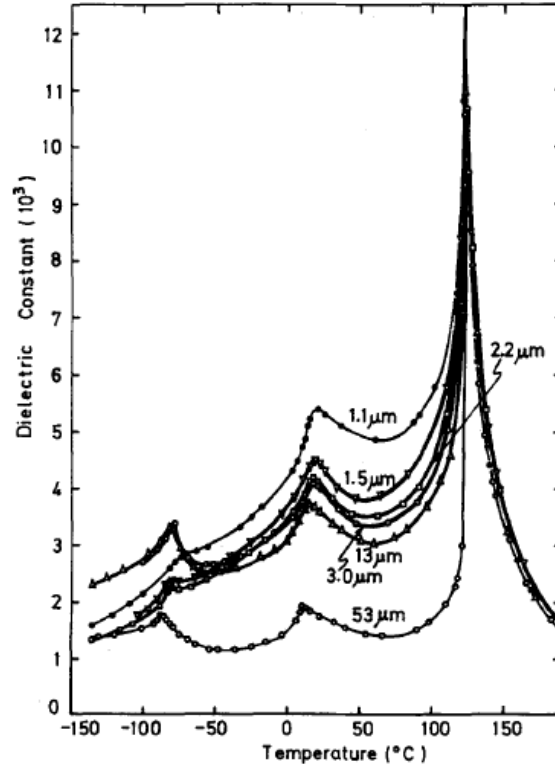


Figure 4.1: Temperature and grain size influence in BaTiO₃ properties [107]

Copper, aluminum and titanium were selected as the conductive materials due to their properties. Copper and aluminum were used for their low electrical resistivity, while titanium was considered due to its high melting point. Additionally, several ring dimensions were utilized in order to fully understand the variation of inductance with ring geometry. These properties play an important role in the operation of the sensor due to their influence in the quality (Q) factor. According to literature, lower resistivity and higher inductance improve the Q factor of the sensor [95]. Additionally, the variation of metal rings provided a better understanding of the response of the wireless sensor. In order to achieve an affordable solution, commercially available copper washers (McMaster) were employed for the CRR structure. Finally, polyvinyl alcohol (PVA) was used as the binding material in the dielectric ceramic in order to prevent cracking that can undermine the final properties of the sensor. The optimum amount of PVA was found experimentally through the 1-inch sample fabrication. The PVA concentration in the sample was gradually increased starting at 1% wt. of BTO in order to eliminate the cracking

found in the samples prior to the binder implementation. The optimal amount of binder was found to be 7.5% wt. of the BTO.

Table 4.1: Waveguide specifications

Name	Frequency range (GHz)	Length (mm)	Height (mm)	Width (mm)
WR62-Ku band	12.4 – 18.0	15.80	7.90	5.08
WR90-X band	8.2 – 12.4	22.86	10.16	7.62
WR430	1.72 – 2.6	109.22	54.61	35.56

4.1.1 Polyvinyl alcohol synthesis

Polyvinyl alcohol (99% hydrolyzed, Sigma Aldrich) was synthesized by mixing it with deionized (DI) water in a 1:10 ratio at a certain temperature. For this process, DI water was placed in a 250 mL beaker under heavy stirring (600 rpm) at room temperature. The PVA was added gradually in 0.1-gram intervals into the DI water until the ratio was reached. After that, the solution was heated to 90°C until the powder was fully dissolved into the water, showing a yellowish, semi-transparent color and then was cooled down in air to reach the room temperature.

4.1.2 Sensor fabrication

BaTiO₃ nanopowders were mixed in a mortar with 7.5% wt. PVA. The mixture was ground to achieve uniform binder distribution. After that, the ceramic/binder mixture was placed inside of the compressive die. Pressing the powder mixture by hand with a punch attained uniform thickness. The second and third layers of the BaTiO₃/PVA mixture were prepared following the process aforementioned. A copper washer was placed and centered inside of the die in between each of the ceramic layers, a schematic of the ceramic/washer configuration can be seen in Figure 4.2 (a). The die was then placed inside of a CARVER pressing machine and compressed using 3 metric ton pressure for 5 minutes, as seen in Figure 4.2 (b).

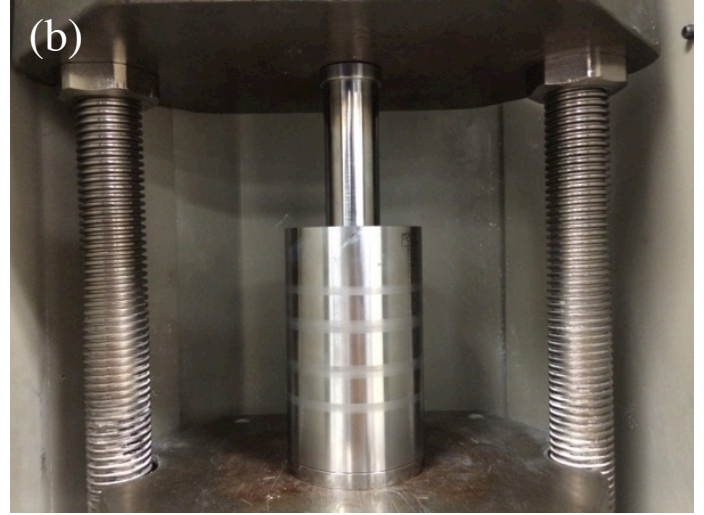
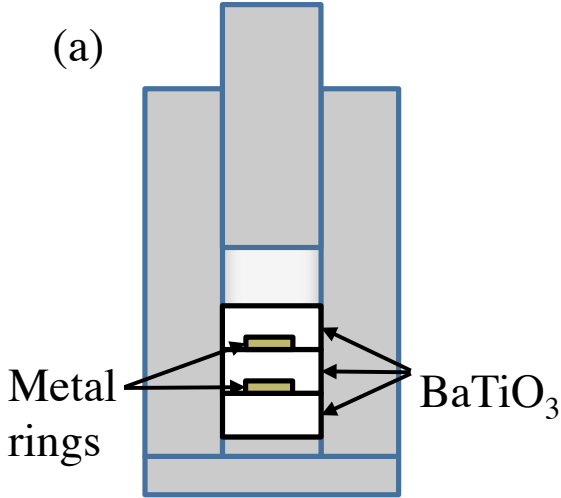


Figure 4.2: (a) Schematic of sensor architecture, (b) die placed inside of the pressing machine, prior to compression

After the compression was completed, the 1-inch samples were cured at a 150°C for 90 minutes, following a $5^\circ\text{C}/\text{min}$ ramp to accomplish better binder distribution and increase the rigidity of the wireless sensor. As mentioned before, aside from the 1-inch samples, 2.75-inch cylindrical and 2-inch squared samples were fabricated. For the 2.75-inch cylindrical samples and 2-inch samples, curing was not necessary as the samples were rigid enough for handling. The details for the fabricated samples can be found below. Table 4.2 shows the summary of the dimensions and characteristics of the samples. Additionally, Figures 4.3 through 4.10 show the samples fabricated using this method.

Table 4.2: Summary of fabricated samples

Sample No.	Matrix	No. Of Units	Diameter/Side Length (in)	Height (in)	CRR structure details
1	$\text{BaTiO}_3 - 7.5\%$ PVA	1	2.75	1/2	2 copper shims (OD: 3/8in, ID: 1/4in, t: 0.01in)
2	$\text{BaTiO}_3 - 7.5\%$ PVA	1	2.75	2/3	18 copper washers (OD: 7 mm, ID: 3.23 mm, t: 0.5 mm)

3	$\text{BaTiO}_3 - 7.5$ % PVA	1	2.75	1/2	4 titanium washers (OD: 5/8", ID: 3/16", t: 0.04")
4	$\text{BaTiO}_3 - 7.0$ % PVA	1	2.75	1/8	2 copper shims (OD: 3/8", ID: 1/4", t: 0.005")
5	$\text{BaTiO}_3 - 7.5$ % PVA	1	2.75	1/4	2 copper shims (OD: 3/8", ID: 1/4", t: 0.005") (each)
6	$\text{BaTiO}_3 - 7.5$ % PVA	4	2	1/4	2 copper washers (OD: 1/4", ID: 1/8", t: 0.02") (each)
7	$\text{BaTiO}_3 - 7.5$ % PVA	4	2	1/4	2 aluminum washers (OD: 3/8", ID: 1/4", t: 0.005") (each)
8	$\text{BaTiO}_3 - 7.5$ % PVA	2	2	1/4	2 copper washers (OD: 1/2", ID: 0.203", t: 0.03") (each)

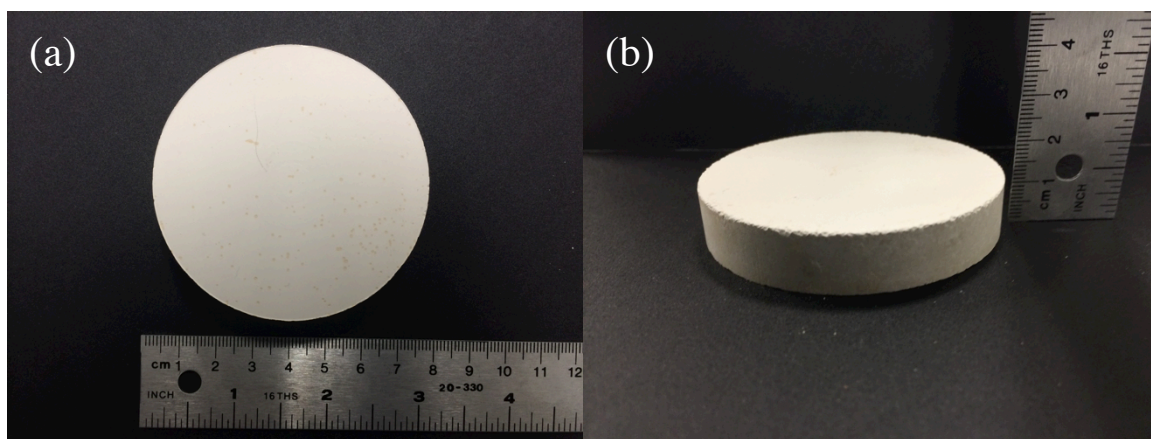


Figure 4.3: Sample 1, (a) top view, (b) 3D view

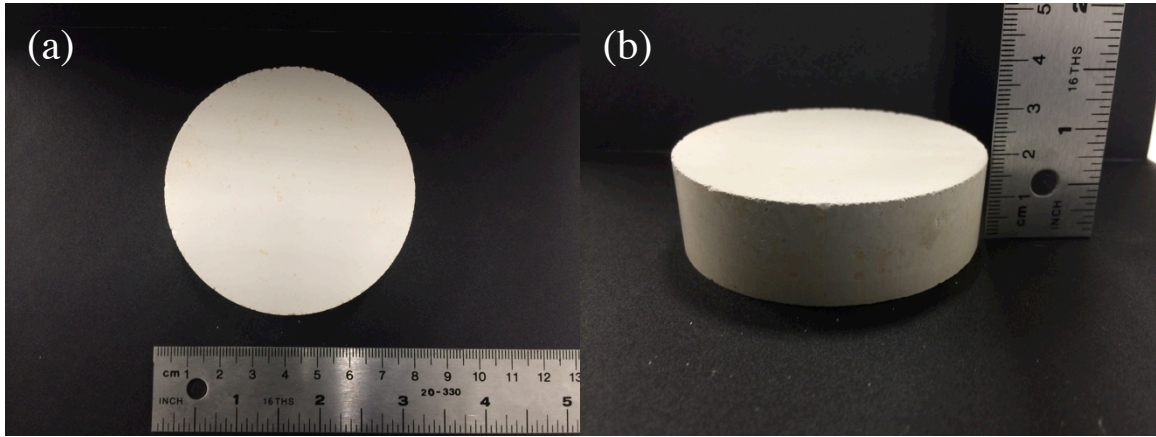


Figure 4.4: Sample 2, (a) top view, (b) 3D view

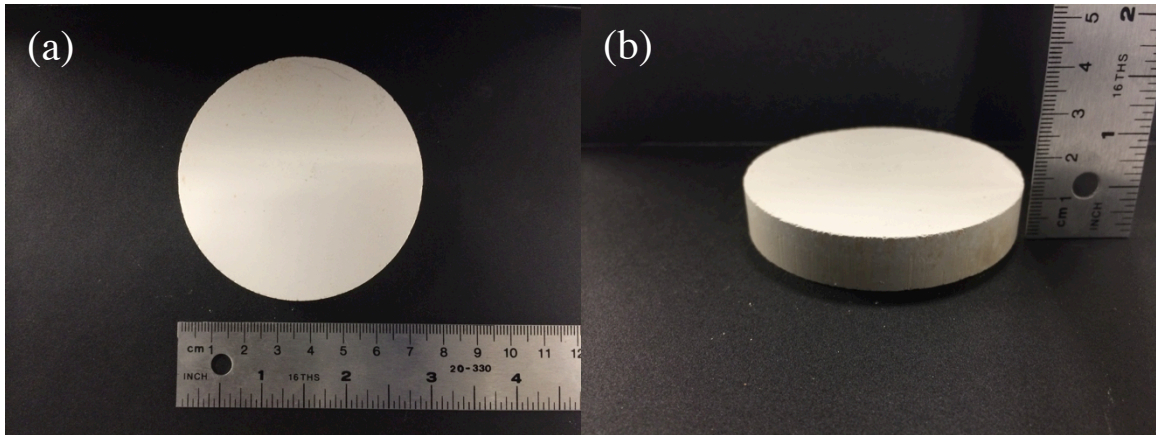


Figure 4.5: Sample 3, (a) top view, (b) 3D view

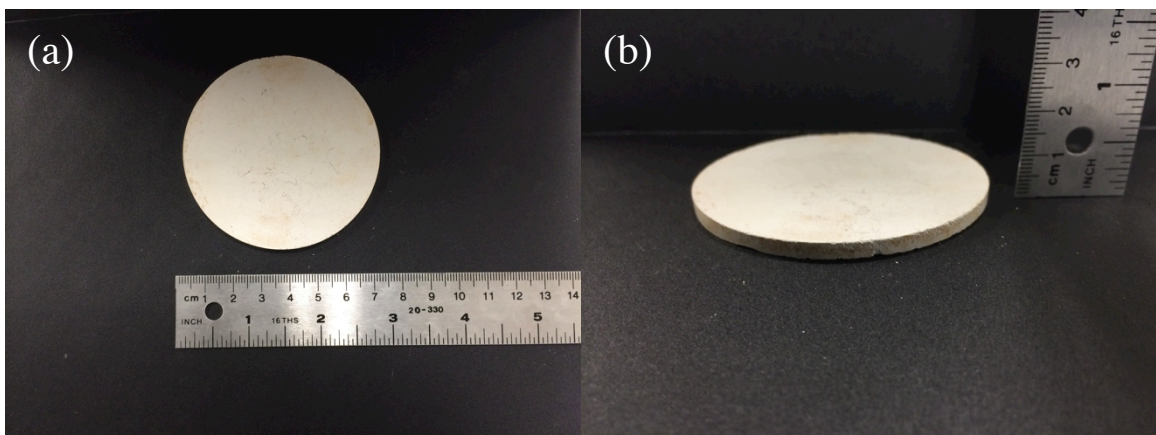


Figure 4.6: Sample 4, (a) top view, (b) 3D view

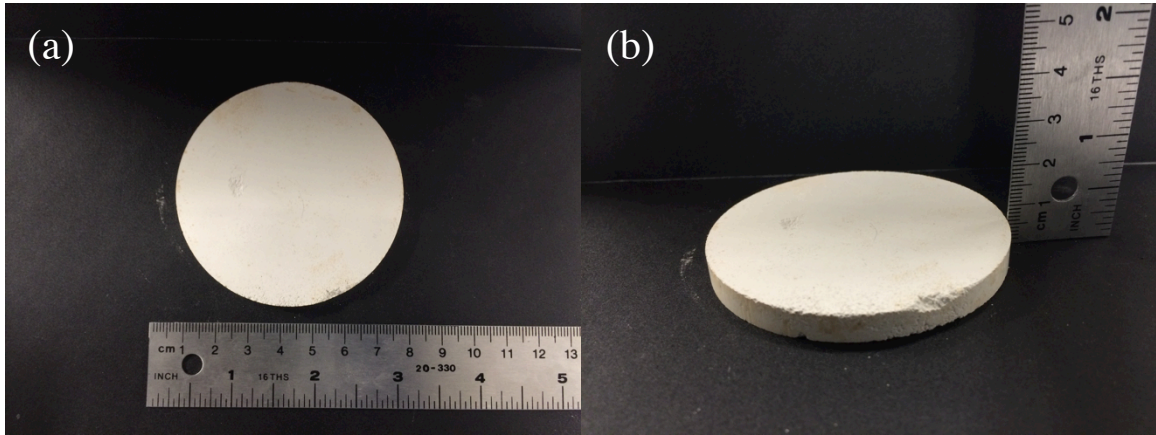


Figure 4.7: Sample 5, (a) top view, (b) 3D view

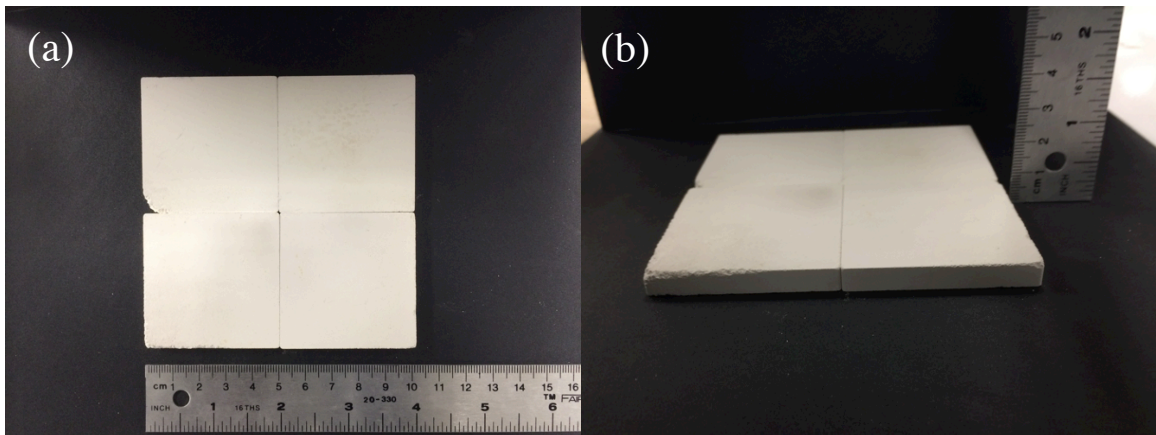


Figure 4.8: Sample 6, (a) top view, (b) 3D view

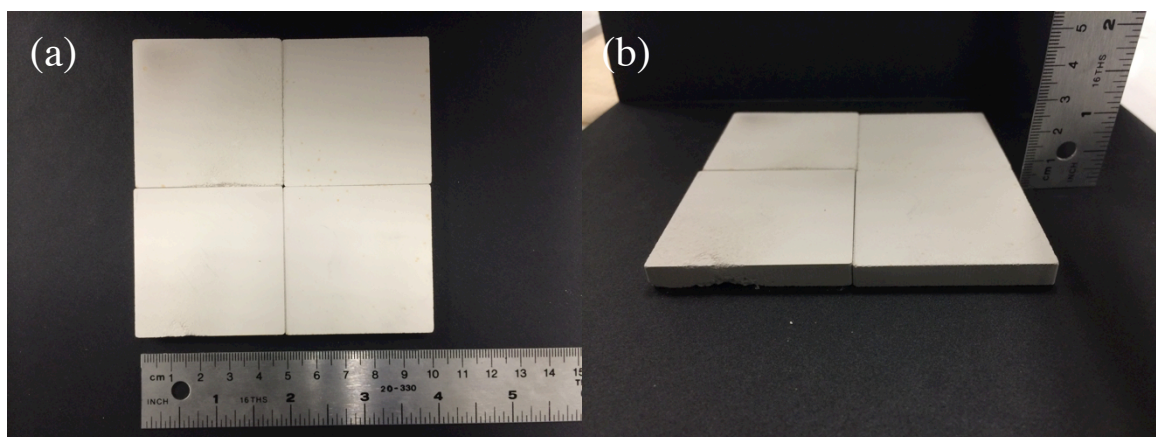


Figure 4.9: Sample 7, (a) top view, (b) 3D view

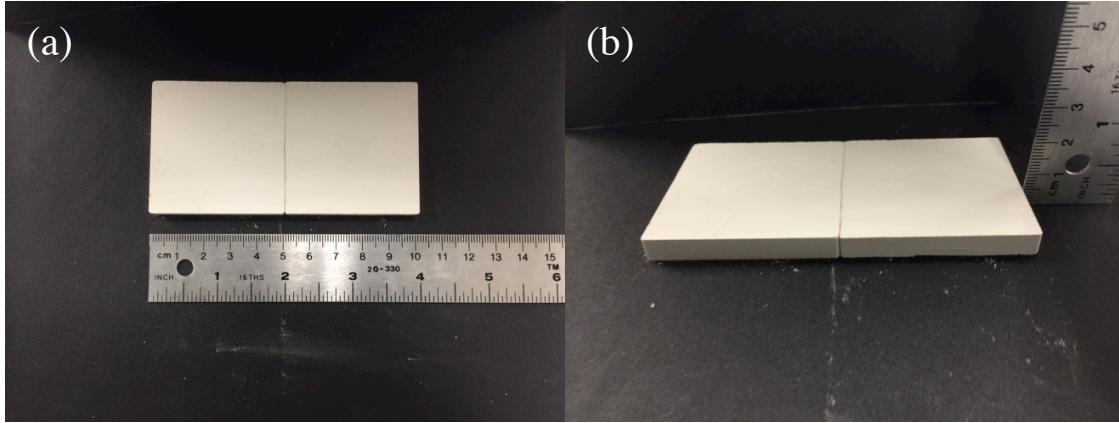


Figure 4.10: Sample 8, (a) top view, (b) 3D view

4.1.3 Sample polishing

In order to do the waveguide testing using the Ku and X bands, the 1-inch samples were polished to the needed dimensions, portrayed in Table 4.1. For the polishing, waterproof silicon carbide sand papers were utilized. Grits 120, 180, 220, 320, 1000 were used subsequently to achieve a smooth finish. Low revolution (200 rpm) spinning was utilized throughout the polishing process to achieve higher control over the dimensions and the finishing of the sample. Figure 4.11 shows two samples polished for the X band dimensions, prepared with a mixture of BaTiO_3 and 7.5% PVA. For this samples, the CRR structure was comprised of titanium washers with an outer diameter of 3/16 inches, an inner diameter of 3/32 inches and a thickness of 0.01 to 0.03 inches.

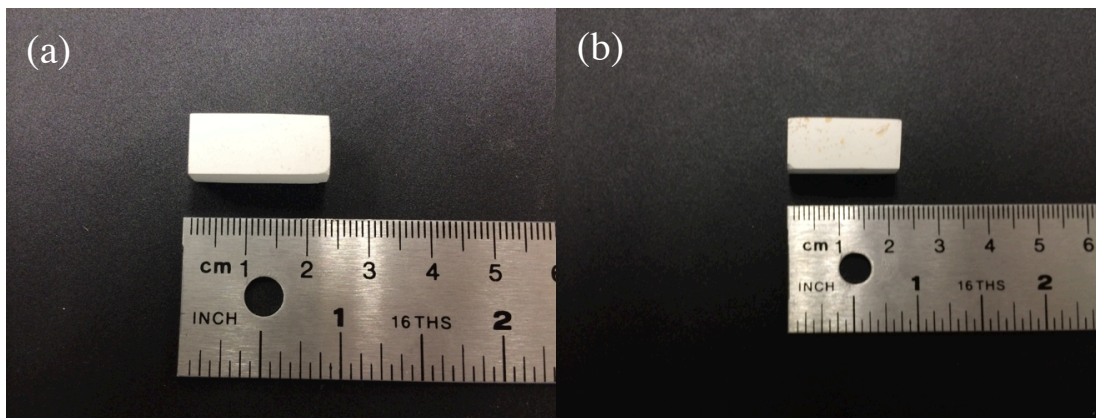


Figure 4.11: Samples polished for X band testing. Both (a) and (b) were fabricated under the same characteristics

4.2 Fabrication using 3D printing

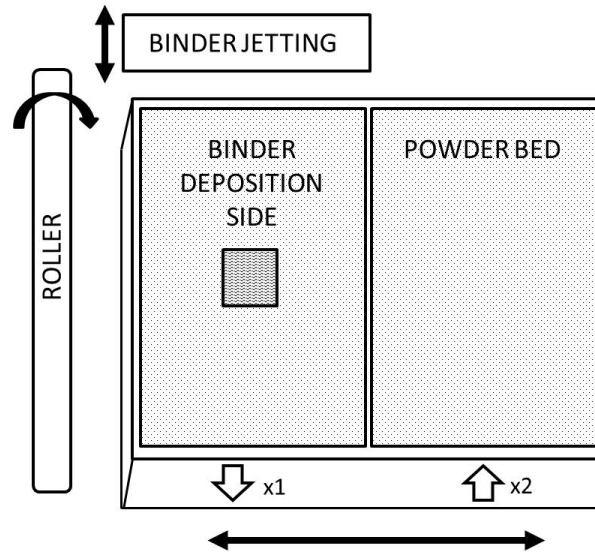


Figure 4.12: Schematic of powder bed system [108]

ExOne M-lab system, a binder-jetting technology that builds three-dimensional objects in a layer-by-layer fashion was used to fabricate the ceramic parts required for the sensor. The M-lab system consists of a two bed-system as shown in the schematic in Figure 4.12. Build dimensions are 40x60x15mm. One bed is for the build powder material and the other one is for part fabrication, where two layers are used from the powder bed to accommodate a single layer in the fabrication bed, this is performed to accomplish better powder packing. Designs for the part files can be made using any commercial CAD software and has to be uploaded to the system as an *.stl* file, which converts the 3D part into a layer-by-layer arrangement readable by the system. While building a part, powder layers are spread by a roller from the powder bed to the binder deposition side as the bed moves mechanically from left to right in the x-direction. Once there is a uniform layer of powders, binder droplets are deposited over that layer according to the design provided. Then the system waits for several minutes to allow drying of the binder, after that another layer of powders is spread and the aforementioned steps are repeated until the part is done. Once the part is complete, the fabrication bed is placed inside an oven at 195 °C for 2 hours to cure the binder. After curing, the fabrication bed is removed and cleaning of the parts

takes place. When the parts are ready they can be sintered or infiltrated with a different material according to the specific need.

Initially, BaTiO_3 (BTO) was chosen as the dielectric material because of its properties as mentioned in section 2.1. BTO powder was purchased from Acros Organics through Fischer Scientific and powder particles were approximately $1\ \mu\text{m}$ in diameter, while agglomerations were up to $10\ \mu\text{m}$ as can be estimated from Figure 4.13.

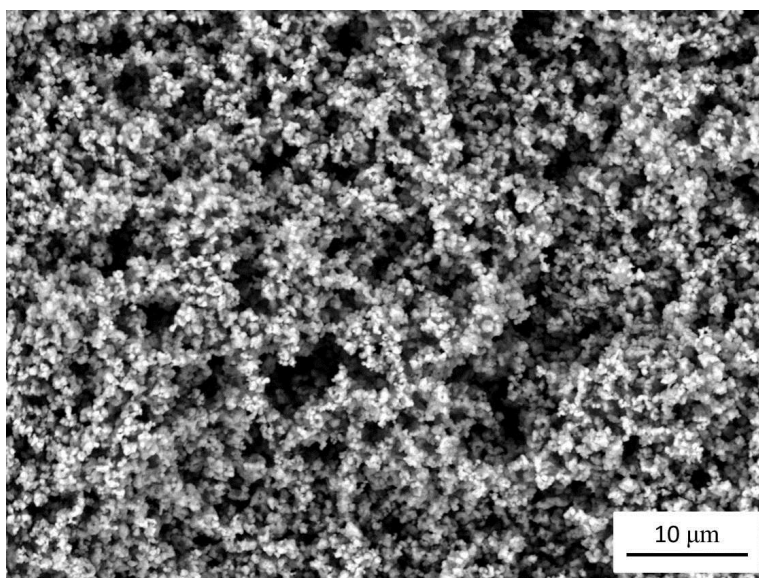


Figure 4.13: As received BTO powder [108]

To obtain the optimum result, different building parameters were used and post-sintering density was compared. The binder saturations used were 60, 75, 100 and 120%. Binder saturation can be defined as the ratio of the deposited binder solution volume to the pore volume in the powder bed for a given layer thickness [109]. Since layer thickness is based on powder size, initially a $15\ \mu\text{m}$ thickness was used, but as the samples were breaking in small pieces after binder curing, the layer thickness was doubled to $30\ \mu\text{m}$, regardless of powder size. A high temperature cyclic furnace was used for all sintering temperatures. Different sintering profiles were followed to find out the optimum profile that achieves the highest density. For all the sintering profiles, the heating ramp rate was chosen to be $10\ ^\circ\text{C}/\text{min}$ for all the steps. To ensure

the binder burnout, samples were held at 600 °C for 0.3 hours and 0.5 hours while heating up and cooling down respectively. The complete steps for different sintering profiles are shown in Figure 4.14. After the samples were heated up to the maximum temperature according to the profile, they were left inside the furnace to avoid faster cooling rates.

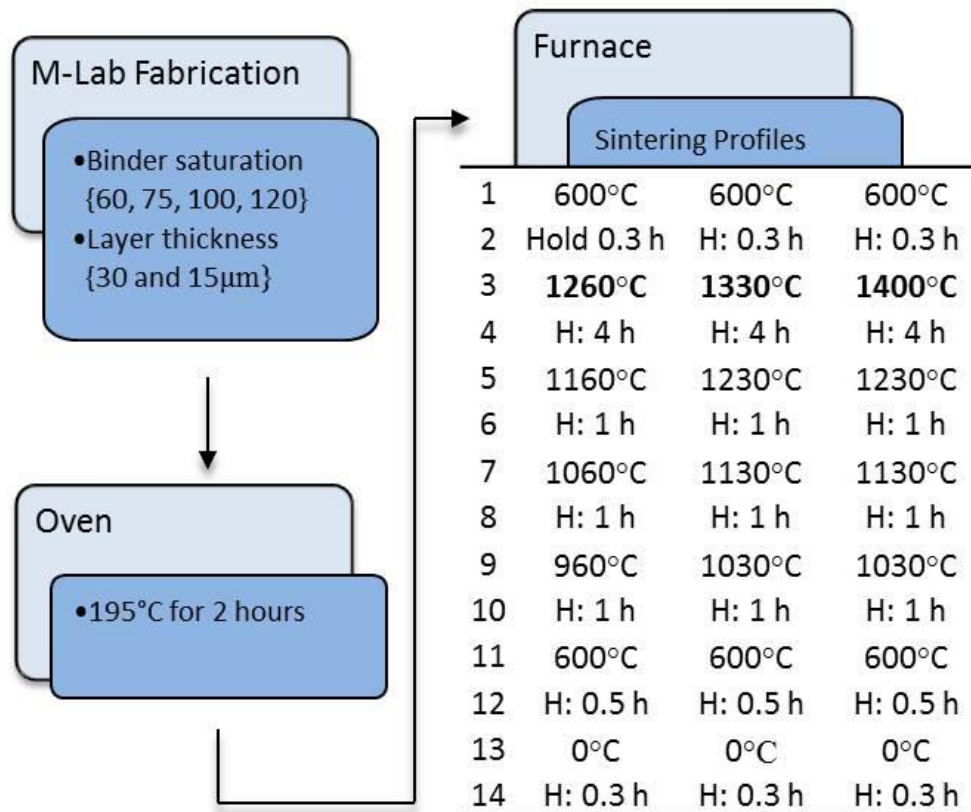


Figure 4.14: Different temperature profiles used for sintering fabricated parts [108]

ASTM B962-08 standard test method, which uses the Archimides' principle, was followed to obtain the density values. A Mettler Toledo MS303S precision scale was used to measure the weight of the sample while a copper mesh was used to hold the samples in place. The samples were impregnated with olive oil to seal the surface porosity and avoid water adsorption through the pores. Then, they were immersed in water and weighed. A drop of soap was dissolved in water to reduce surface tension. Water was at room temperature (~ 22 °C). Therefore, two different densities were measured for one sample. One is referred to as sintered

(as removed from the furnace after sintering without any additional processing) and the other is referred to as impregnated (dipped in oil at a pressure of 7 kPa for 30 min) from hereafter. A comparison of the different densities obtained by different sintering profile and binder saturations are plotted in Figure 4.15 for both sintered and impregnated samples. Each data point in Figure 4.15 represents the average value of five measured densities. The highest density was achieved for the sintering profile of 1260 °C and for 60% binder saturation for both sintered and impregnated samples, and the values are 1.3 g/cm³ and 1.6 g/cm³ respectively.

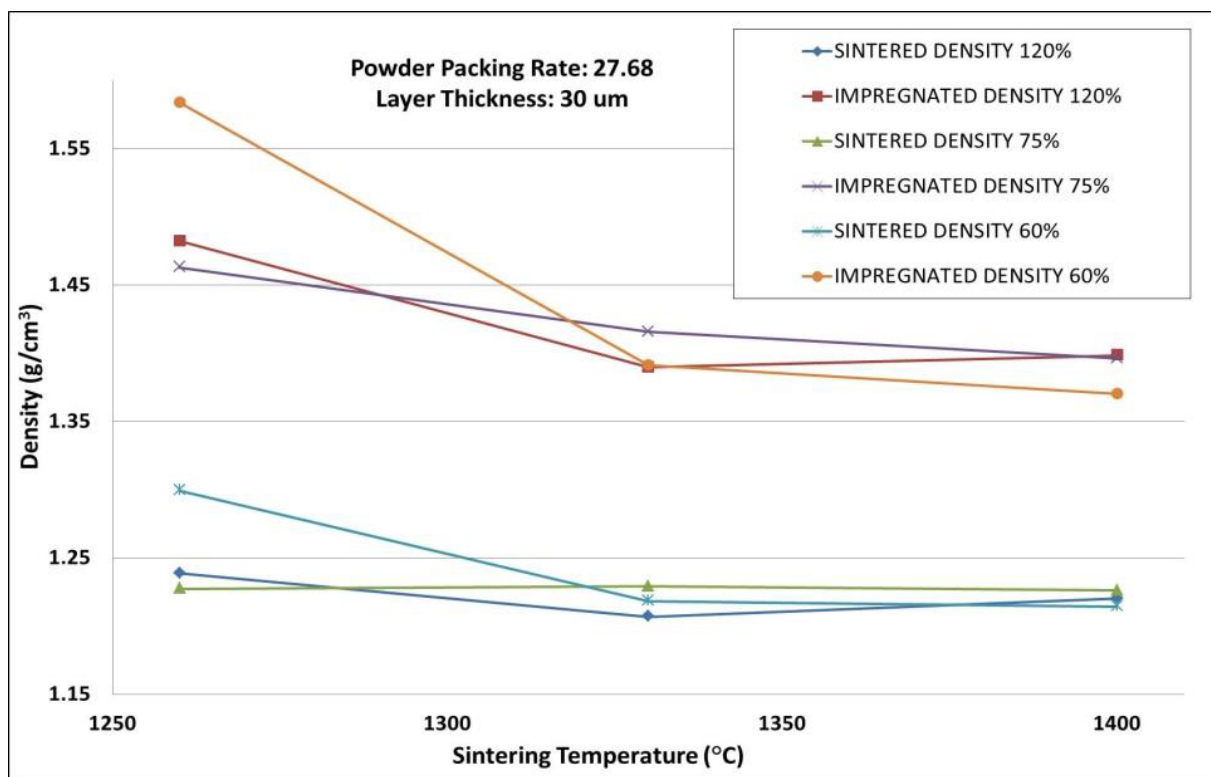


Figure 4.15: Density vs sintering temperature for different binder saturations [108]

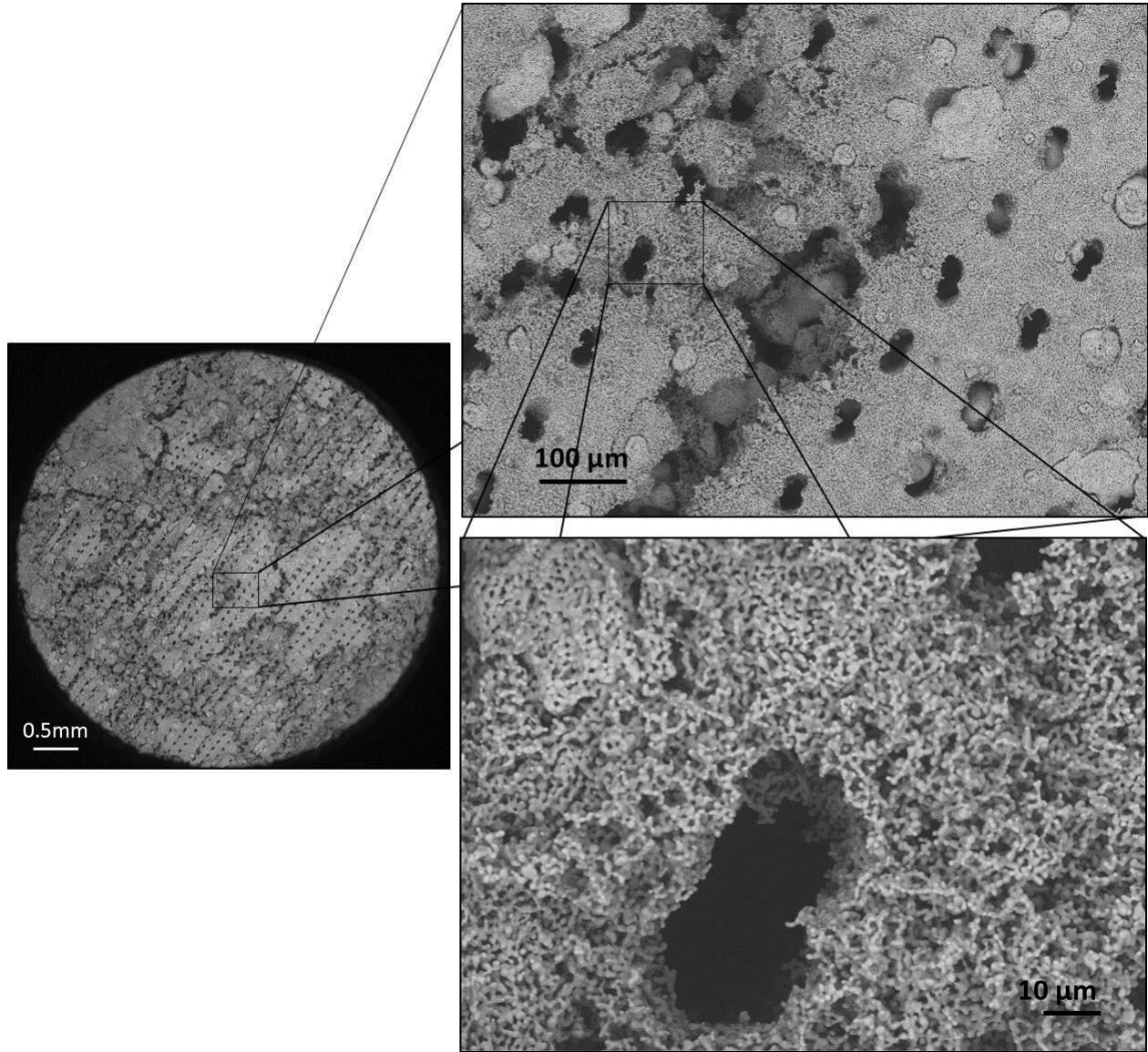


Figure 4.16: Set of magnified images (a) to (c) of sample fabricated with 60% binder saturation, layer thickness of 30 μm and sintered at 1200 $^{\circ}\text{C}$ for 4 hours [108]

The reason behind the low density obtained by sintering is believed to be the absence of pressuring force while sintering. Nonetheless, binder saturation plays an important role as well. To further investigate these results, samples fabricated with 60% binder saturation and a layer thickness of 30 μm were sintered at 1200 $^{\circ}\text{C}$ for a total of four hours and the surface was analyzed. It can be observed in Figure 4.16 (a), (b), and (c) that binder has already burned out (binder burn out takes place at ~ 600 $^{\circ}\text{C}$), and empty spaces of 60 μm length and 20 μm width

were left behind. Therefore, to obtain a denser part BTO grain growth has to cover these empty spaces left behind after the binder burnout. Since, the intricacy of the 3D fabricated parts does not allow applying force while sintering, as the complex parts would lose their shape, samples sintered at higher temperatures were evaluated. Figure 4.17, 4.18 and 4.19 show the SEM images of samples fabricated with 60% binder saturation and layer thickness of 30 μm and that were sintered at 1260 $^{\circ}\text{C}$, 1330 $^{\circ}\text{C}$ and 1400 $^{\circ}\text{C}$ respectively.

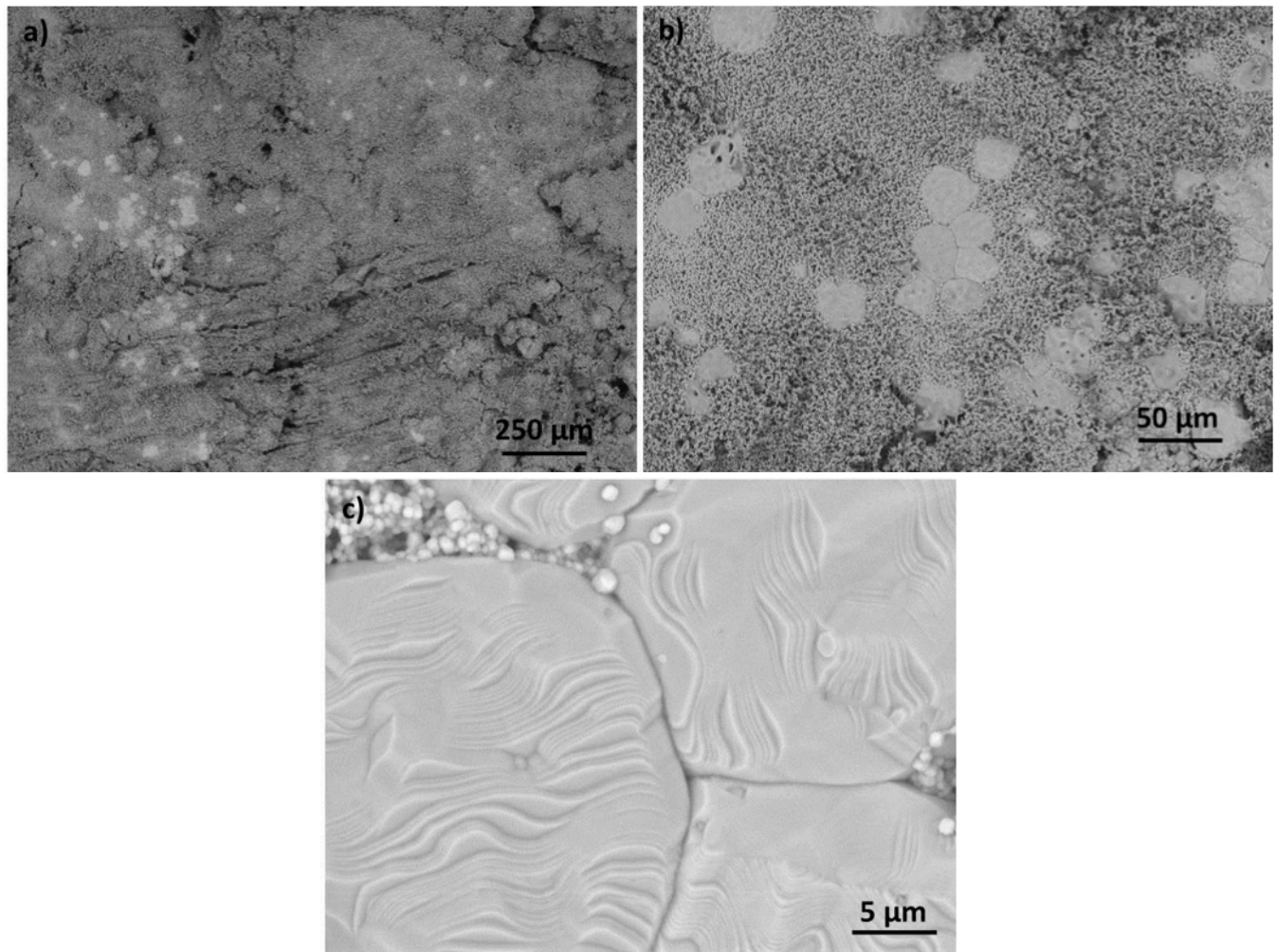


Figure 4.17: Set of magnified images (a) to (c) of sample fabricated with 60% binder saturation, layer thickness of 30 μm and sintered at 1260 $^{\circ}\text{C}$ for four hours [108]

It can be observed from Figure 4.17 (c) that grain size values range from 25 to 40 μm , and space between grains is fully enclosed. However, from Figure 4.17 (a) and (b) it is obvious

that most of the powder did not achieve a good grain growth and the size remained unchanged. Figure 4.18 and 4.19 show more sintered powder compared to samples sintered at 1260 °C, but wider gaps in the grain boundaries are observed. Densification during sintering mainly happens by two types of mechanisms,

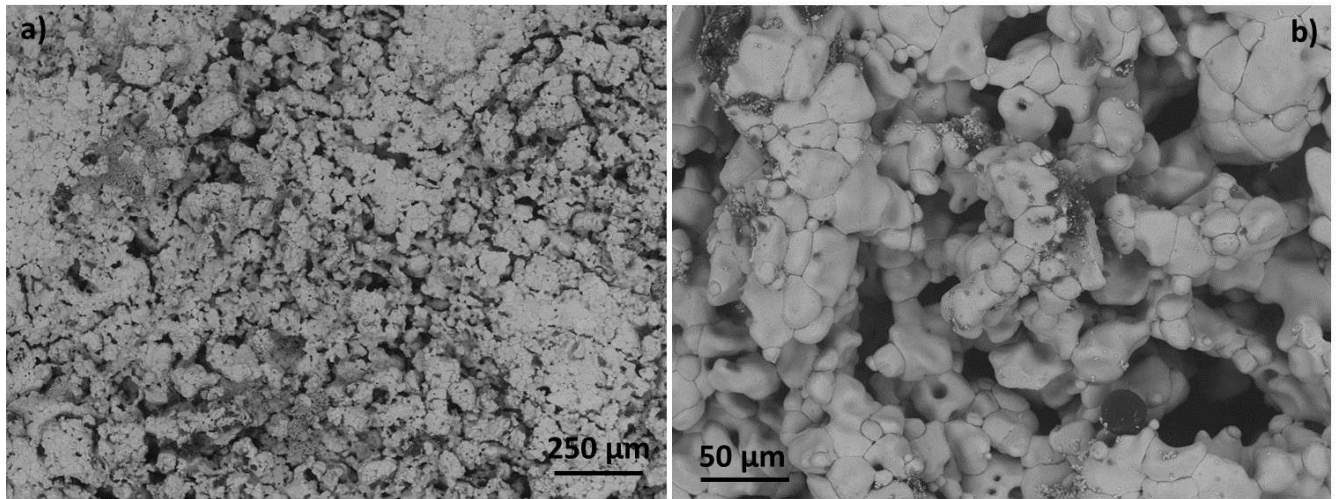


Figure 4.18: Set of magnified images (a) and (b) of sample fabricated with 60% binder saturation, layer thickness of 30μm and sintered at 1330°C for four hours [108]

lattice diffusion and grain boundary diffusion, and solid state sintering usually consists of three stages: 1) initial: involves necking and grain growth, 2) intermediate: results in shrinkage and densification, and 3) final: elimination of close pores and formation of dense microstructure [110]. It can be inferred from Figure 4.17 to 4.19 that these samples mostly reached the initial stage of sintering, where grain growth is occurring but it's not uniform. Stage two was also partially observed since samples had considerable shrinkage after sintering. Therefore, further research needs to be conducted to find out the proper sintering behavior of BTO fabricated by the M-lab system.

Since samples sintered at 1260 °C provided the highest density among the three temperatures used, XRD analysis was done on the samples sintered at 1260 °C and fabricated with 60% binder saturation. It should be noted that transition temperatures for BTO from tetragonal crystal structure to

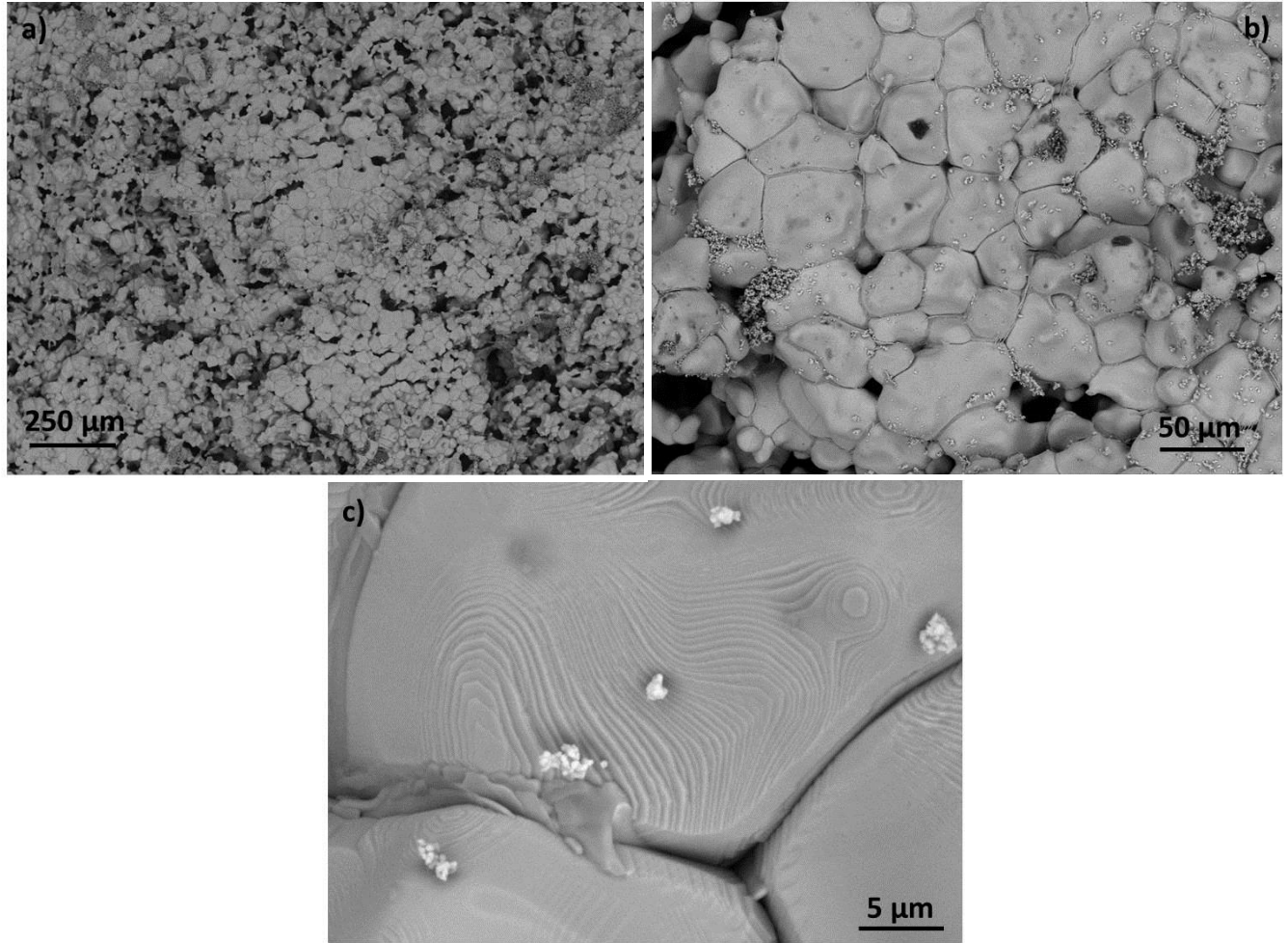


Figure 4.19: Set of magnified images a) to c) of sample fabricated with 60% binder saturation, layer thickness of 30 μ m and sintered at 1400 $^{\circ}$ C for four hours [108]

cubic is 130 $^{\circ}$ C and from cubic to hexagonal is 1460 $^{\circ}$ C. While tetragonal crystal structure of BTO shows both polarity and ferroelectricity, BTO with hexagonal crystal structure is not ferroelectric anymore [110]. XRD analysis results show that (Figure 4.20) as purchased BTO powder used to fabricate the parts consisted of mostly tetragonal structure with the presence of cubic phase. Nonetheless, after a sintering cycle of 1260 $^{\circ}$ C for four hours, the presence of a hexagonal peak in the [110] direction at $2\theta=42.8^{\circ}$. According to Chen et al. [111], solid state sintering leads to the cubic phase while cooling, and each grain formed is tightly packed with the surrounding neighboring grains and the orientations of the grains are random which explains the tight space between grains in Figure 4.17. A similar result was described by Gao et al. [112],

where an inclination to transform from tetragonal to cubic phase was observed while sintering BTO powder at 1250 °C.

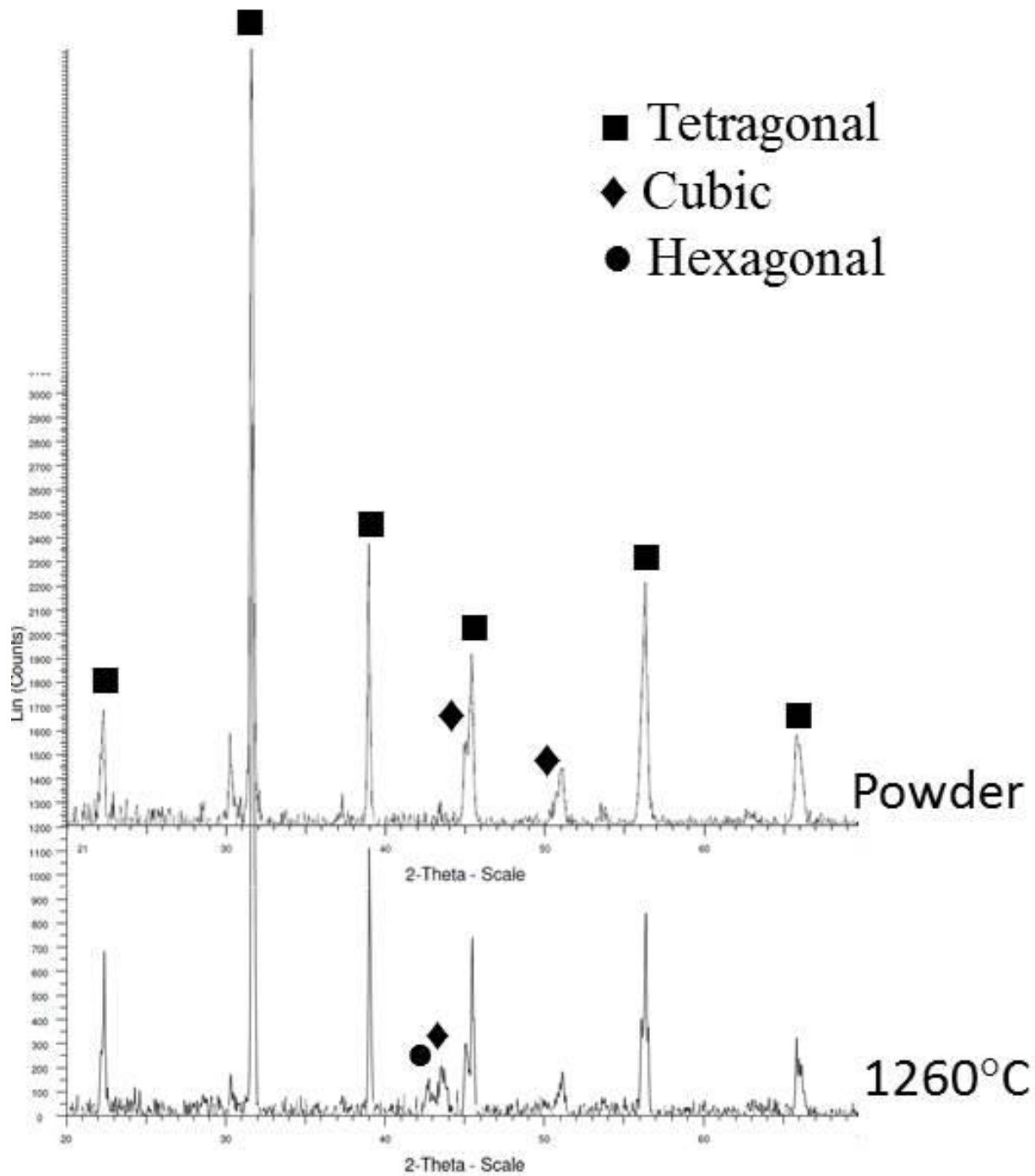


Figure 4.20: XRD analysis of as-received powder and sample sintered at 1260 °C for four hours [108]

Another important change that was observed in the sintered samples was shrinkage, which happened in all x, y and z directions and for all the sintering profiles used. Figure 4.21 compares the shrinkage in each direction with regards to the maximum sintering temperature used. It was noticed that the shrinkage was minimum for the samples sintered at 1260 °C and it was maximum for the samples sintered at 1400 °C and it was true for shrinkage in all directions.

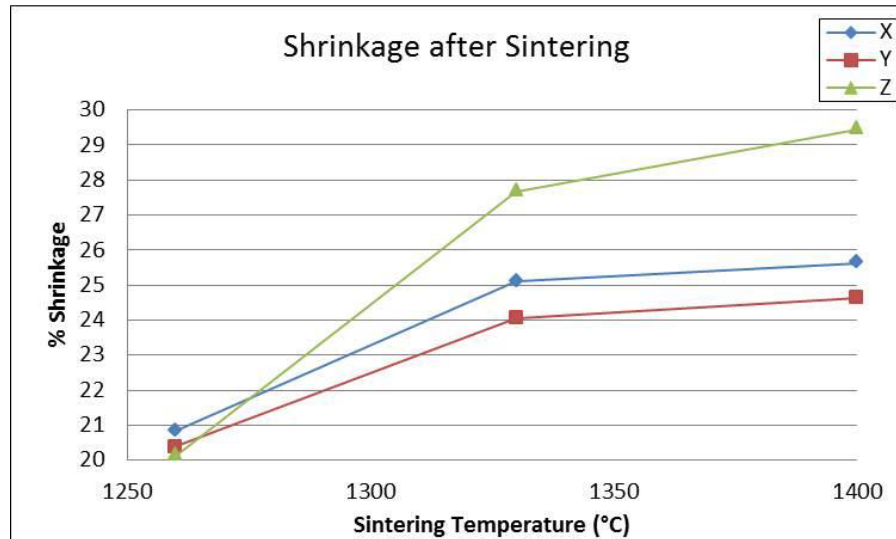


Figure 4.21: Graph depicting shrinkage percentage in each direction vs sintering temperature [108]

Since, the sensor will contain two CRR structures embedded inside a BTO matrix, several approaches were tried to find the optimum setup for that. Commercially available metal washers were used as the CRR structure. Inserting a CRR structure by pausing the building process and then continuing the rest of the building process was tried but the part cracked after curing at the location of the washer. Therefore, a new plan was devised to make two separate parts: one male part with extrusions and one female part with holes. A washer would be placed in the center hole and other extrusions were designed to properly attach and hold two parts together as shown in Figure 4.21. Binder saturation and layer thickness was taken as 60% and 30 μm respectively as proven to be the best settings for BTO as discussed previously. The

fabricated parts were sintered at 1260 °C for four hours as this sintering profile achieved the minimum shrinkage and maximum density compared to the other two profiles used.

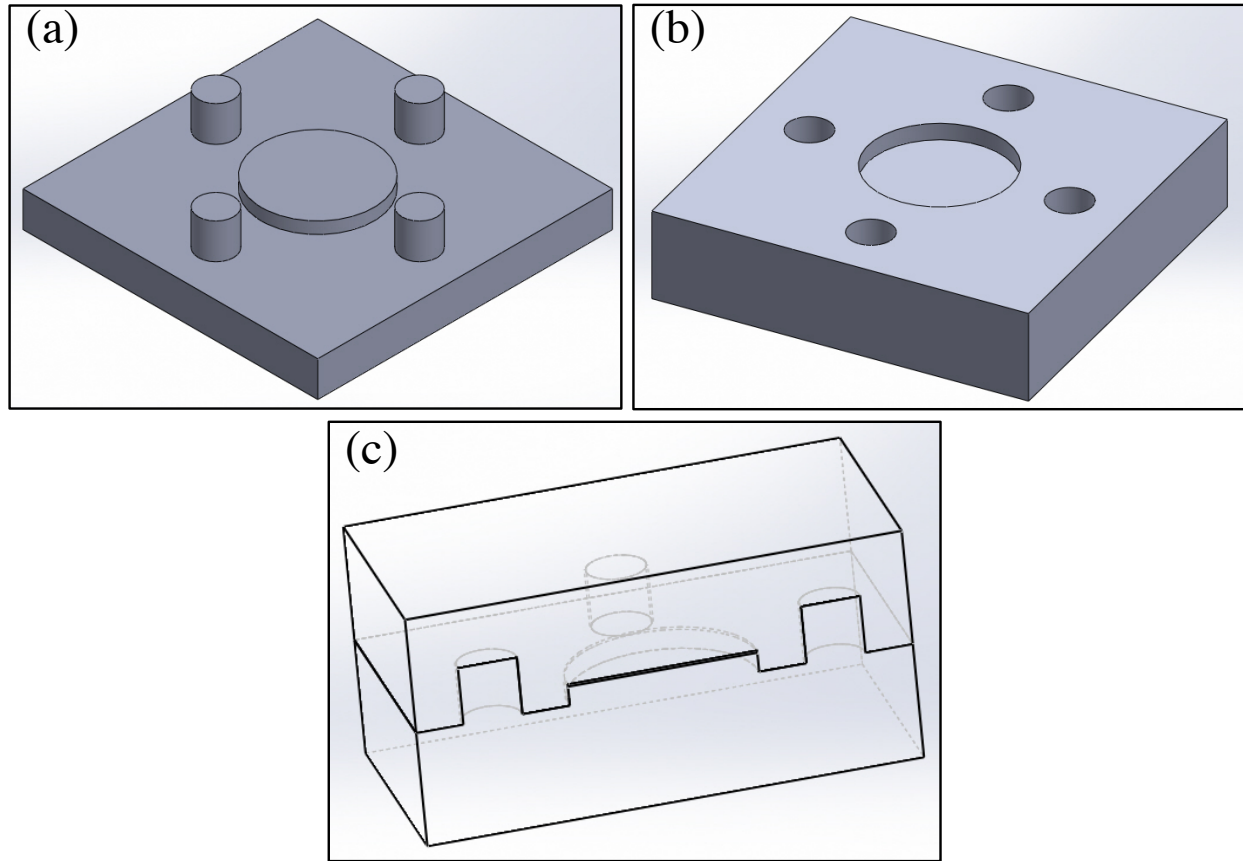


Figure 4.22: CAD design of (a) Male part with extrusions (b) Female part with holes (c) Section view of the assembly



Figure 4.23: Fabricated male and female parts with BTO, sintered at 1260 °C for four hours

From Figure 4.23, it can be seen that the fabricated BTO samples were cracked on one side, also the extrusions are not well defined, and there are cracks beneath them as well. More samples were made with the same settings and different binder saturations. Different sintering profiles were used, but none of them provided expected results. Finally, the failure was attributed to the particle size of the raw BTO powder used in this process since it was smaller than the recommended powder particle size for the ExONE M-lab system (1 μ m vs 60 μ m). Since difficulties were faced obtaining BTO powders with the recommended particle size, a new material with the particle size close to the recommended value (alumina, Al₂O₃) was used.

The alumina powder used had larger particle size compared to the BTO used before. The particle size ranged from 50 μ m to 100 μ m, which falls in the recommended particle size range, which is 50 μ m to 120 μ m. The same binder saturation (60%) was used with this powder as well, but, as it has larger particle size than the BTO, a thicker layer thickness (60 μ m) was used. The male and female parts fabricated with alumina were more consistent than the BTO ones in terms of crack and dimensional accuracy. The as built un-sintered samples showed stronger components when compared to the as built un-sintered BTO samples. Figure 4.25 (a) and (b) shows fabricated alumina male and female parts before and after sintering at 1600 °C for 4 hours.

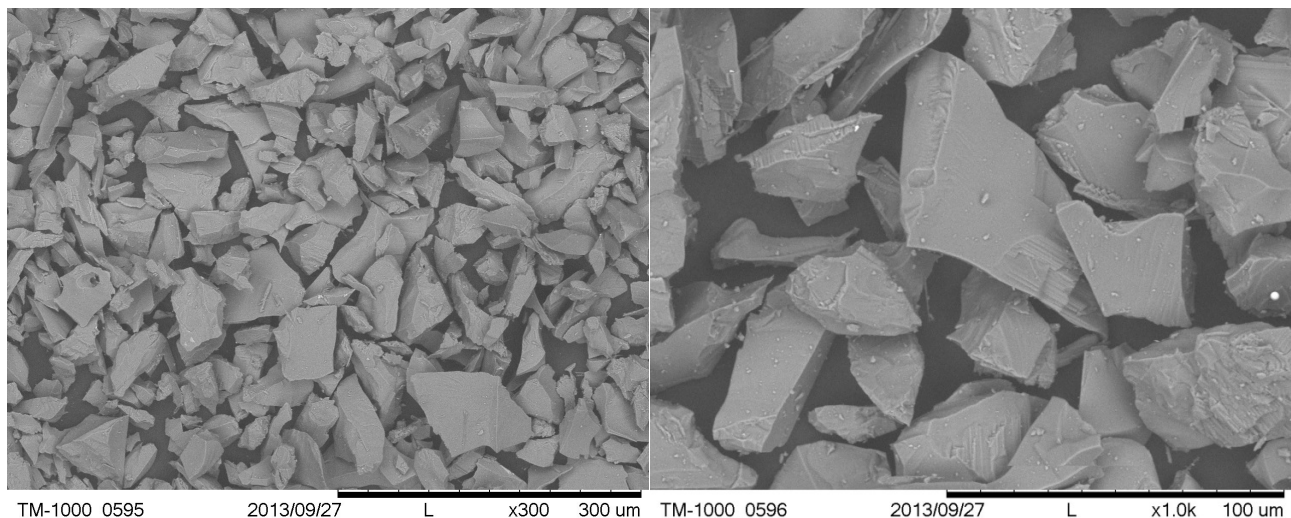


Figure 4.24: SEM image of raw alumina powder at different magnifications

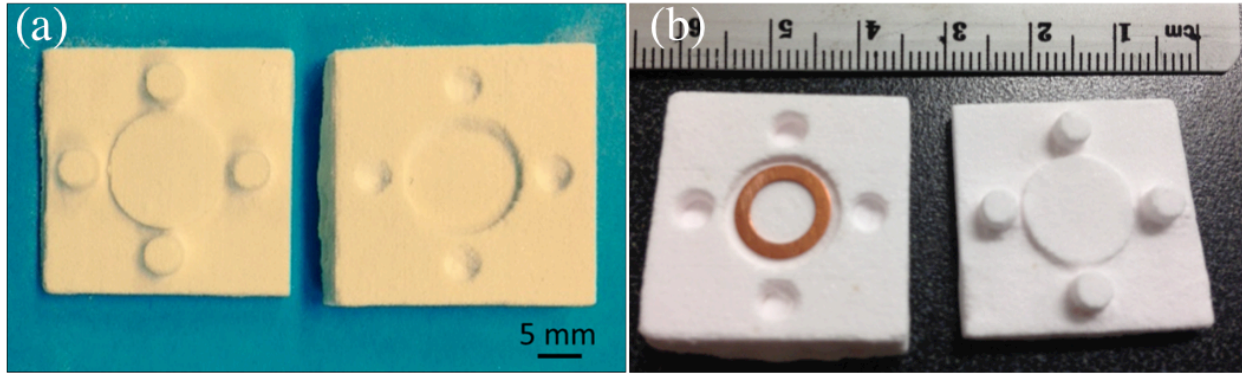


Figure 4.25: Fabricated male and female parts using alumina (a) before sintering and (b) after sintering at 1680 °C for 4 hours

After the successful building of male and female parts using alumina, it was decided to fabricate parts that are more complex and will be difficult to achieve using any conventional method. Since the application of the temperature sensor will be to measure temperature inside combustion chambers or furnaces it was decided to build a curved sample that will fit inside a cylindrical combustion chamber or a tube furnace. For demonstration, a MTI OTF – 1200X tube furnace, with 44.62 mm inside diameter was chosen and the fabricated samples had to fit inside the tube. Two different samples with different arc lengths and thicknesses were made. The first sample has a short arc length of 4.38 mm with 4 mm thickness and the second sample has larger arc length of 20 mm and thickness of 2.5 mm. CAD designs of the two samples are shown in Figure 4.26 and the fabricated parts are shown in Figure 4.27. From

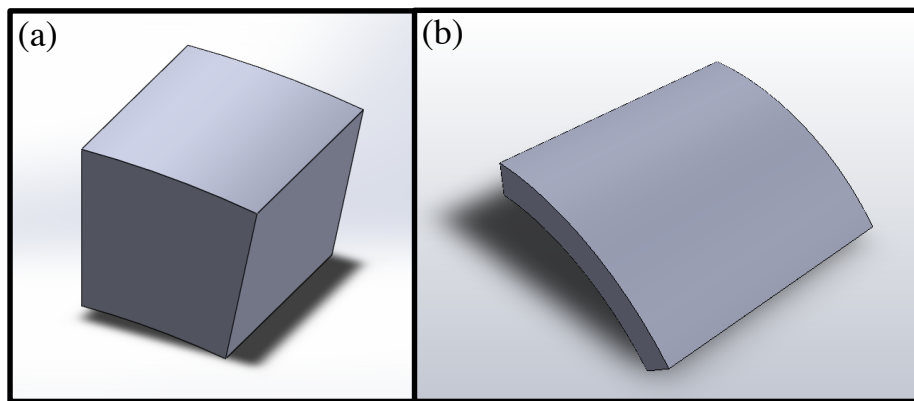


Figure 4.26: CAD design of curved sample of (a) 4.38 mm arc length and 4mm thickness (b) 20 mm arc length and 2.5 mm thickness

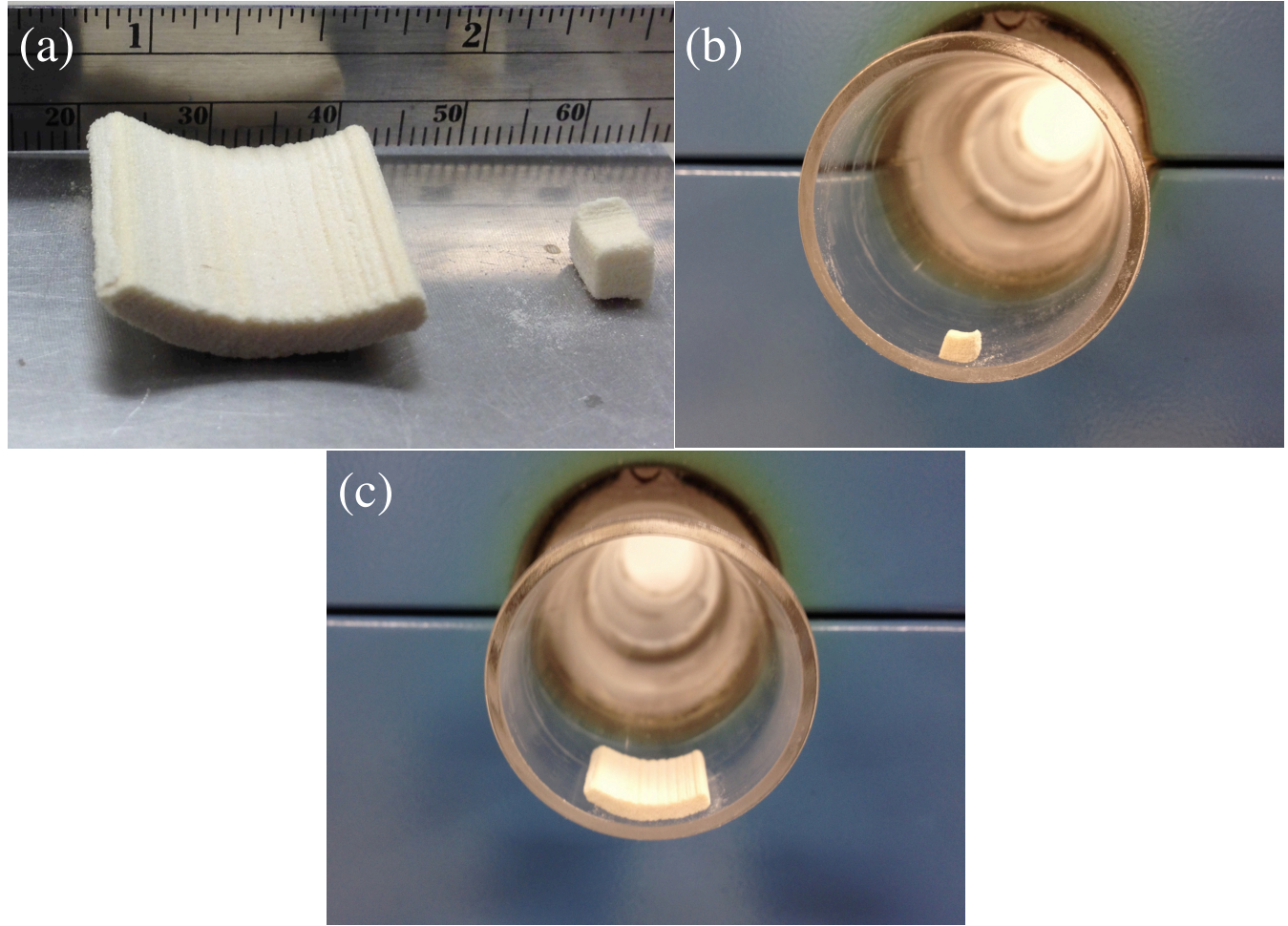


Figure 4.27: Fabricated curved samples (a) as built samples (b) small sample fitted inside the tube (c) large sample inside the tube

Figure 4.27, it can be seen that the curved samples made with alumina achieved good dimensional accuracy and fitted nicely inside the tube furnace.

4.3 Conclusion

In this chapter, the feasibility of using additive manufacturing to fabricate ceramic parts for the proposed sensor model was discussed. Initially BTO powders were used and different parameters such as different binder saturations, layer thickness and sintering profile was evaluated to obtain the optimum settings for the fabrication. Unfortunately, the particle size for BTO powders was too small to have good parts using the ExOne M-lab system and hence obtaining complicated geometry was not possible and the fabricated samples cracked either

before sintering or after sintering. Then, a new material alumina with proper particle size was used and complex male and female parts as well as curved samples were fabricated successfully and sintering profile with maximum temperature of 1650 °C for 4 hours was used to sinter these alumina samples. Future work will include finding the optimum sintering profile for alumina samples as well as doping the particles with BTO to obtain better dielectric properties, and designing and fabricating male, female parts as well as curved parts to hold two CRR structures in the assembly.

Chapter 5: Testing and Results

In this chapter, experimental setup for measuring the dielectric constant of the different materials used and fabricated both by conventional method, and 3D fabrication will be described and the test results will be presented. Agiles PNA-XX network analyzer and Ku band waveguide were used to conduct the testing to measure the dielectric constant of BTO and alumina samples. Later, a free space testing setup was used using two horn antennas and sensor samples made by compression method were tested and their transmission spectra $S_{2,1}$ was plotted against a sweep frequency from 8.2 to 12 GHz and the resonance response is analyzed. More tests were conducted using the facility of MWI lab in Phoenix, Arizona and the results will be presented and discussed as well.

5.1 Experimental setup using waveguide and network analyzer and corresponding test results

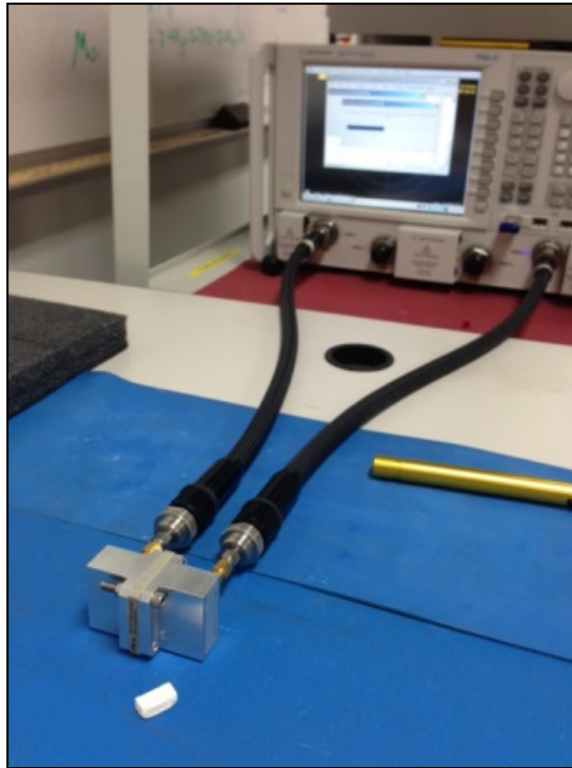


Figure 5.1: Experimental setup of measuring dielectric constant with a waveguide, a 3D printed BTO sample is placed in front of the setup

Figure 5.1 shows the experimental setup used for obtaining the dielectric constant of BTO samples fabricated by both compression method and 3D printing. An Agilent PNA-XX network analyzer was used to analyze the data. Two ports of the network analyzer were attached to the two ports of the waveguide and the sample was placed inside the waveguide and secured properly. Open, short and loaded calibrations were done each time before placing a sample inside of the waveguide.

Dielectric constant of the 3D printed samples were tested using a WR 62 – Ku band waveguide that has a frequency range from 12.4 – 18 GHz. Samples sintered using different sintering profiles were tested and the dielectric constant value as a function of frequency was plotted in Figure 5.2. It is observed that the dielectric constant decreases with the increase of frequency and samples sintered at 1260 °C showed the highest dielectric constant for any given frequency. It was expected as these samples showed the highest compactness and best grain growth (as discussed in chapter 4) among these three samples.

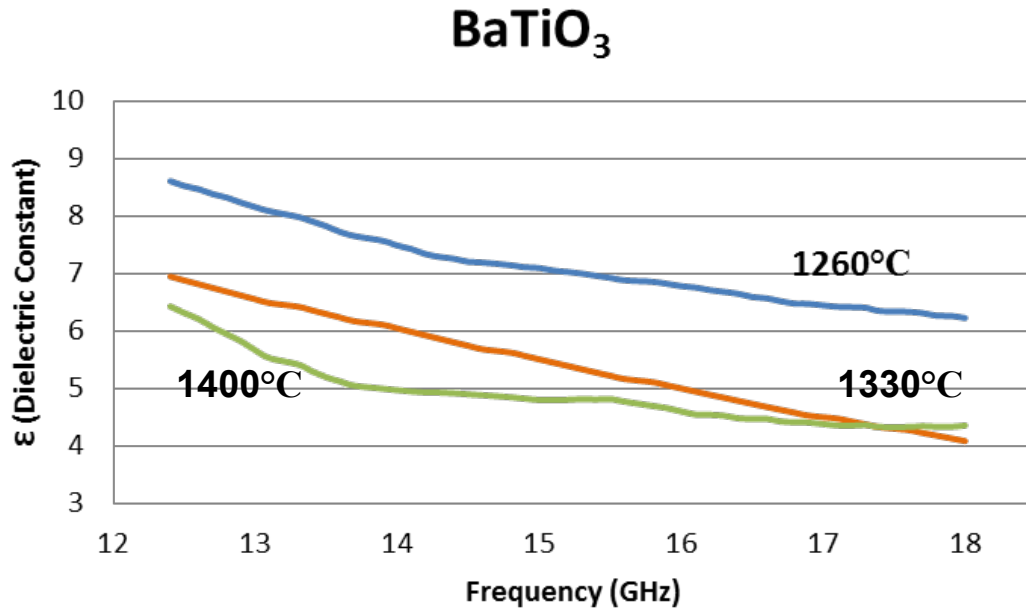


Figure 5.2: Dielectric constant of BTO samples fabricated by 3D printing and sintered at different temperatures as a function of frequency

Dielectric constant of an as built sample fabricated by compression method was tested using a WR 90 – X band waveguide with the frequency ranging 8.2 - 12.4 GHz. Due to the size constraint of

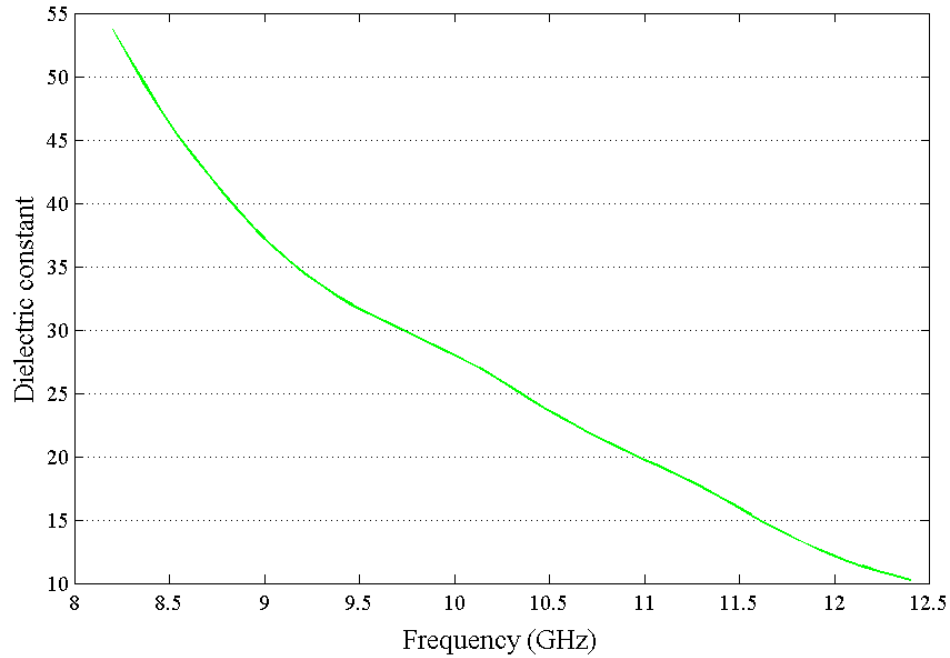


Figure 5.3: Dielectric constant of an as built sample fabricated by compression method as a function of frequency

fabricating samples with compression method, it was not possible to build a sample to fit the Ku band waveguide. Similar to the 3D printed samples, the compressed sample also show a decrease with the increase of frequency and the dielectric constant measured at 12.4 GHz is almost 10 which is close to the dielectric constant value of the 3D printed sample sintered at 1260 °C.

5.2 Experimental setup for free space measurement using horn antenna and corresponding test results

Once the characterizations of the materials were done, the next step was to test the fabricated samples in free space and locate the resonance frequency. A pair of horn antenna and the same PNA network analyzer was used for this purpose. The experimental setup is shown in

Figure 5.4. Two horn antennas were set at a distance and were connected to the two ports of the network analyzer. The test sample was placed near the transmitting antenna and two Styrofoam blocks were used to support the sample. The signal was sent from the transmitting antenna and was received by the other antenna. The network analyzer was used to analyze the transmitted data from the transmitter antenna to the receiver antenna.

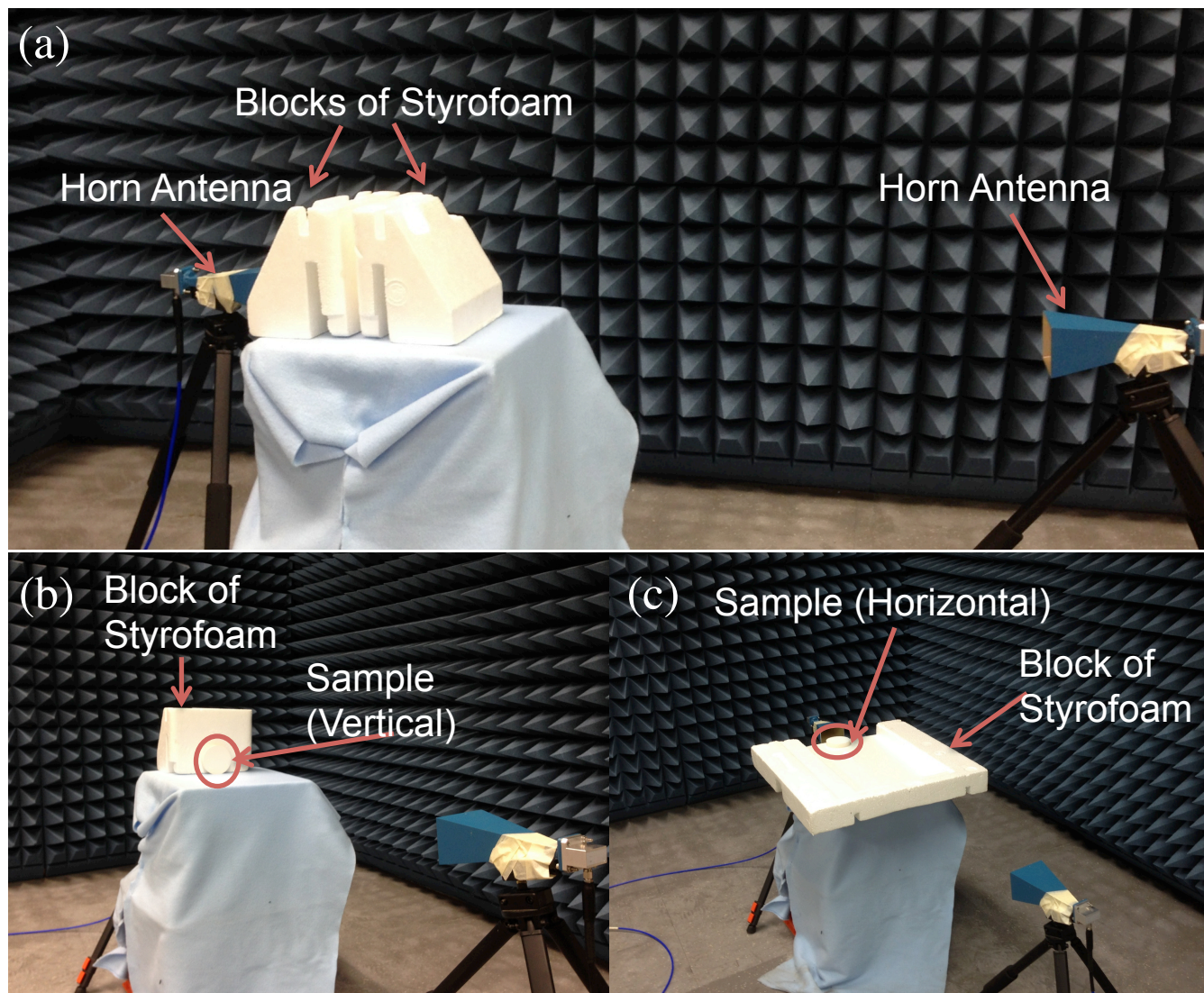


Figure 5.4: Free space measurement setup using horn antenna connected to a network analyzer

Three samples (sample 3, 4 and 5) were tested using this setup and the transmission response of those samples in vertical and horizontal orientations are analyzed. Figure 5.5 and 5.6

represents a comparison of the transmission response of the three samples for horizontal and vertical orientation respectively. For the horizontal orientation, no identifiable resonance peak was observed. As the sample thickness was not large enough to have the antenna in the shadow of the samples, the surrounding noises interfered and the data received by the antenna does not necessarily represent the transmission response of the sample.

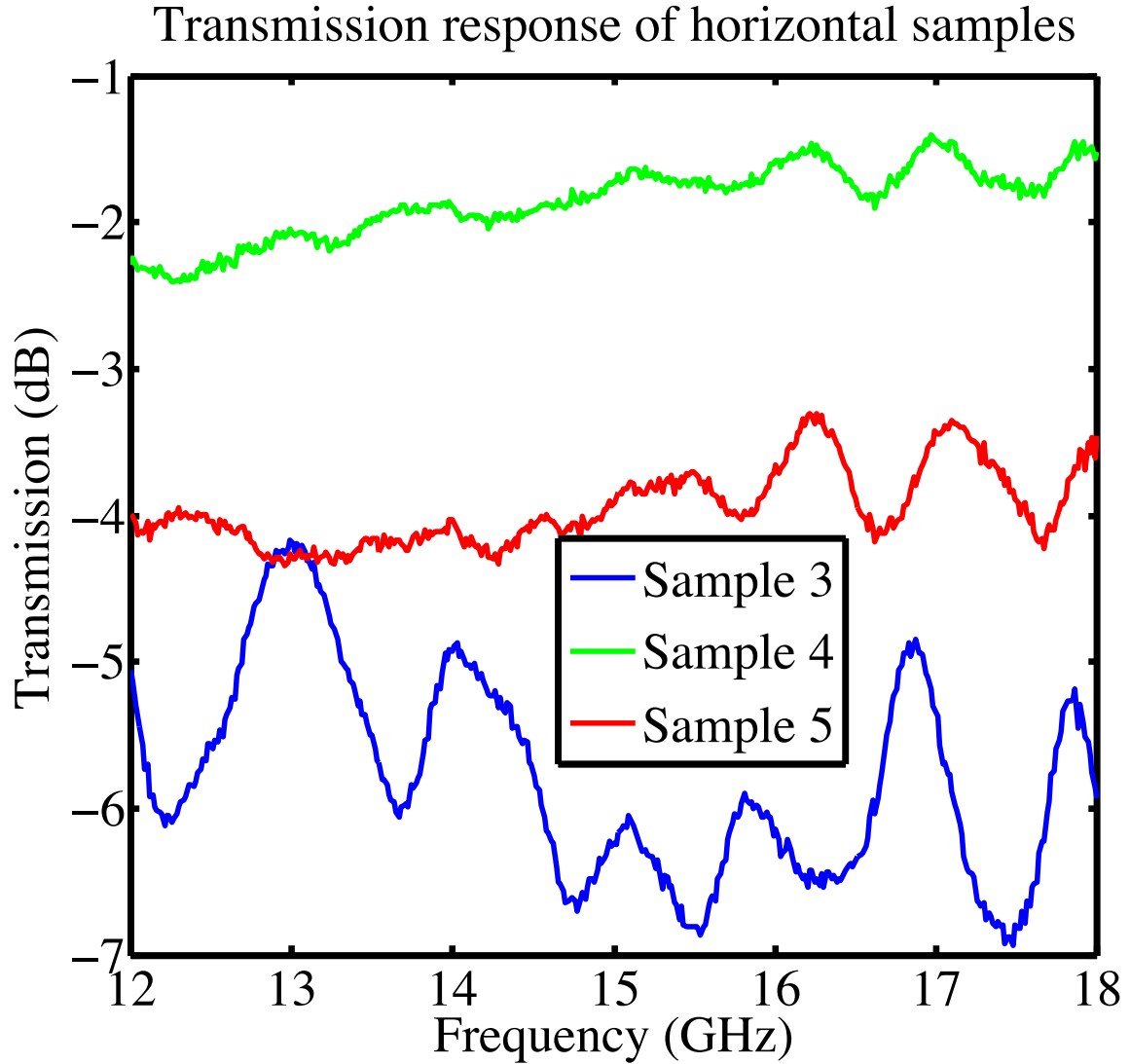


Figure 5.5: Transmission response measured from the scattered parameters for sample 3, 4, and 5 placed horizontally

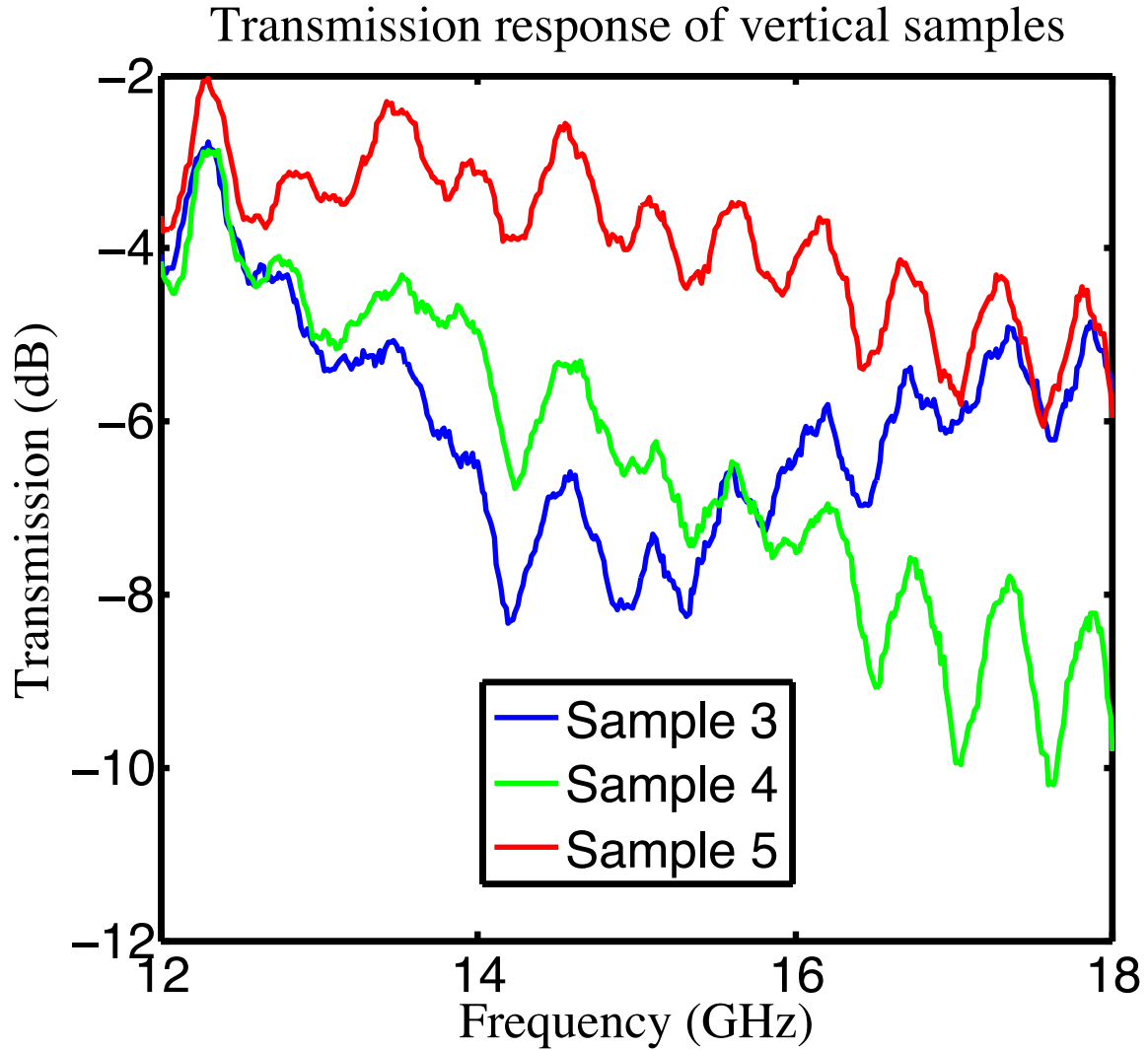


Figure 5.6: Transmission response measured from the scattered parameters for sample 3, 4, and 5 placed vertically

In the vertical orientation, sample 5 did not show any defined resonance peak while sample 3 and 4 displayed the first resonance peak near 14 GHz. However, the presence of multiple peaks makes it difficult to trace the desired peak. The presence of multi-peaks can be associated with either multiple resonances of the structure or from the surrounding noise and needs further investigation.

5.3 Experimental setup for free space measurement using Gaussian Beam antenna and corresponding test results

Since, using horn antenna in free space did not provide any decisive result, a better test

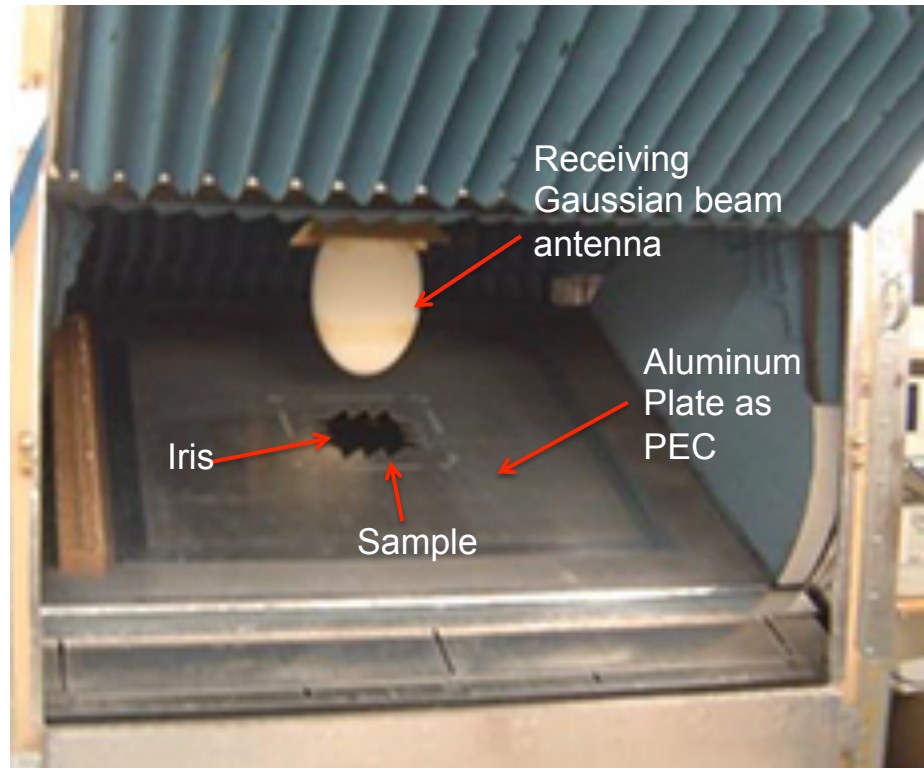


Figure 5. 7: Free space testing setup with two Gaussian Beam antennas connected with a network analyzer (www.mwilab.com)

setup was needed to obtain better results with reduced noise. MWI lab, a company based in Phoenix, Arizona was kind enough to let us use their test facility equipped with two Mr. Bean Gaussian beam antennas as shown in Figure 5.7. There are two chambers in the setup. The lower chamber is an isolated box with walls lined with aluminum plate. A Mr. Bean Gaussian beam antenna is placed inside the lower chamber. On the top surface of the chamber, an aluminum plate is placed as a PEC (Perfect Electric Conductor) with an opening in the middle called iris. The top and bottom antenna, and iris are all aligned and the sample is placed on the iris so that the sample perfectly covers the iris. The antennas are connected to the two ports of a network analyzer. The bottom antenna sends the signal and the top antenna receives it. Since, the sample

is placed on the iris and since it covers the iris and the surroundings are covered with aluminum, the signal that the top antenna receives comes through the sample and hence less noise is observed in the data (Figure 5.8 to 5.15).

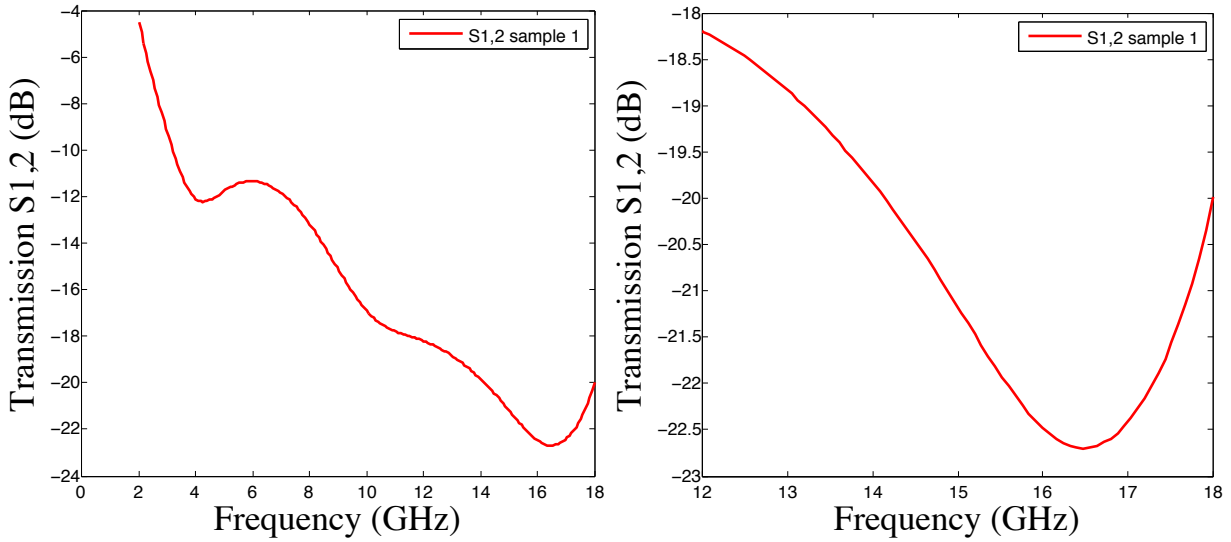


Figure 5.8: Transmission response from sample 1 (a) from 2-18 GHz (b) from 12-18 GHz

The transmission response from sample 1 is plotted in Figure 5.8. It shows something similar to a resonance at around 16.5 GHz, which is magnified in Figure 5.8 (b). However, as the tests were limited to 18 GHz, it cannot be decided whether there was a resonance or not. Similar results were obtained from sample 3 and 6 shown in Figure 5.10 and 5.13 respectively where it cannot be decided whether there is a resonance or not and needs to be tested at higher frequency. Transmission response from sample 4, 5, 7 and 8 did not show any resonance within this frequency range (Figure 5.11, 5.12, 5.14 and 5.15 respectively). Further investigations at higher and lower frequencies are needed to obtain the resonance characteristics of this sample. Sample 2, on the other hand, showed excellent resonance characteristics within this frequency range as shown in Figure 5.9. The first resonance is at around 5 GHz and there are two more resonance peaks observed at around 9 GHz and 13 GHz. The peak at 9 GHz shows the highest intensity and can be used as the reference resonance frequency for sensing.

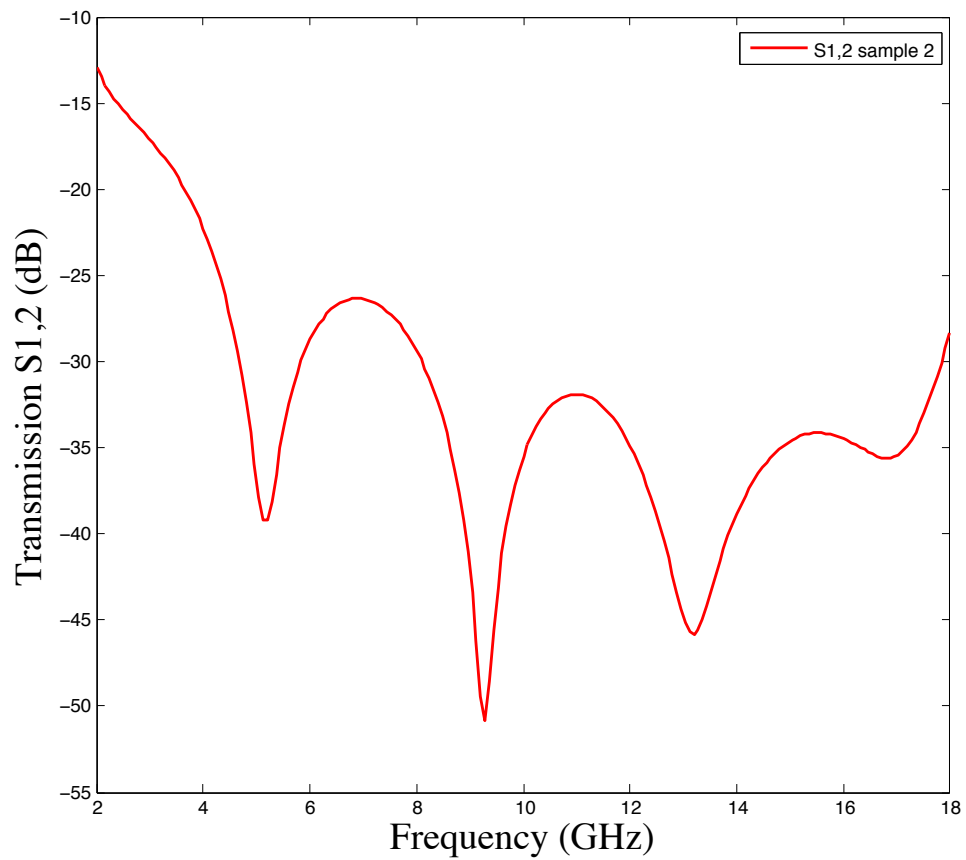


Figure 5.9: Transmission response from sample 2

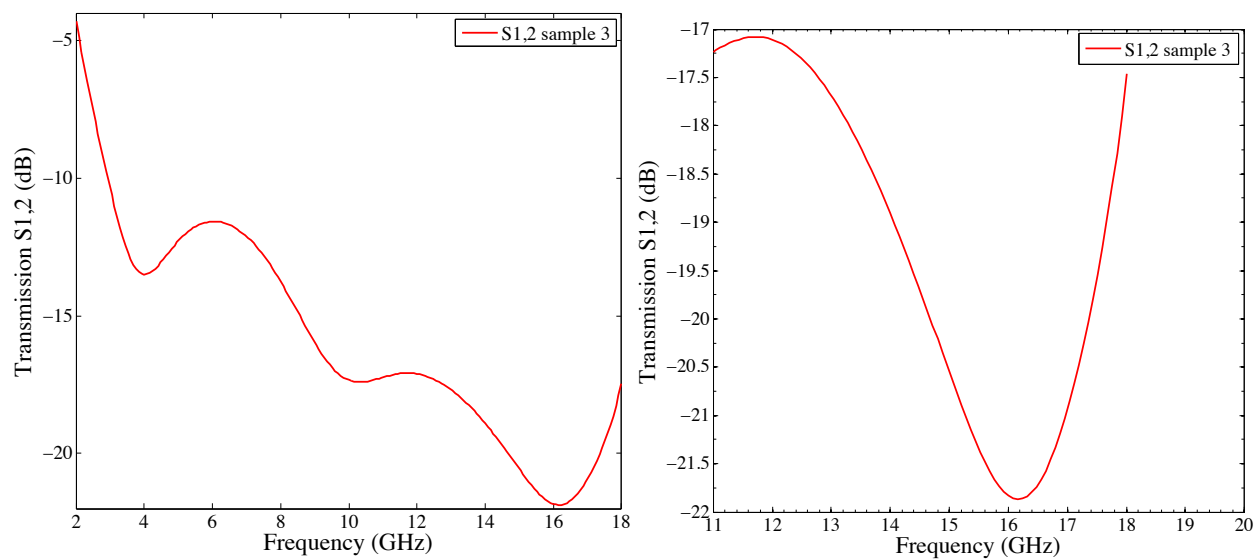


Figure 5.10: Transmission response from sample 3 (a) from 2-18 GHz (b) from 11-18 GHz

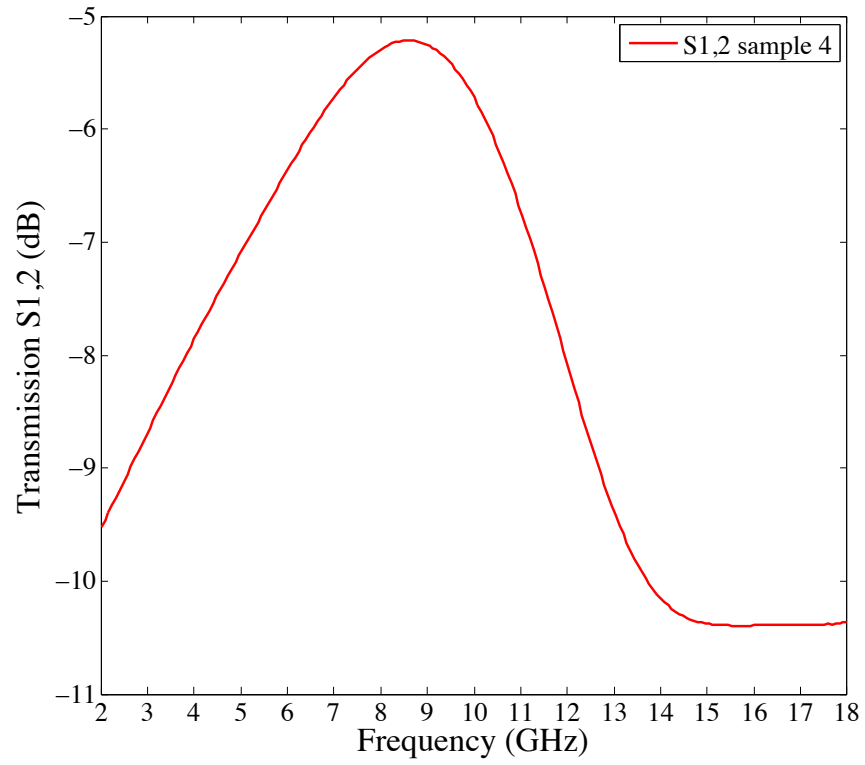


Figure 5.11: Transmission response from sample 4

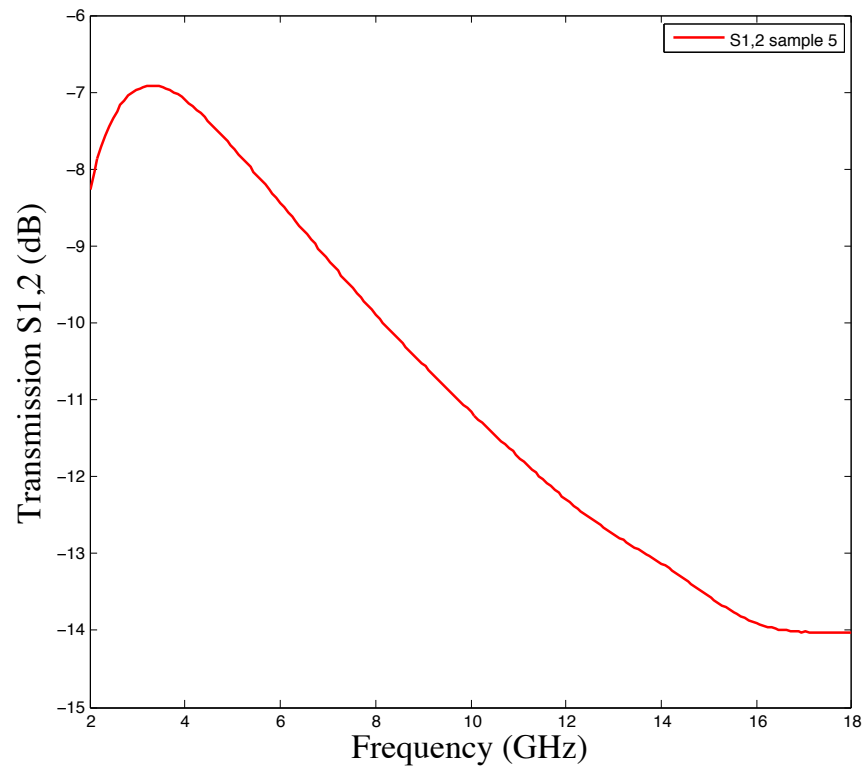


Figure 5.12: Transmission response from sample 5

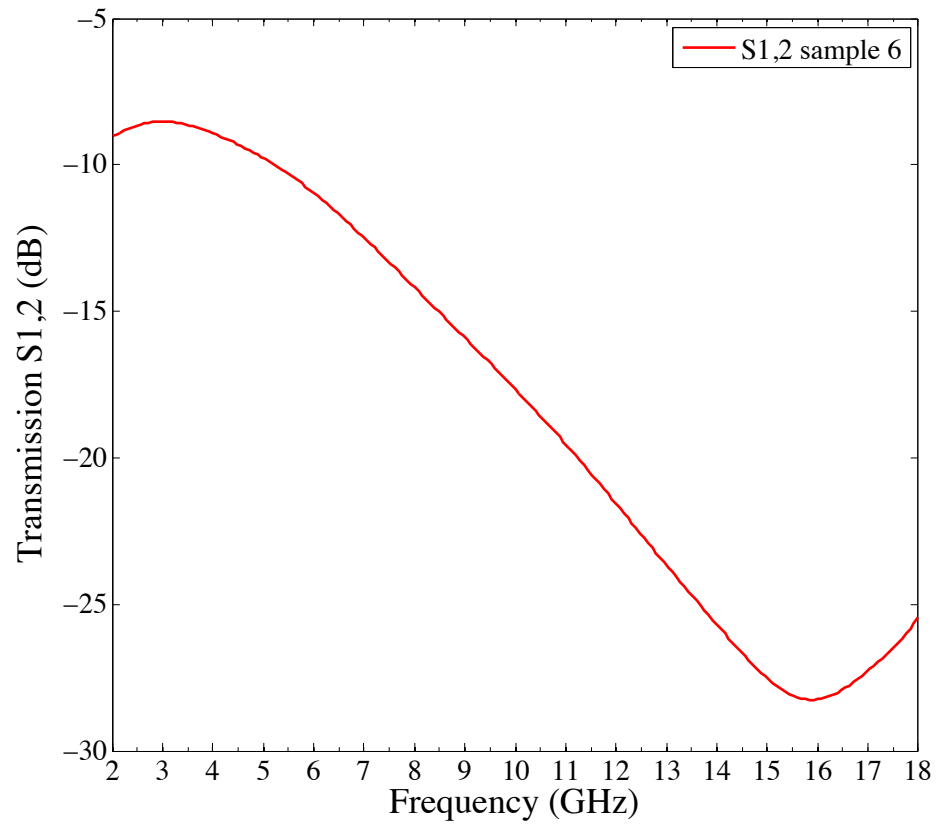


Figure 5.13: Transmission response from sample 6

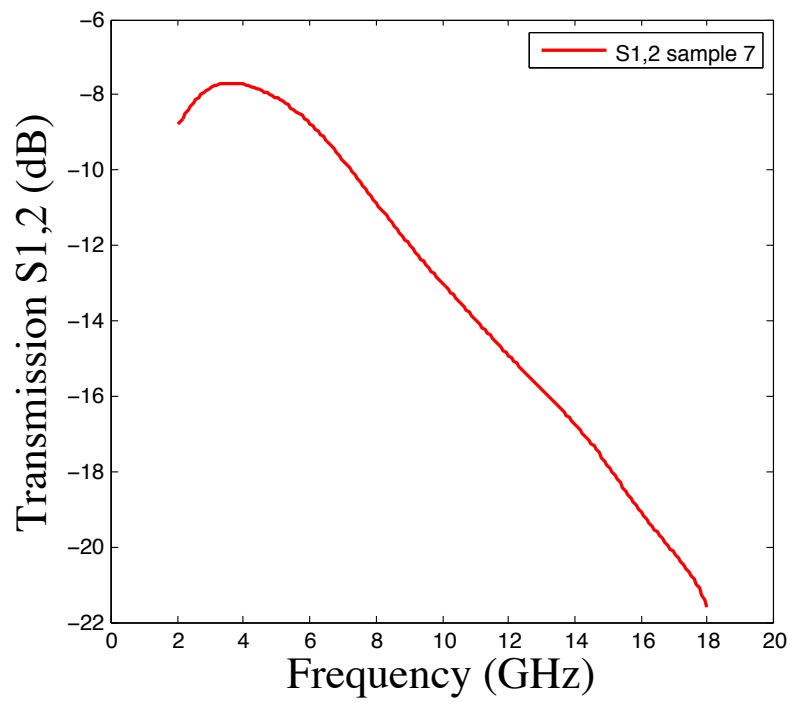


Figure 5.14: Transmission response from sample 7

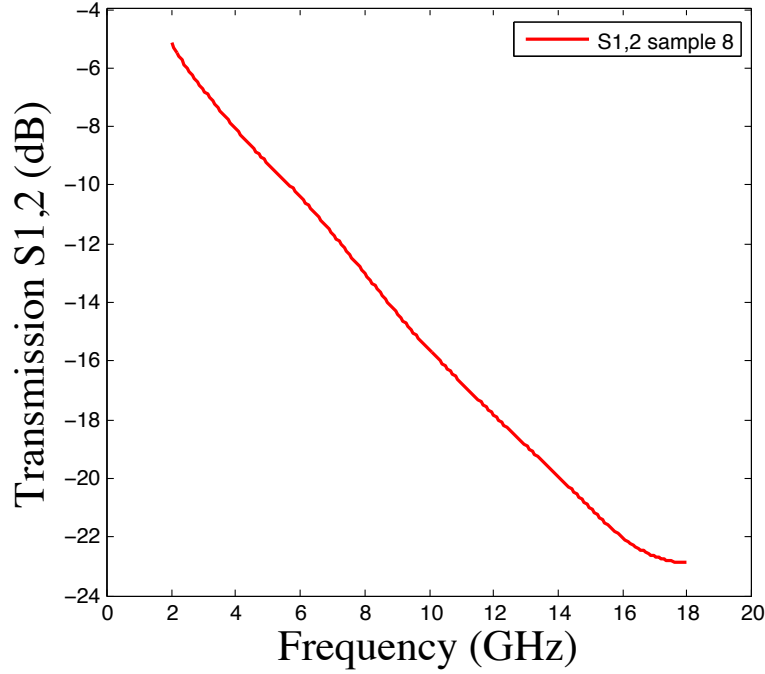


Figure 5.15: Transmission response from sample 8

5.4 Conclusion

In this chapter, preliminary test results at room temperature have been discussed. Two different test setups have been used, one with two horn antennas and one with two Gaussian beam antennas. The results obtained using the first setup was affected by the surrounding noise, while the results obtained using the Gaussian beam antennas had less noise. Sample 3, 4 and 5 were tested for a sweep frequency from 12-18 GHz using the horn antennas and all of the 8 samples were tested for a sweep frequency from 2-18 GHz using Gaussian beam antennas. Sample 2 and sample 3 showed excellent resonant behavior within this frequency window while other samples did not show anything decisive. Further investigation will be carried out at higher frequencies and also as a function of temperature to demonstrate the temperature sensitivity of the samples.

Chapter 6: Conclusion

Wireless temperature sensing is of utmost importance to the energy conversion systems where one percent of accuracy improvement can result hundreds of millions of cost savings. In this thesis, we propose a metamaterial-based wireless temperature sensor consisting of two CRR structures embedded in a dielectric matrix for high temperature and harsh environment operations. The proposed sensor model shows a linear change in its resonance frequency with the change in temperature, which is detected by antennas and analyzed by a network analyzer. The use of CRR structure makes the fabrication cheap and simple as complex technique like lithography can be avoided.

In chapter 3, full-wave electromagnetic simulations using HFSS demonstrate the feasibility of such a sensor and models using other common SRR structures were also evaluated and compared with the proposed CRR structure. Effect of geometrical parameters such as substrate thickness and split gap were evaluated and it was seen that with the increase of substrate thickness all other structures shows an increase in the resonance frequency while CRR structure shows a decrease. The increase of split gap is also found to be increasing the resonance frequency for all the structures that were evaluated. A comparative analysis of the sensitivity of each structure was examined using the dielectric constant of LiNbO_3 at different temperatures. It was demonstrated that proposed CRR structure is highly sensitive to the change of temperature and hence really suitable as a temperature sensor.

In chapter 4, two different fabrication techniques were discussed; one was conventional die-punch compressing method and the other is 3D printing using binder-jetting technology. SEM and XRD characterized the materials used for both fabrication techniques. It was found that while small particle size of the BTO powders used yielded good results in the conventional method, it was not suitable for the M-lab system for 3D printing. It was found out that using the conventional method it's possible to achieve good strength and density of the samples while the 3D printed samples needed curing and sintering to achieve better strength as well as higher

density. However, the conventional method was limited only in obtaining circular or square shaped sample, complex geometries such as a curved part was fabricated using the 3D printing technology.

In chapter 5, some preliminary testing results of samples fabricated using conventional method were presented. Two different test setup was used; one with a pair of horn antennas and the other with a pair of Gaussian beam antennas and less noise observed in the results obtained using the Gaussian beam antennas. While some samples showed good results, other samples did not show good resonance peaks within the frequency range used for testing.

Future work will include investigating different sintering profiles for alumina and obtaining the optimum profile to achieve the highest density and fabricating array of samples of the same dimensions and CRR arrangement by 3D printing. Further investigation will be carried out at higher frequencies and also as a function of temperature inside a combustion chamber to demonstrate the temperature sensitivity of the samples.

References

1. Goetz, J., *Sensors That Can Take the Heat, Part 1: Opening the High-Temperature Toolbox*. Sensors, 2000. **17**(6): p. 20-39.
2. Gregory, O.J. and T. You, *Ceramic temperature sensors for harsh environments*. Sensors Journal, IEEE, 2005. **5**(5): p. 833-838.
3. Thai, T.T., et al. *A novel passive wireless ultrasensitive RF temperature transducer for remote sensing*. in *Microwave Symposium Digest (MTT), 2010 IEEE MTT-S International*. 2010. IEEE.
4. Smith, D., J. Pendry, and M. Wiltshire, *Metamaterials and negative refractive index*. Science, 2004. **305**(5685): p. 788-792.
5. Veselago, V.G., *The electrodynamics of substances with simultaneously negative values of ϵ and μ* . Physics-Uspekhi, 1968. **10**(4): p. 509-514.
6. Katsarakis, N., et al., *Electric coupling to the magnetic resonance of split ring resonators*. Applied physics letters, 2004. **84**(15): p. 2943-2945.
7. Katsarakis, N., et al., *Magnetic response of split-ring resonators in the far-infrared frequency regime*. Optics Letters, 2005. **30**(11): p. 1348-1350.
8. Ekmekci, E., R. Averitt, and G. Turhan-Sayan. *Effects of Substrate Parameters on the Resonance Frequency of Double-sided SRR Structures under Two Different Excitations*. in *Symposium Proceedings of the Progress in Electromagnetic Research*. 2010.
9. Ekmekci, E., *Design, fabrication and characterization of novel metamaterials in microwave and terahertz regions: multi-band, frequency-tunable and miniaturized structures*, in *Electrical and Electronics Engineering 2010*, Middle East Technical University.
10. Pendry, J.B., et al., *Magnetism from conductors and enhanced nonlinear phenomena*. Microwave Theory and Techniques, IEEE Transactions on, 1999. **47**(11): p. 2075-2084.
11. Shakoor, A., *Design Fabrication and Characterization of Split Ring Resonators in the Near Infrared Region*.
12. Aydin, K., et al., *Investigation of magnetic resonances for different split-ring resonator parameters and designs*. New journal of physics, 2005. **7**(1): p. 168.
13. Zhang, S., J. Xiao, and Y. Li, *Novel microstrip band-stop filters based on complementary split ring resonators*. Microwave Journal, 2006. **49**(11): p. 100.
14. Chen, H.-T., et al., *Active terahertz metamaterial devices*. Nature, 2006. **444**(7119): p. 597-600.
15. Chen, H.-T., et al., *A metamaterial solid-state terahertz phase modulator*. Nature photonics, 2009. **3**(3): p. 148-151.
16. Grimberg, R., *Electromagnetic metamaterials*. Materials Science and Engineering: B, 2013.

17. Freire, M.J., R. Marques, and L. Jelinek, *Experimental demonstration of a $\mu = -1$ metamaterial lens for magnetic resonance imaging*. Applied physics letters, 2008. **93**: p. 231108.
18. Pendry, J.B., *Negative refraction makes a perfect lens*. Physical review letters, 2000. **85**(18): p. 3966.
19. Wood, B., *Metamaterials and invisibility*. Comptes Rendus Physique, 2009. **10**(5): p. 379-390.
20. Pendry, J.B., D. Schurig, and D.R. Smith, *Controlling electromagnetic fields*. Science, 2006. **312**(5781): p. 1780-1782.
21. Schurig, D., et al., *Metamaterial electromagnetic cloak at microwave frequencies*. Science, 2006. **314**(5801): p. 977-980.
22. Chen, H. and C. Chan, *Acoustic cloaking in three dimensions using acoustic metamaterials*. Applied physics letters, 2007. **91**(18): p. 183518-183518-3.
23. Lai, Y., et al., *Hybrid elastic solids*. Nature materials, 2011. **10**(8): p. 620-624.
24. Torres-Silva, H. and D.T. Cabezas, *Chiral Seismic Attenuation with Acoustic Metamaterials*. Journal of Electromagnetics Analysis and Applications, 2013. **5**(1): p. 10-15.
25. Chen, T., S. Li, and H. Sun, *Metamaterials application in sensing*. Sensors, 2012. **12**(3): p. 2742-2765.
26. Lee, H.-J. and J.-G. Yook, *Biosensing using split-ring resonators at microwave regime*. Applied physics letters, 2008. **92**(25): p. 254103-254103-3.
27. Tao, H., et al., *Metamaterials on paper as a sensing platform*. Advanced Materials, 2011. **23**(28): p. 3197-3201.
28. Kabashin, A., et al., *Plasmonic nanorod metamaterials for biosensing*. Nature materials, 2009. **8**(11): p. 867-871.
29. Yoshida, H., et al., *Terahertz sensing method for protein detection using a thin metallic mesh*. Applied physics letters, 2007. **91**(25): p. 253901-253901-3.
30. Melik, R., et al., *Flexible metamaterials for wireless strain sensing*. Applied physics letters, 2009. **95**(18): p. 181105-181105-3.
31. Ekmekci, E. and G. Turhan-Sayan. *Metamaterial sensor applications based on broadside-coupled SRR and V-Shaped resonator structures*. in *Antennas and Propagation (APSURSI), 2011 IEEE International Symposium on*. 2011. IEEE.
32. Kadic, M., et al., *Metamaterials beyond electromagnetism*. Reports on progress in physics. Physical Society (Great Britain), 2013. **76**(12): p. 126501-126501.
33. Engheta, N. *Metamaterials with negative permittivity and permeability: background, salient features, and new trends*. in *Microwave Symposium Digest, 2003 IEEE MTT-S International*. 2003. IEEE.
34. Bose, J.C., *On the rotation of plane of polarisation of electric waves by a twisted structure*. Proceedings of the Royal Society of London, 1898. **63**(389-400): p. 146-152.

35. Lindman, K.F., *Über eine durch ein isotropes System von spiralförmigen Resonatoren erzeugte Rotationspolarisation der elektromagnetischen Wellen*. Annalen der Physik, 1920. **368**(23): p. 621-644.
36. Kock, W.E., *Metallic delay lenses*. Bell Syst. Tech. J., 1948. **27**: p. 58-82.
37. Veselago, V., *Properties of materials having simultaneously negative values of the dielectric (ϵ) and the magnetic (μ) susceptibilities*. Soviet Physics-Solid State, 1967. **8**(12).
38. Pendry, J., et al., *Extremely low frequency plasmons in metallic mesostructures*. Physical review letters, 1996. **76**(25): p. 4773.
39. Smith, D.R., et al., *Composite medium with simultaneously negative permeability and permittivity*. Physical review letters, 2000. **84**(18): p. 4184.
40. Shelby, R.A., D.R. Smith, and S. Schultz, *Experimental verification of a negative index of refraction*. Science, 2001. **292**(5514): p. 77-79.
41. Grzegorzcyk, T. and J. Kong, *Review of left-handed metamaterials: Evolution from theoretical and numerical studies to potential applications*. Journal of Electromagnetic Waves and Applications, 2006. **20**(14): p. 2053-2064.
42. O'Äöbrien, S. and J. Pendry, *Magnetic activity at infrared frequencies in structured metallic photonic crystals*. Journal of Physics: Condensed Matter, 2002. **14**(25): p. 6383.
43. Grzegorzcyk, T.M., et al., *Properties of left-handed metamaterials: transmission, backward phase, negative refraction, and focusing*. Microwave Theory and Techniques, IEEE Transactions on, 2005. **53**(9): p. 2956-2967.
44. Marques, R., F. Medina, and R. Rafii-El-Idrissi, *Role of bianisotropy in negative permeability and left-handed metamaterials*. Physical Review B, 2002. **65**(14): p. 144440.
45. Saadoun, M.M. and N. Engheta, *A reciprocal phase shifter using novel pseudochiral or $\mathcal{C}\mathcal{E}$ medium*. Microwave and Optical Technology Letters, 1992. **5**(4): p. 184-188.
46. Huangfu, J., et al., *Experimental confirmation of negative refractive index of a metamaterial composed of Ω -like metallic patterns*. Applied physics letters, 2004. **84**(9): p. 1537-1539.
47. Chen, H., et al., *Negative refraction of a combined double S-shaped metamaterial*. Applied physics letters, 2005. **86**(15): p. 151909-151909-3.
48. Chen, H., et al., *Magnetic properties of S-shaped split-ring resonators*. Progress In Electromagnetics Research, 2005. **51**: p. 231-247.
49. Gay-Balmaz, P. and O.J. Martin, *Efficient isotropic magnetic resonators*. Applied physics letters, 2002. **81**(5): p. 939-941.
50. Yao, H.-Y., et al., *Macroscopic performance analysis of metamaterials synthesized from microscopic 2-D isotropic cross split-ring resonator array*. Progress In Electromagnetics Research, 2005. **51**: p. 197-217.

51. Wongkasem, N., A. Akyurtlu, and K.A. Marx, *Group theory based design of isotropic negative refractive index metamaterials*. Progress In Electromagnetics Research, 2006. **63**: p. 295-310.
52. Vendik, I. and O. Vendik, *Metamaterials and their application in microwaves: A review*. Technical Physics, 2013. **58**(1): p. 1-24.
53. Vendik, O. and M. Gashinova, *Proceedings of the 34th European Microwave Conference, Amsterdam, The Netherlands, 2004*. 2004.
54. Chen, H., et al., *Equivalent circuit model for left-handed metamaterials*. Journal of applied physics, 2006. **100**(2): p. 024915-024915-6.
55. Moss, C., T. Grzegorzczuk, and Y. Zhang, *Numerical studies of left handed metamaterials*. Progress In Electromagnetics Research, 2002. **35**: p. 315-334.
56. Lindell, I.V., et al., *Electromagnetic waves in chiral and bi-isotropic media*. 1994.
57. Wang, B., et al., *Chiral metamaterials: simulations and experiments*. Journal of Optics A: Pure and Applied Optics, 2009. **11**(11): p. 114003.
58. Barron, L.D., *Molecular light scattering and optical activity* 2004: Cambridge University Press.
59. Tretyakov, S., et al., *Waves and energy in chiral nihility*. Journal of Electromagnetic Waves and Applications, 2003. **17**(5): p. 695-706.
60. Pendry, J., *A chiral route to negative refraction*. Science, 2004. **306**(5700): p. 1353-1355.
61. Marques, R., L. Jelinek, and F. Mesa, *Negative refraction from balanced quasi-Åplanar chiral inclusions*. Microwave and Optical Technology Letters, 2007. **49**(10): p. 2606-2609.
62. Baena, J., L. Jelinek, and R. Marqués, *Towards a systematic design of isotropic bulk magnetic metamaterials using the cubic point groups of symmetry*. Physical Review B, 2007. **76**(24): p. 245115.
63. Jelinek, L., et al., *Periodic arrangements of chiral scatterers providing negative refractive index bi-isotropic media*. Physical Review B, 2008. **77**(20): p. 205110.
64. Frank, B., et al., *Large-Area 3D Chiral Plasmonic Structures*. ACS nano, 2013. **7**(7): p. 6321-6329.
65. Tang, Y., *Chirality of Light and Its Interaction with Chiral Matter*. 2013.
66. Han, C., H.M. Leung, and W.Y. Tam, *Chiral metamaterials by shadowing vapor deposition*. Journal of Optics, 2013. **15**(7): p. 072101.
67. Papakostas, A., et al., *Optical manifestations of planar chirality*. Physical review letters, 2003. **90**(10): p. 107404.
68. Rogacheva, A., et al., *Giant gyrotropy due to electromagnetic-field coupling in a bilayered chiral structure*. Physical review letters, 2006. **97**(17): p. 177401.
69. Zhang, S., et al., *Negative refractive index in chiral metamaterials*. Physical review letters, 2009. **102**(2): p. 023901.

70. Murugkar, S., et al. *Planar chiral metamaterials for biosensing applications*. in *SPIE BiOS*. 2013. International Society for Optics and Photonics.
71. Novitsky, A.V., V.M. Galynsky, and S.V. Zhukovsky, *Asymmetric transmission in planar chiral split-ring metamaterials: Microscopic Lorentz-theory approach*. *Physical Review B*, 2012. **86**(7): p. 075138.
72. Mahmoud, S.F. and A.J. Viitanen, *Surface wave character on a slab of metamaterial with negative permittivity and permeability*. *Progress In Electromagnetics Research*, 2005. **51**: p. 127-137.
73. Enoch, S., et al., *A metamaterial for directive emission*. *Physical review letters*, 2002. **89**(21): p. 213902.
74. Hamid, A.-K., *Axially slotted antenna on a circular or elliptic cylinder coated with metamaterials*. *Progress In Electromagnetics Research*, 2005. **51**: p. 329-341.
75. Engheta, N., *An idea for thin subwavelength cavity resonators using metamaterials with negative permittivity and permeability*. *Antennas and Wireless Propagation Letters*, IEEE, 2002. **1**(1): p. 10-13.
76. Shi, Y. and C.-H. Liang, *Analysis of the left-handed metamaterials using multi-domain pseudospectral time-domain algorithm*. *Progress In Electromagnetics Research*, 2005. **51**: p. 153-165.
77. Shooshtari, A. and A.R. Sebak, *Electromagnetic scattering by parallel metamaterial cylinders*. *Progress In Electromagnetics Research*, 2006. **57**: p. 165-177.
78. Yang, F., et al., *DC electric invisibility cloak*. *Physical review letters*, 2012. **109**(5): p. 053902.
79. Fan, C., Y. Gao, and J. Huang, *Shaped graded materials with an apparent negative thermal conductivity*. *Applied physics letters*, 2008. **92**(25): p. 251907-251907-3.
80. Li, J., Y. Gao, and J. Huang, *A bifunctional cloak using transformation media*. *Journal of applied physics*, 2010. **108**(7): p. 074504-074504-5.
81. Chen, T., C.-N. Weng, and J.-S. Chen, *Cloak for curvilinearly anisotropic media in conduction*. *Applied physics letters*, 2008. **93**(11): p. 114103-114103-3.
82. Guenneau, S., C. Amra, and D. Veynante, *Transformation thermodynamics: cloaking and concentrating heat flux*. *Optics Express*, 2012. **20**(7): p. 8207-8218.
83. Schittny, R., et al., *Experiments on transformation thermodynamics: Molding the flow of heat*. *Physical review letters*, 2013. **110**(19): p. 195901.
84. Liang, Z. and J. Li, *Extreme acoustic metamaterial by coiling up space*. *Physical review letters*, 2012. **108**(11): p. 114301.
85. Frenzel, T., et al., *Three-dimensional labyrinthine acoustic metamaterials*. *Applied physics letters*, 2013. **103**(6): p. 061907-061907-4.
86. Liu, Z., et al., *Locally resonant sonic materials*. *Science*, 2000. **289**(5485): p. 1734-1736.
87. Schaedler, T., et al., *Ultralight metallic microlattices*. *Science*, 2011. **334**(6058): p. 962-965.

88. Buckmann, T., et al., *Tailored 3D Mechanical Metamaterials Made by Dip,Äin Direct,ÄLaser,ÄWriting Optical Lithography*. Advanced Materials, 2012. **24**(20): p. 2710-2714.
89. Schimetta, G., et al. *Wireless pressure and temperature measurement using a SAW hybrid sensor*. in *Ultrasonics Symposium, 2000 IEEE*. 2000. IEEE.
90. Ballandras, S., et al. *Wireless temperature sensor using SAW resonators for immersed and biological applications*. in *Ultrasonics Symposium, 2002. Proceedings. 2002 IEEE*. 2002. IEEE.
91. Hornsteiner, J., E. Born, and E. Riha, *Langasite for high temperature surface acoustic wave applications*. physica status solidi (a), 1997. **163**(1): p. R3-R4.
92. Hornsteiner, J., et al. *Surface acoustic wave sensors for high-temperature applications*. in *Frequency Control Symposium, 1998. Proceedings of the 1998 IEEE International*. 1998. IEEE.
93. Bulst, W.-E., G. Fischerauer, and L. Reindl, *State of the art in wireless sensing with surface acoustic waves*. Industrial Electronics, IEEE Transactions on, 2001. **48**(2): p. 265-271.
94. Reindl, L., et al. *Wireless measurement of temperature using surface acoustic waves sensors*. in *Frequency control symposium and PDA exhibition jointly with the 17th European frequency and time forum, 2003. Proceedings of the 2003 IEEE international*. 2003. IEEE.
95. Wang, Y., et al., *A passive wireless temperature sensor for harsh environment applications*. Sensors, 2008. **8**(12): p. 7982-7995.
96. Ong, K.G., et al., *Design and application of a wireless, passive, resonant-circuit environmental monitoring sensor*. Sensors and Actuators A: Physical, 2001. **93**(1): p. 33-43.
97. Kocer, F., P.M. Walsh, and M.P. Flynn. *An RF powered, wireless temperature sensor in quarter micron CMOS*. in *Circuits and Systems, 2004. ISCAS'04. Proceedings of the 2004 International Symposium on*. 2004. IEEE.
98. Souri, K., Y. Chae, and K. Makinwa. *A CMOS temperature sensor with a voltage-calibrated inaccuracy of $\pm 0.15^{\circ}\text{C}$ (3σ) from -55 to 125°C* . in *Solid-State Circuits Conference Digest of Technical Papers (ISSCC), 2012 IEEE International*. 2012. IEEE.
99. Cheng, H., S. Ebadi, and X. Gong, *A Low-Profile Wireless Passive Temperature Sensor Using Resonator/Antenna Integration Up to 1000°C* . Antennas and Wireless Propagation Letters, IEEE, 2012. **11**: p. 369-372.
100. Ekmekci, E. and G. Turhan-Sayan, *Multi-functional metamaterial sensor based on a broad-side coupled SRR topology with a multi-layer substrate*. Applied Physics A, 2013. **110**(1): p. 189-197.
101. Gu, J., et al., *A close-ring pair terahertz metamaterial resonating at normal incidence*. Opt. Express, 2009. **17**(22): p. 20307-20312.

102. Wu, M., et al. *A compact equivalent circuit model for the SRR structure in metamaterials.* in *Microwave Conference Proceedings, 2005. APMC 2005. Asia-Pacific Conference Proceedings.* 2005. IEEE.
103. Zhu, J., et al., *Optimal design of miniaturized thin-film helical resonators.* Applied physics letters, 2008. **93**(23): p. 234105-234105-3.
104. Lanfredi, S. and A. Rodrigues, *Impedance spectroscopy study of the electrical conductivity and dielectric constant of polycrystalline LiNbO₃.* Journal of applied physics, 1999. **86**(4): p. 2215-2219.
105. Ekmekci, E. and G. Turhan-Sayan, *Comparative investigation of resonance characteristics and electrical size of the double-sided SRR, BC-SRR and conventional SRR type metamaterials for varying substrate parameters.* Progress In Electromagnetics Research B, 2009. **12**: p. 35-62.
106. Alici, K.B., et al., *Miniaturized negative permeability materials.* Applied physics letters, 2007. **91**(7): p. 071121-071121-3.
107. Kinoshita, K. and A. Yamaji, *Grain-size effects on dielectric properties in barium titanate ceramics.* Journal of applied physics, 1976. **47**(1): p. 371-373.
108. Gaytan, S.M., et al., *Analysis of ferroelectric ceramic fabricated by binder jetting technology.*
109. Moon, J., et al., *Fabrication of functionally graded reaction infiltrated SiC-Si composite by three-dimensional printing (3DPTM) process.* Materials Science and Engineering: A, 2001. **298**(1): p. 110-119.
110. Subramaniam, S., *In Situ High Temperature Environmental Scanning Electron Microscopic Investigations of Sintering Behavior in Barium Titanate*, 2006, University of Cincinnati.
111. Chen, J.-H., et al., *Domain switching of barium titanate ceramics induced by surface grinding.* Materials chemistry and physics, 2005. **91**(1): p. 67-72.
112. Gao, L.-J., et al., *Grain-controlled barium titanate ceramics prepared from high-gravity reactive precipitation process powder.* Materials chemistry and physics, 2004. **88**(1): p. 27-31.

Curriculum Vita

Hasanul Karim was born on 1st February 1989 in Noakhali, Bangladesh. He is the second child of Mr. Ali Karim and Mrs. Mosammat Begum Noorjahan. Mr. Karim completed Bachelor of Science in Mechanical Engineering in April 2010 from Khulna University of Engineering & Technology. After completion of Bachelor degree he joined the High Commission of Canada, Bangladesh and served as a facilities assistant. In August 2012 Mr. Karim joined the University of Texas at El Paso for his Master of Science degree in Mechanical Engineering. He has been appointed as a Graduate Research Assistant at the UTEP since August 2012. He has two journals and several conference paper publications during his master's degree.

Permanent address: Maddhasonadya, Banglabazar, Hatiya, Noakhali
Bangladesh

This thesis was typed by Hasanul Karim.